Supporting Information

A Tripodal Triazatruxene Derivative as a Face-On Oriented Hole-Collecting Monolayer for Efficient and Stable Inverted Perovskite Solar Cells

Minh Anh Truong,[*,1] Tsukasa Funasaki,[‡,1] Lucas Ueberricke,[‡,1] Wataru Nojo,[‡,1,2] Richard Murdey,[1] Takumi Yamada,[1] Shuaifeng Hu,[1] Aruto Akatsuka,[3] Naomu Sekiguchi,[4] Shota Hira,[1] Lingling Xie,[1] Tomoya Nakamura,[1] Nobutaka Shioya,[1] Daisuke Kan,[1] Yuta Tsuji,[5] Satoshi Iikubo,[4] Hiroyuki Yoshida,[3,6,7] Yuichi Shimakawa,[1] Takeshi Hasegawa,[1] Yoshihiko Kanemitsu,[1] Takanori Suzuki,[2] Atsushi Wakamiya[*,1]

[1]*Institute for Chemical Research, Kyoto University, Gokasho, Uji, Kyoto, 611-0011, Japan.*
[2]*Department of Chemistry, Faculty of Science, Hokkaido University, Sapporo, 060-0810, Japan.*
[3]*Graduate School of Science and Engineering, Chiba University, 1-33 Yayoi-cho, Inage-ku, Chiba, 263-8522, Japan.*
[4]*Department of Advanced Materials Science and Engineering, Faculty of Engineering Sciences, Kyushu University, Kasuga, Fukuoka, 816-8580, Japan.*
[5]*Department of Advanced Analytical Science for Materials and Devices, Faculty of Engineering Sciences, Kyushu University, Kasuga, Fukuoka, 816-8580, Japan.*
[6]*Graduate School of Engineering, Chiba University, 1-33 Yayoi-cho, Inage-ku, Chiba, 263-8522, Japan.*
[7]*Molecular Chirality Research Center, Chiba University, 1-33 Yayoi-cho, Inage-ku, Chiba, 263-8522, Japan.*

‡T.F. L.U., and W.N. contributed equally to this work.

*Corresponding authors:

truong.minhanh.2x@kyoto-u.ac.jp, wakamiya@scl.kyoto-u.ac.jp

Table of Contents

General

Materials

Unless otherwise stated, all materials were used as received without further purification. Oxindole (> 98.0%), phosphoryl chloride ($POCl_3$, > 98.0%), sodium hydride (60%, dispersion in paraffin liquid), 1,4-dibromobutane (> 98.0%), diethyl(3-bromopropyl)phosphonate (> 95.0%), triethylphosphite (> 97.0%), bromotrimethylsilane (> 95.0%), [2-(3,6-Dimethoxy-9*H*-carbazol-9-yl)ethyl]phosphonic acid (MeO-2PACz, > 98.0%), cesium iodide (CsI, > 99%), methylammonium bromide (MABr, > 98.0%, low water content), lead(II) iodide (PbI_2, 99.99%, trace metals basis), lead(II) bromide ($PbBr_2$, > 98.0%, for Perovskite precursor), formamidinium iodide (FAI, > 98.0%, low water content), and bathocuproine (BCP) were purchased from Tokyo Chemical Industry Co., Ltd. (TCI). Poly[bis(4-phenyl)(2,4,6-trimethylphenyl)amine] (PTAA) and ethane-1,2-diammonium iodide ($EDAI_2$) were purchased from Sigma-Aldrich Co., Ltd. (Sigma-Aldrich). Poly(3,4-ethylenedioxythiophene): poly(styrene sulfonate) (PEDOT:PSS) aqueous solution (Clevious PVP AI 4083) was purchased from Heraeus Co., Ltd. Fullerene C_{60} (sublimed, 99.99%) was purchased from ATR Company. Dimethylsulfoxide (DMSO, super dehydrated) was purchased from FUJIFILM Wako Pure Chemical Co., Ltd. Dimethylformamide (DMF), toluene and chlorobenzene were purchased from Kanto Chemical. Co., Inc. All of these solvents were degassed by argon (Ar) gas bubbling for 1 h and further dried over molecular sieves (3 Å) in an Ar-filled glove box (H_2O, O_2 < 0.1 ppm) before use.

Equipment and Characterization

All reactions were carried out under Ar atmosphere. Thin layer chromatography (TLC) was performed on plates coated with 0.25 mm thick silica gel 60F-254 (Merck). Column chromatography was performed by using PSQ 60B (Fuji Silysia). ^{1}H, ^{13}C, and ^{31}P NMR spectra were recorded on Bruker Avance-400 spectrometer (400 MHz for ^{1}H NMR, 101 MHz for ^{13}C NMR, and 162 MHz for ^{31}P NMR). The NMR chemical shifts are reported in ppm relative to the residual protons and carbons of $CDCl_3$ (δ = 7.26 ppm in ^{1}H NMR, δ = 77.16 ppm in ^{13}C NMR) and DMSO-d_6 (δ = 2.50 ppm in ^{1}H NMR, δ = 39.52 ppm in ^{13}C NMR). NMR spectra were processed using MestReNova version 14.0.0.

The contact angle measurements of the hole collecting layer covered ITO substrates were recorded in a range of 0–180° with high precision (± 0.1° accuracy) using a FAMAS interface measurement and analysis system (Kyowa Interface Science Co., Ltd.).

Photoelectron yield spectroscopy (PYS) measurements were carried out using a BUNKOUKEIKI BIP-KV201 under vacuum (~10^{-3} Pa). Film samples for PYS measurements were prepared by deposition of the hole collecting material solution on the surface of ITO substrates in an Ar-filled glove box and transferred to the chamber for PYS measurement without exposure to air.

Cyclic voltammetry (CV) was performed on an ALS/chi-620C electrochemical analyzer with the CV cell consisting of a glassy carbon working electrode, a Pt wire counter electrode, and an $Ag/AgNO_3$ reference electrode. The measurement was carried out under an argon atmosphere using DMF solutions of samples (1.0 mM) with 0.1 M tetrabutylammonium hexafluorophosphate ($^{n}Bu_4N^{+}PF_6^{-}$) as a supporting electrolyte. The redox potentials were calibrated with ferrocene as an internal standard.

Cyclic voltammetry (CV) of thin film was performed on an ALS/chi-620C electrochemical analyzer with the CV cell consisting of a bare or hole collecting monolayer adsorbed ITO working electrode, a Pt wire counter electrode, and an $Ag/AgNO_3$ reference electrode. The measurement was carried out under an argon atmosphere using *o*-DCB solution with 0.1 M tetrabutylammonium hexafluorophosphate ($^{n}Bu_4N^{+}PF_6^{-}$) as a supporting electrolyte. The redox potentials were calibrated with ferrocene as an internal standard. The area of working electrode dipped into electrolyte solution is 0.9 cm × 1.25 cm.

UV–vis absorption measurement was performed with a Shimadzu UV-3600 plus spectrometer (Shimadzu Co.,).

ATR measurements of powder samples were carried out with Thermo Fischer Scientific Magna 550 FT-IR spectrometer (Angle of incidence: 45°, un-polarization).

IRRAS measurements of thin films coated on Si/ITO substrates were carried out with Thermo Fischer Scientific Nicolet iS50 FT-IR spectrometer (Angle of incidence: 80°, p-polarization).

Scanning electron microscopy (SEM) was performed with a Hitachi S8010 ultra-high-resolution scanning electron microscope (Hitachi High-Tech Corporation).

Thin film X-ray diffraction (XRD) measurements were performed on a Rigaku RINT 2500 (Rigaku Co.) with Cu Kα radiation (λ= 1.5406 Å). All the samples were scanned with 2θ = 5°–50° with a 0.05° step and 0.2 s integration time. The power supply was operated at 300 mA and 40 kV.

Ultraviolet photoelectron spectroscopy (UPS) measurements were performed under ultrahigh vacuum (base pressure $<5 \times 10^{-8}$ Pa) using a homemade apparatus with an electron analyzer (PHOIBOS-100, SPECS) and helium discharge lamp. The He Iα resonance line (21.22 eV) was incident at 45° from the surface and detect the normal emission of photoelectrons to acquire the UPS spectra. The energies of the vacuum levels were deduced by using the secondary electron cutoff (SECO) of the UPS spectra at normal emission with a sample bias of −5 V. The metastable atom electron spectroscopy (MAES) spectra were recorded with the same apparatus. In the measurements, helium atoms were excited to the metastable states, 2^3S (19.82 eV), by a DC discharge. The metastable helium was incident to the sample at the normal angle, and emitted electron was detected at 60° from the normal. A sample bias of −1 V was applied during MAES spectra acquisition to increase spectral intensity. The position of the spectral feature was decided as the minimum of the second derivative of the spectrum. To assign the features that appeared in UPS/MAES spectra, we calculated the density of state (DOS). At first, we calculated the molecular orbital (MO) energies of a single molecule by B3LYP functional with the basis sets of 6-31G(d). The geometry was optimized before the MO energy calculation. Then the calculated energy levels were broadened by the Gaussian functions. The widths of the Gaussian functions were chosen to best simulate the experimental UPS/MAES spectra as described below. The DOS curve was obtained as the sum of these Gaussian curves. For the total DOS, all the molecular orbitals were used, and each MO level was broadened by the Gaussian function with the full-width at half maximum (FWHM) of 0.94 eV. For the partial DOS, the calculated MOs were categorized into σ, π, and anchor orbitals at first. Then each set of MOs was broadened by the Gaussian functions with an FWHM of 1.175 eV. By comparing the UPS spectrum and the calculated DOS, the calculated energy was scaled by multiplying a factor of 1.2 and aligned at the vacuum levels. This scaling factor was used for the analysis of MAES spectra.

For the time-resolved photoluminescene (TRPL) measurements, the samples were excited by a picosecond pulsed light with a wavelength of 688 nm (Advanced Laser Diode System). The excitation fluence was set at 100 nJ cm^{-2}. The PL signals were recorded using an avalanche photodiode (ID Quantique) and a time-correlated single photon

counting board (PicoQuant). The PL lifetimes were obtained by fitting the PL decay curve with a double exponential function and calculating the average lifetime. The PL spectra were recorded using a N_2 cooled charge-coupled-device array equipped with a monochromator (Princeton Instruments). The samples were kept in an Ar-filled metallic box for the whole process to avoid oxygen contamination and degradation.

Photocurrent–voltage (*J–V*) measurements for perovskite solar cells were measured in air with an OTENTO-SUNIII (BUNKOUKEIKI Co., Ltd.). The light intensity of the illumination source was adjusted by using standard silicon photodiodes (BS520). Each device was measured with a 20 mV voltage step and a 200 ms time step (i.e. scan rate of 0.1 V s^{-1}) using a Keithley 2400 source meter. The device active area was defined by an optimal mask (0.1 cm^2). Steady-state power output (SPO) measurements were performed by holding the device at the voltage of the maximum power point, as determined by the JV characteristic, and monitoring the current density over the course of 600 s.

External quantum efficiency (EQE) and internal quantum efficiency (IQE) spectra were measured with a Bunkoukeiki SMO-250III system equipped with a Bunkoukeiki SM-250 diffuse reflection unit (Bunkoukeiki Co., Ltd.). The incident light intensity was calibrated with a standard SiPD S1337-1010BQ silicon photodiode.

The cell for AIST certified measurement was encapsulated by a cover glass and sealed with AFTINNOVA-EF FD20 film (Ajinomoto Fine-Techno Co., Inc.) by heating at 70 °C for 5 min.

Impedance spectroscopy data was obtained in air with a 4192 LF impedance analyzer (Hewlett-Packard Company), at zero volts applied bias, 30 mV oscillator voltage, 20-200,000 Hz frequency scan, with the measurement devices under AM 1.5G simulated solar radiation with a 0.1 cm^{-2} shadow mask. The impedance data was fit by using the following model circuit:

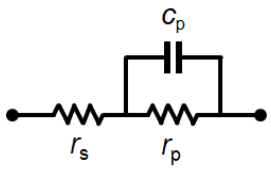

Geometry optimization was performed by using Gaussian 09 (revision C.01) program.[1]

Synthesis

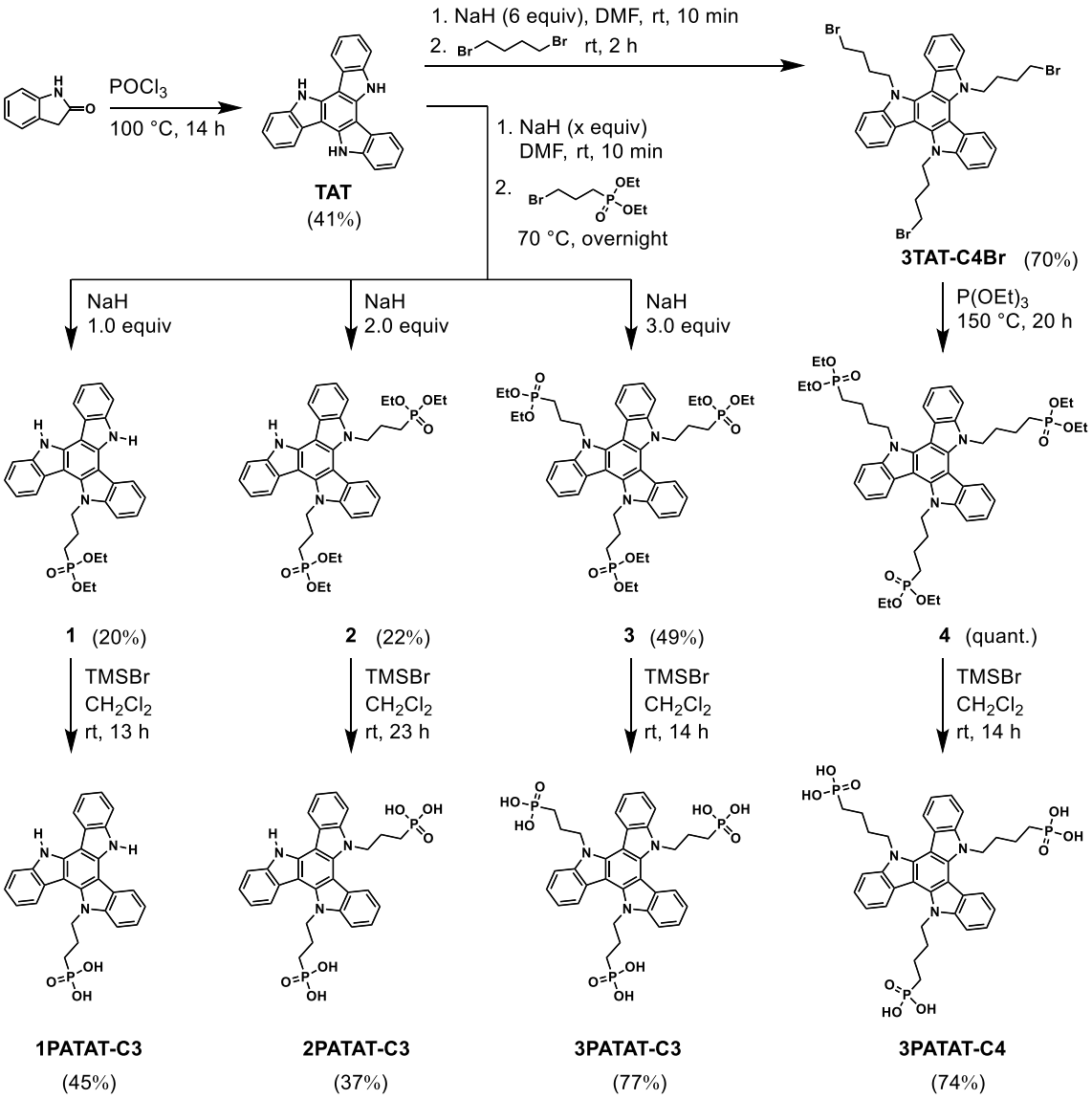

Scheme S1. Synthetic routes for triazatruxene-based hole collecting monolayer materials.

Synthesis of TAT:

TAT was synthesized according to previously reported synthetic method.[2]

Under Ar atmosphere, a solution of oxindole (10.7 g, 80.55 mmol) in $POCl_3$ (50 mL) was stirred and refluxed at 100 °C for 14 h. After cooling down to room temperature, the dark brown mixture was poured into ice water and neutralized carefully with NaOH. After neutralization, the brown precipitate was filtered to give the crude product. The crude product was purified by silica gel column chromatography with dichloromethane as eluent. After evaporation of eluate under reduced pressure and recrystallization from

acetone, **TAT** was obtained as a pale yellow solid (5.8 g, 11.11 mmol, 41% yield). ^{1}H NMR (400 MHz, DMSO-d_6): δ 11.86 (s, 3H), 8.68–8.66 (d, J = 7.6 Hz, 3H), 7.73–7.71 (d, J = 8.0 Hz, 3H), 7.40–7.31 (m, 6H).

Notes:

- $POCl_3$ is a corrosive reagent. It reacts violently with water, releasing phosphoric acid and fumes of hydrogen chloride.
- Attempts to synthesize the molecule with a two-carbon spacer from **TAT** were unsuccessful due to competing elimination reaction.

Synthesis of 3TAT-C4Br:

To a solution of **TAT** (345 mg, 1.00 mmol) in anhydrous DMF (10 mL), NaH (144 mg, 6.00 mmol) was added at room temperature and stirred for 10 min. Then, 1,4-dibromobutane (1.8 mL, 15.00 mmol) was added via syringe and the mixture was stirred for 2 h. The reaction mixture was poured into water, washed with brine and extracted with dichloromethane. The organic phase was dried over Na_2SO_4, filtered, and concentrated under reduced pressure to give the crude product. The obtained crude product was purified by silica gel column chromatography (hexane: dichloromethane = 2:1 to 1:1, R_f = 0.25 to 0.59) to give 526 mg of **3TAT-C4Br** (0.70 mmol, 70% yield) as a brown solid. m.p. 95 °C; ^{1}H NMR (400 MHz, $CDCl_3$): δ 8.24–8.22 (d, J = 8.0 Hz, 3H), 7.65–7.63 (d, J = 8.0 Hz, 3H), 7.50–7.46 (t, J = 7.2 Hz, 3H), 7.40–7.36 (t, J = 8.0 Hz, 3H), 4.96–4.92 (t, J = 7.6 Hz, 6H), 3.25–3.22 (t, J = 6.8 Hz, 6H), 2.13–2.06 (m, 6H), 1.71–1.64 (m, 6H). ^{13}C NMR (101 MHz, $CDCl_3$): δ 141.0, 138.8, 123.5, 123.2, 121.6, 120.2, 110.8, 103.5, 46.1, 33.1, 29.8, 28.3. HRMS (APCI) (m/z): $[M+H]^+$ calcd. for $C_{36}H_{37}Br_3N_3$, 750.0512; found, 750.0529.

Synthesis of 1:

To a solution of **TAT** (345 mg, 1.00 mmol) in anhydrous DMF (10 mL), NaH (24 mg, 1.00 mmol) was added at room temperature and stirred for 15 min. Then, diethyl(3-bromopropyl)phosphonate (0.21 mL, 1.10 mmol) was added via syringe and the mixture was stirred at 70 °C overnight. After cooling down to room temperature, the reaction mixture was poured into water, washed with brine and extracted with dichloromethane. The organic phase was dried over $MgSO_4$, filtered, and concentrated under reduced pressure to give the crude product. The obtained crude product was purified by silica gel column chromatography (hexane: dichloromethane = 2:1, R_f = 0.08 then diethyl ether, R_f = 0.76) to give 105 mg of **1** (0.20 mmol, 20% yield) as brown oil. ^{1}H NMR (400 MHz, DMSO-d_6): δ 11.93 (s, 1H), 11.82 (s, 1H), 8.73–8.70 (t, J = 6.4 Hz, 2H), 8.32–8.30 (d, J

= 8.0 Hz, 1H), 7.88–7.86 (d, *J* = 8.0 Hz, 1H), 7.81–7.79 (d, *J* = 8.0 Hz, 1H), 7.76–7.74 (d, *J* = 7.6 Hz, 1H), 7.48–7.30 (m, 6H), 5.15–5.12 (t, *J* = 7.2 Hz, 2H), 3.88–3.80 (m, 4H), 2.15 (br, 2H), 1.85–1.77 (m, 2H), 1.07–1.03 (t, *J* = 6.8 Hz, 6H). ^{13}C NMR (101 MHz, DMSO-d_6): δ 139.1, 139.0, 138.9, 135.7, 135.0, 133.7, 122.8, 122.7, 122.5, 122.3, 121.9, 121.3, 121.1, 119.9, 119.8, 119.7, 119.6, 119.3, 111.5, 111.2, 109.6, 101.5, 100.9, 100.5, 61.0, 60.9, 45.6, 45.4, 23.8, 23.8, 22.3, 20.9, 16.1, 16.1. ^{31}P NMR (162 MHz, DMSO-d_6): δ 31.38. HRMS (APCI) (*m*/*z*): $[M+H]^+$ calcd. for $C_{31}H_{31}N_3O_3P$, 524.2098; found, 524.2098.

Synthesis of 2:

To a solution of **TAT** (345 mg, 1.00 mmol) in anhydrous DMF (10 mL), NaH (48 mg, 2.00 mmol) was added at room temperature and stirred for 10 min. Then, diethyl(3-bromopropyl)phosphonate (0.42 mL, 2.20 mmol) was added via syringe and the mixture was stirred at 70 °C overnight. After cooling down to room temperature, the reaction mixture was poured into water, washed with brine and extracted with dichloromethane. The organic phase was dried over $MgSO_4$, filtered, and concentrated under reduced pressure to give the crude product. The obtained crude product was purified by silica gel column chromatography (ethyl acetate: methanol = 1:0 to 20:1, and 10:1, R_f = 0.21) to give 157 mg of **2** (0.22 mmol, 22% yield) as a brown oil. ^{1}H NMR (400 MHz, DMSO-d_6): δ 11.88 (s, 1H), 8.77–8.75 (d, *J* = 8.0 Hz, 1H), 8.35–8.33 (d, *J* = 8.0 Hz, 1H), 8.30–8.28 (d, *J* = 8.4 Hz, 1H), 7.92–7.82 (m, 3H), 7.51–7.31 (m, 6H), 5.16–5.13 (t, *J* = 7.6 Hz, 2H), 5.10–5.06 (t, *J* = 7.2 Hz, 2H), 4.06–4.00 (m, 3H), 3.86–3.75 (m, 7H), 2.08 (m, 4H), 1.81–1.63 (m, 4H), 1.19–1.16 (t, *J* = 6.8 Hz, 4H), 1.07–1.00 (m, 11H). ^{13}C NMR (101 MHz, DMSO-d_6): δ 140.1, 139.6, 139.5, 137.4, 135.8, 135.0, 123.2, 122.9, 122.8, 122.5, 121.8, 121.4, 121.1, 120.1, 120.0, 119.9, 119.8, 111.7, 110.3, 102.2, 101.9, 100.9, 79.2, 60.9, 60.8 (two peaks), 54.9, 46.2, 46.0, 45.7, 45.5, 23.2, 23.2, 23.1, 22.2, 20.8, 16.1, 16.0 (two peaks), 15.9. ^{31}P NMR (162 MHz, DMSO-d_6): δ 30.84, 30.79. HRMS (ESI) (*m*/*z*): $[M+H]^+$ calcd. for $C_{38}H_{46}N_3O_6P_2$, 702.2856; found, 702.2825.

Synthesis of 3:

To a solution of **TAT** (1.73 g, 5.00 mmol) in anhydrous DMF (50 mL), NaH (360 mg, 15.00 mmol) was added at room temperature and stirred for 10 min. Then, diethyl(3-bromopropyl)phosphonate (2.9 mL, 15.00 mmol) was added via syringe and the mixture was stirred at 70 °C overnight. After cooling down to room temperature, the reaction mixture was poured into water, washed with brine and extracted with dichloromethane. The organic phase was dried over $MgSO_4$, filtered, and concentrated under reduced

pressure to give the crude product. The obtained crude product was purified by silica gel column chromatography (ethyl acetate: methanol = 1:0 to 4:1, and 1:1, R_f = 0.14) to give 2.17 g of **3** (2.46 mmol, 49% yield) as a brown oil. ^{1}H NMR (400 MHz, DMSO-d_6): δ 8.29–8.27 (d, J = 8.4 Hz, 3H), 7.91–7.89 (d, J = 8.0 Hz, 3H), 7.51–7.48 (t, J = 7.2 Hz, 3H), 7.41–7.37 (t, J = 7.2 Hz, 3H), 5.08–5.04 (t, J = 7.2 Hz, 6H), 3.80–3.73 (m, 12H), 1.93 (br, 6H), 1.62–1.54 (m, 6H), 1.03–1.01 (t, J = 7.2 Hz, 12H). ^{13}C NMR (101 MHz, DMSO-d_6): δ 140.5, 137.6, 123.2, 122.3, 121.4, 120.4, 111.1, 102.8, 60.9, 60.8, 54.9, 46.3, 46.1, 22.5, 22.4, 22.1, 20.7, 16.0, 15.9. ^{31}P NMR (162 MHz, DMSO-d_6): δ 30.61. HRMS (APCI) (m/z): $[M+H]^+$ calcd. for $C_{45}H_{61}N_3O_9P_3$, 880.3615; found, 880.3585.

Synthesis of 4:

3TAT-C4Br (400 mg, 0.53 mmol) was dissolved in triethylphosphite (2 mL) and the reaction mixture was stirred at 150 °C for 20 h. After cooling down to room temperature, the solvent was removed under reduced pressure to give the crude product. The obtained crude product was purified by silica gel column chromatography (chloroform: methanol = 200:1 to 100:1, R_f = 0.1) to give 597 mg of **4** (0.65 mmol, quantitative yield) as a pale yellow oil. ^{1}H NMR (400 MHz, $CDCl_3$): δ 8.24–8.22 (d, J = 8.0 Hz, 3H), 7.63–7.61 (d, J = 8.0 Hz, 3H), 7.47–7.43 (t, J = 7.2 Hz, 3H), 7.37–7.33 (t, J = 7.6 Hz, 3H), 4.96–4.92 (t, J = 7.6 Hz, 6H), 3.98–3.90 (m, 12H), 2.05–1.98 (m, 6H), 1.67–1.48 (m, 12H), 1.20–1.17 (t, J = 7.2 Hz, 18H). ^{13}C NMR (101 MHz, $CDCl_3$): δ 141.1, 138.9, 123.6, 123.2, 121.5, 120.2, 110.8, 103.5, 61.6, 61.5, 46.2, 30.6, 30.4, 26.1, 24.7, 20.0, 19.9, 16.5, 16.4. ^{31}P NMR (162 MHz, DMSO-d_6): δ 32.14. HRMS (APCI) (m/z): $[M+H]^+$ calcd. for $C_{48}H_{66}N_3O_9P_3$, 921.4012; found, 921.4019.

Synthesis of 1PATAT-C3:

Compound **1** (24 mg, 0.05 mmol) was dissolved in dry dichloromethane (2 mL). Then, bromotrimethylsilane (57 μL, 0.44 mmol) was added dropwise. The reaction mixture was stirred at room temperature for 13 h. After the solvent was removed under reduced pressure, the solid residue was dissolved in methanol (0.5 mL) and stirred for 10 min. Then, dichloromethane (5 mL) was added and the resulting solution was stirred at 0 °C for further 1 h. The precipitate was filtered off and washed with cold dichloromethane to give 10 mg of **1PATAT-C3** (0.02 mmol, 45% yield) as a greenish powder. m.p. > 400 °C; ^{1}H NMR (400 MHz, DMSO-d_6): δ 11.92 (s, 1H), 11.81 (s, 1H), 8.73–8.69 (t, J = 8.8 Hz, 2H), 8.31–8.29 (d, J = 8.0 Hz, 1H), 7.82–7.73 (m, 3H), 7.42–7.28 (m, 6H), 5.06 (br, 2H), 2.22 (m, 3H), 1.60–1.52 (m, 3H). ^{13}C NMR (101 MHz, DMSO-d_6): δ 139.1, 139.0, 138.9, 135.8, 135.0, 133.8, 122.8, 122.7, 122.5, 122.2, 122.0, 119.9, 119.7, 119.6, 119.5, 119.2,

111.5, 111.1, 109.7, 101.4, 100.8, 100.5, 45.9, 45.7, 25.6, 24.9, 24.2. ^{31}P NMR (162 MHz, $CDCl_3$): δ 26.23. HRMS (ESI) (*m*/*z*): $[M–H]^-$ calcd. for $C_{27}H_{21}N_3O_3P$, 466.1326; found, 466.1324.

Synthesis of 2PATAT-C3:

Compound **2** (47 mg, 0.07 mmol) was dissolved in dry dichloromethane (3 mL). Then, bromotrimethylsilane (92 μL, 0.70 mmol) was added dropwise. The reaction mixture was stirred at room temperature for 23 h. After the solvent was removed under reduced pressure, the solid residue was dissolved in methanol (0.5 mL) and stirred for 10 min. Then, dichloromethane (5 mL) was added and the resulting solution was stirred at 0 °C for several hours. The precipitate was filtered off and washed with cold dichloromethane to give 15 mg of **2PATAT-C3** (0.03 mmol, 37% yield) as a blueish powder. m.p. > 400 °C; ^{1}H NMR (400 MHz, DMSO-d_6): δ 11.88 (s, 1H), 8.75–8.73 (d, *J* = 7.6 Hz, 1H), 8.29–8.27 (d, *J* = 7.6 Hz, 2H), 7.84–7.80 (br, 3H), 7.45–7.30 (br, 6H), 5.15–5.01 (br, 5H), 1.94–1.83 (br, 4H), 0.86 (br, 4H). ^{13}C NMR (101 MHz, DMSO-d_6): δ 140.3, 139.8, 139.7, 137.8, 136.1, 135.2, 123.4, 123.1, 123.0, 122.6, 122.0, 121.6, 121.3, 120.3, 120.1, 119.9, 111.9, 110.7, 110.5, 102.3, 102.1, 101.1, 46.7, 46.5, 46.3, 46.1, 25.5, 24.3, 24.1. ^{31}P NMR (162 MHz, DMSO-d_6): δ 25.95, 25.87. HRMS (ESI) (*m*/*z*): $[M–H]^-$ calcd. for $C_{30}H_{28}N_3O_6P_2$, 588.1453; found, 588.1459.

Synthesis of 3PATAT-C3:

Compound **3** (200 mg, 0.23 mmol) was dissolved in dry dichloromethane (6 mL). Then, bromotrimethylsilane (0.30 mL, 2.31 mmol) was added dropwise. The reaction mixture was stirred at room temperature for 14 h. After the solvent was removed under reduced pressure, the solid residue was reprecipitated by using a mixture of dichloromethane and methanol (5:1, v:v). The precipitate was filtered off and washed with dichloromethane to give 125 mg of **3PATAT-C3** (0.18 mmol, 77% yield) as a blueish powder. m.p. > 400 °C; ^{1}H NMR (400 MHz, DMSO-d_6): δ 8.30–8.28 (d, *J* = 8.0 Hz, 3H), 7.91–7.89 (d, *J* = 8.0 Hz, 3H), 7.51–7.47 (t, *J* = 7.2 Hz, 3H), 7.41–7.37 (t, *J* = 7.6 Hz, 3H), 5.08–5.05 (t, *J* = 6.8 Hz, 6H), 1.95–1.85 (m, 6H), 1.13–1.04 (m, 6H). ^{13}C NMR (101 MHz, DMSO-d_6): δ 141.0, 137.8, 123.2, 122.5, 121.5, 120.4, 111.4, 103.2, 46.8, 46.6, 25.2, 23.8, 23.0, 22.9. ^{31}P NMR (162 MHz, DMSO-d_6): δ 24.75. HRMS (MALDI) (*m*/*z*): $[M]^+$ calcd. for $C_{33}H_{36}N_3O_9P_3$, 711.1664; found, 711.1653.

Synthesis of 3PATAT-C4:

Compound **4** (500 mg, 0.54 mmol) was dissolved in dry dichloromethane (15 mL). Then, bromotrimethylsilane (0.70 mL, 5.45 mmol) was added dropwise. The reaction mixture was stirred at room temperature for 14 h. After the solvent was removed under reduced pressure, the solid residue was reprecipitated by using a mixture of dichloromethane and methanol (20:1, v:v). The precipitate was filtered off and washed with dichloromethane to give 302 mg of **3PATAT-C4** (0.40 mmol, 74% yield) as a greenish powder. m.p. > 400 °C; ^{1}H NMR (400 MHz, DMSO-d_6): δ 8.28–8.26 (d, J = 8.4 Hz, 3H), 7.87–7.84 (d, J = 8.0 Hz, 3H), 7.48–7.44 (t, J = 7.2 Hz, 3H), 7.37–7.34 (t, J = 7.6 Hz, 3H), 4.99–4.96 (t, J = 6.8 Hz, 6H), 1.92–1.88 (m, 6H), 1.43–1.29 (m, 12H). ^{13}C NMR (101 MHz, DMSO-d_6): δ 140.6, 138.5, 123.0, 122.5, 121.3, 120.0, 111.3, 102.6, 46.0, 30.2, 30.0, 27.7, 26.3, 19.9. ^{31}P NMR (162 MHz, $CDCl_3$): δ 27.56. HRMS (ESI) (*m*/*z*): $[M–H]^-$ calcd. for $C_{36}H_{41}N_3O_9P_3$, 752.2056; found, 752.2061.

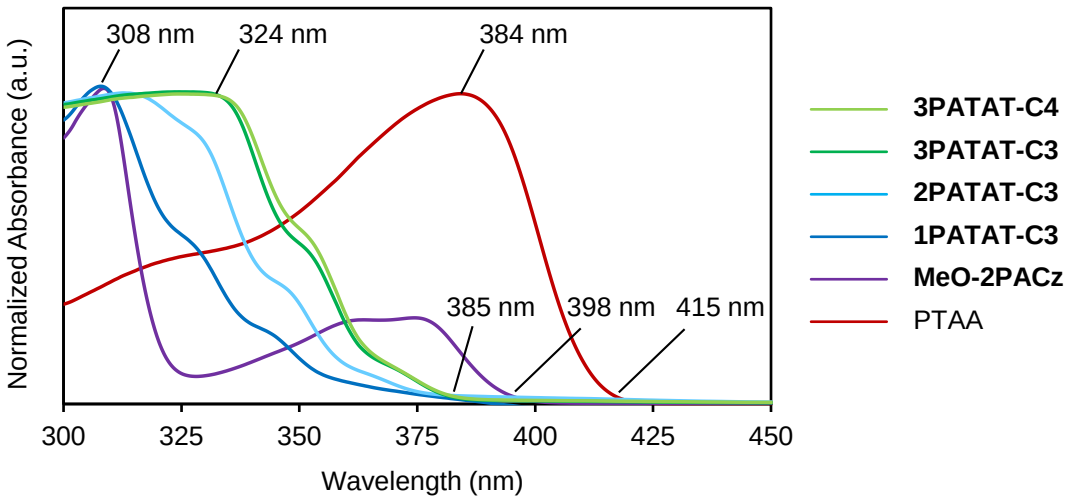

Figure S1. UV–Vis absorption spectra of the **PATAT** series and **MeO-2PACz** in DMF solution (10^{-4} M), and PTAA in THF solution (10^{-3} mg mL^{-1}).

(a) bare ITO

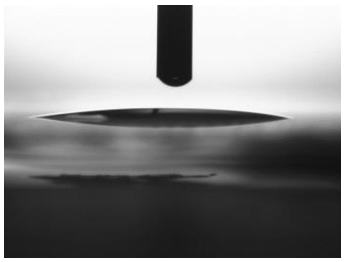

Contact angle: 8˚

(b) ITO/PEDOT:PSS

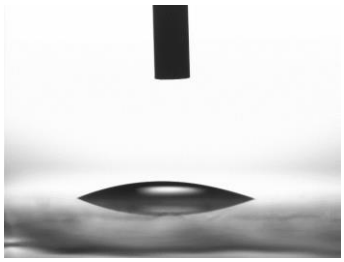

Contact angle: 18˚

(c) ITO/PTAA

Contact angle: 89˚

(d) ITO/**MeO-2PACz**

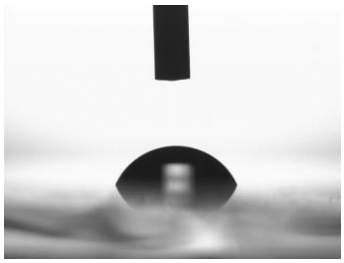

Contact angle: 64˚

(e) ITO/**1PATAT-C3**

Contact angle: 74˚

(f) ITO/**2PATAT-C3**

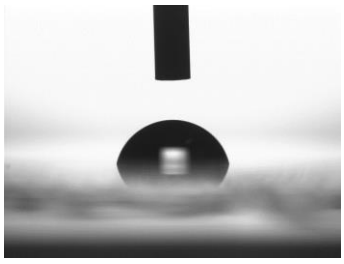

Contact Angle: 74˚

(g) ITO/**3PATAT-C3**

Contact angle: 75˚

(h) ITO/**3PATAT-C4**

Contact angle: 76˚

Figure S2. Contact angles of the water droplets on (a) bare ITO and (b–h) ITO/HCMs.

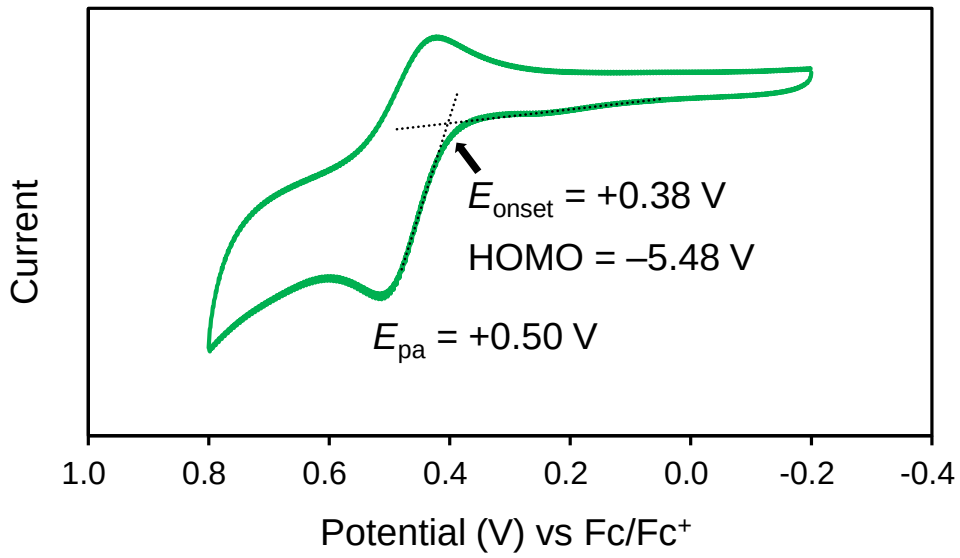

Figure S3. Cyclic voltammogram of **3PATAT-C3** dissolved in DMF solution at a scan rate of 100 mV s^{-1}.

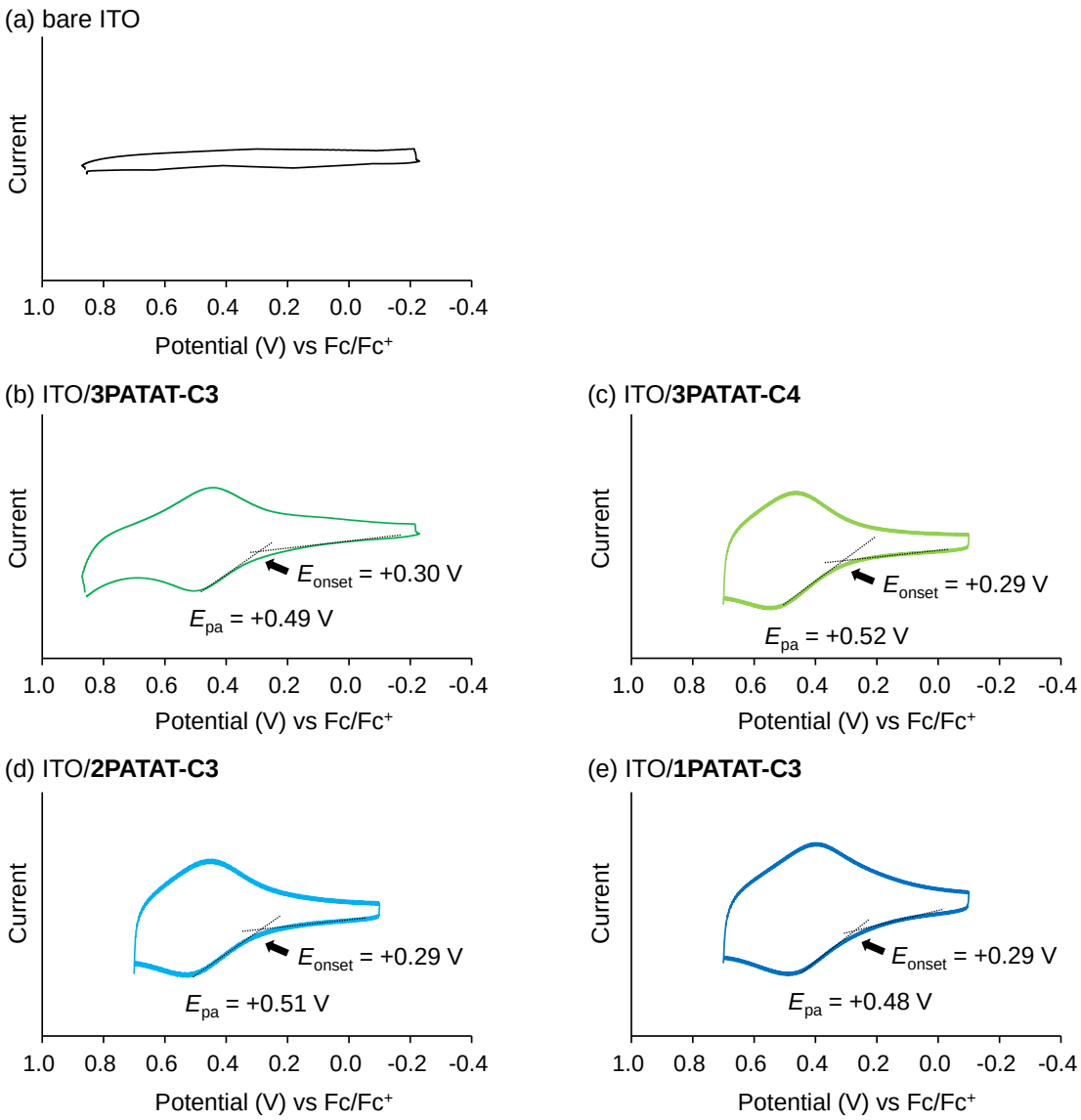

Figure S4. Cyclic voltammograms of the **PATAT** derivatives adsorbed on ITO substrates measured in *o*-DCB solution at a scan rate of 100 mV s^{-1}.

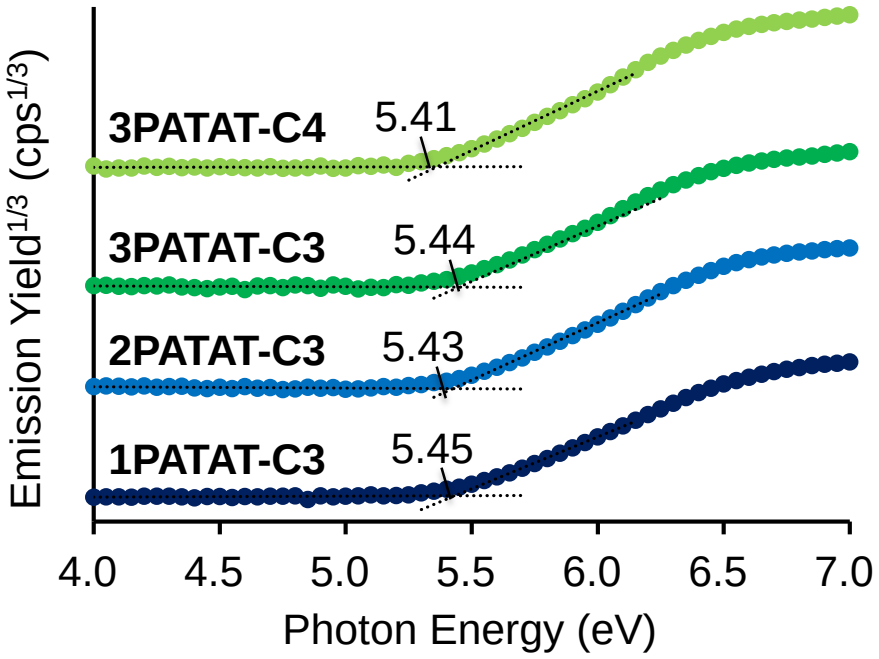

Figure S5. Photoelectron yield spectroscopy (PYS) results of the **PATAT** derivatives adsorbed ITO substrates.

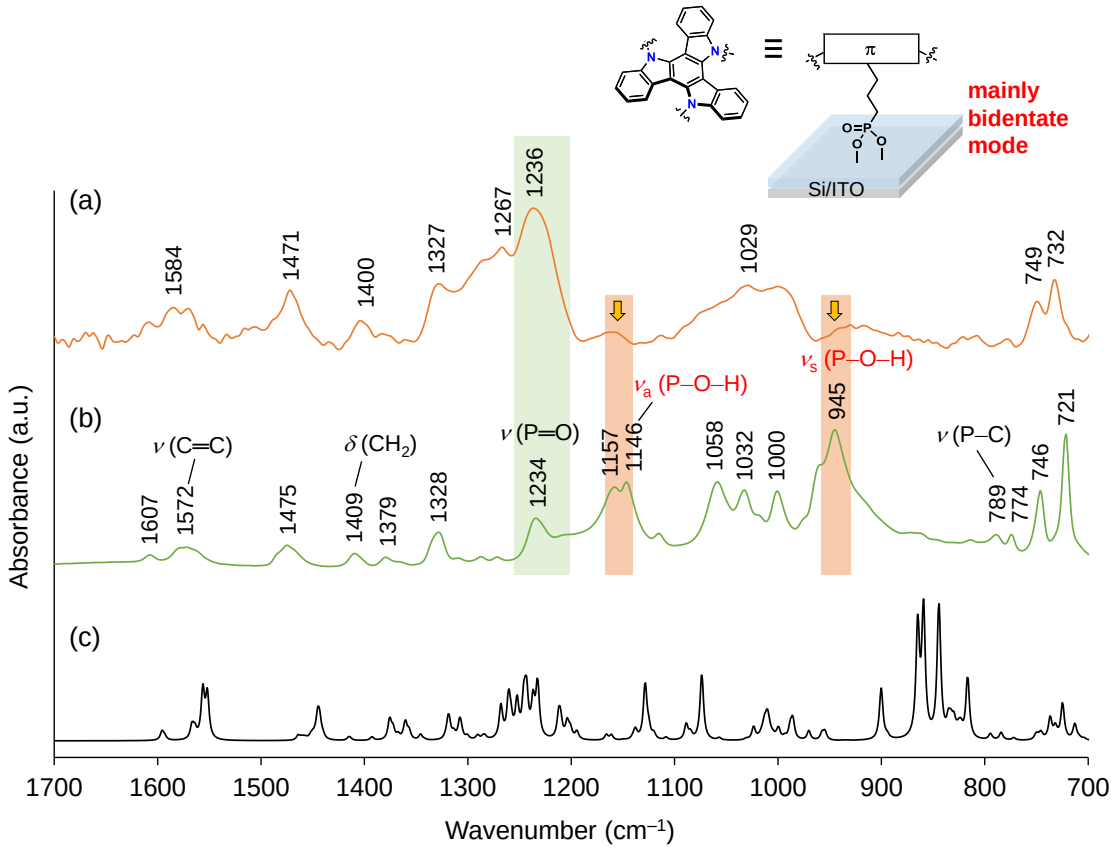

Figure S6. (a) IRRAS spectrum of **3PATAT-C3**-coated on Si/ITO substrate, (b) ATR spectrum of **3PATAT-C3** powder, and (c) calculated spectra of **3PATAT-C3** at B3LYP/6-31G(d,p) level of theory (scaling factor = 0.9613).

(a) AFM of commercial ITO Substrate

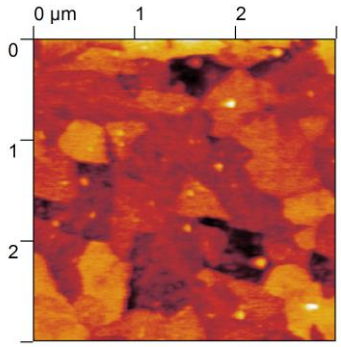

Roughness: 3.5 nm

(b) AFM of epitaxial ITO (111) Film

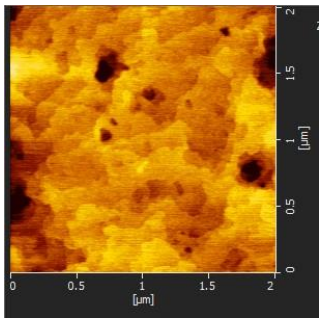

Roughness: 0.3 nm

(c) STM of **3PATAT-C3** adsorb on epitaxial ITO

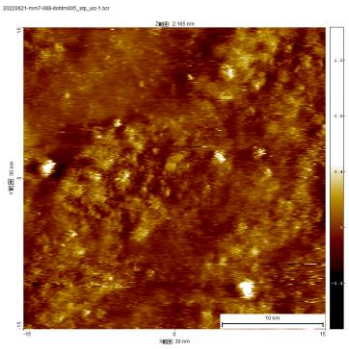

Figure S7. AFM of (a) commercial ITO substrate and (b) epitaxial ITO (111) thin film. Epitaxial ITO (111) film was prepared on Yttrium Stabilized Zirconia (YSZ) (100) substrate using pulsed laser deposition (PLD) method followed by ex-situ annealing at 1250 °C for 5 min under Ar atmosphere. (c) STM measurement of ITO/**3PATAT-C3**.

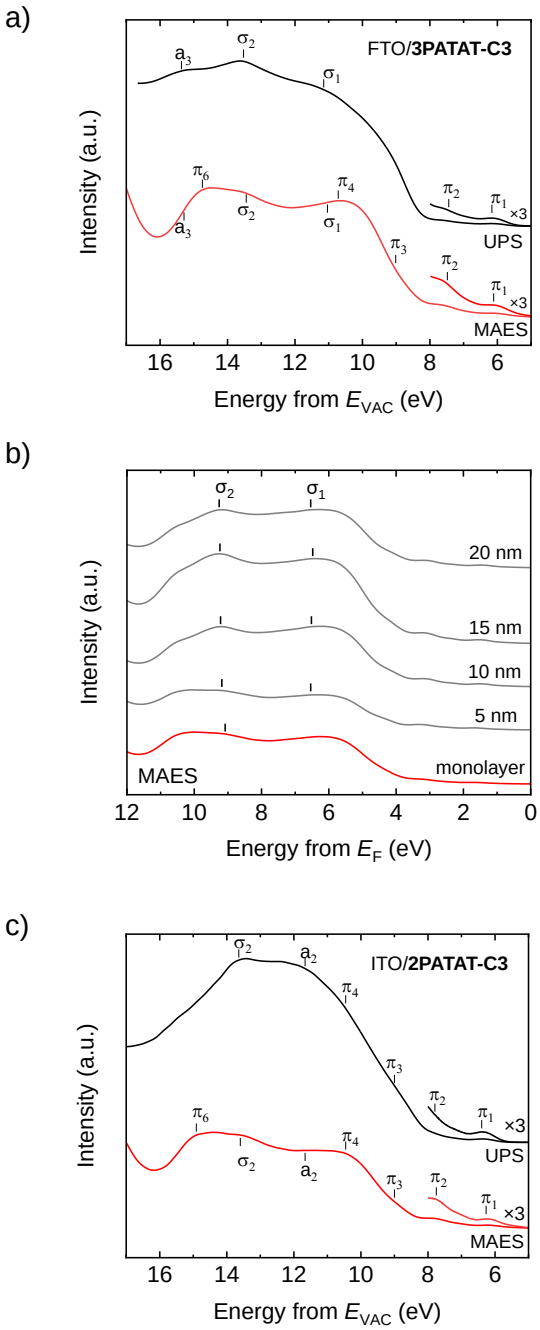

Figure S8. (a) UPS and MAES spectra of FTO/**3PATAT-C3**. (b) MAES spectra of ITO/**3PATAT-C3** with different thickness of **3PATAT-C3**. Multilayer **3PATAT-C3** films were fabricated by spin coated **3PATAT-C3** (0.02 M) in DMF solution onto ITO substrates with different spinning speed. (c) UPS and MAES spectra of ITO/**2PATAT-C3**.

Theoretical Calculations

The first-principles calculations based on the density functional theory (DFT) were performed with the Vienna Ab initio Simulation Package (VASP) [3,4] using the projector-augmented[5,6] wave method. The Perdew-Burke-Ernzerhof (PBE) exchange–correlation functional was used within the generalized gradient approximation.[7] To model the (111) In_2O_3 surface, we used slabs with three O-In-O layers of the material with an ~10 Å vacuum layer, which correspond to large supercells with stoichiometry $In_{32}O_{48}$. To describe **3PATAT-C3** chemisorption configurations, we considered three cases with single, double, or triple covalent anchoring to the surface and with the acidic hydrogen atoms attached to nearby O sites as individual species. A cutoff energy of 500 eV was selected, and k-points were set at 2 × 2 × 2. Structural optimization was achieved based on the electronic structure calculations using the Gaussian smearing method; the sigma value was set at 0.05 eV, and the structural optimization convergence threshold was set at 0.05 eV $Å^{-1}$.

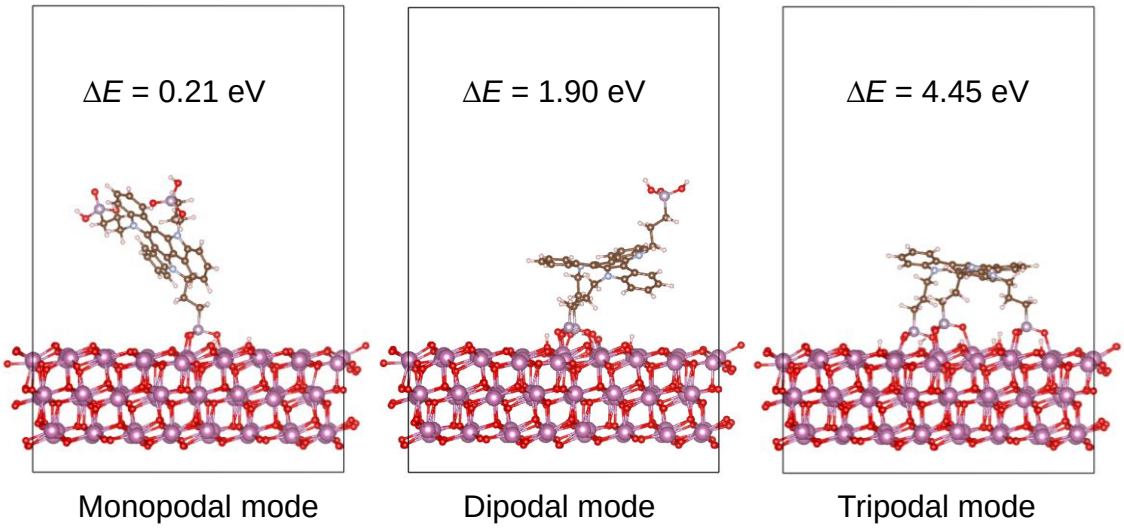

Figure S9. Optimized configurations of **3PATAT-C3** after adsorbed on ITO surface models in monopodal, dipodal, and tripodal mode. The energy difference (ΔE) between before and after adsorption was also given.

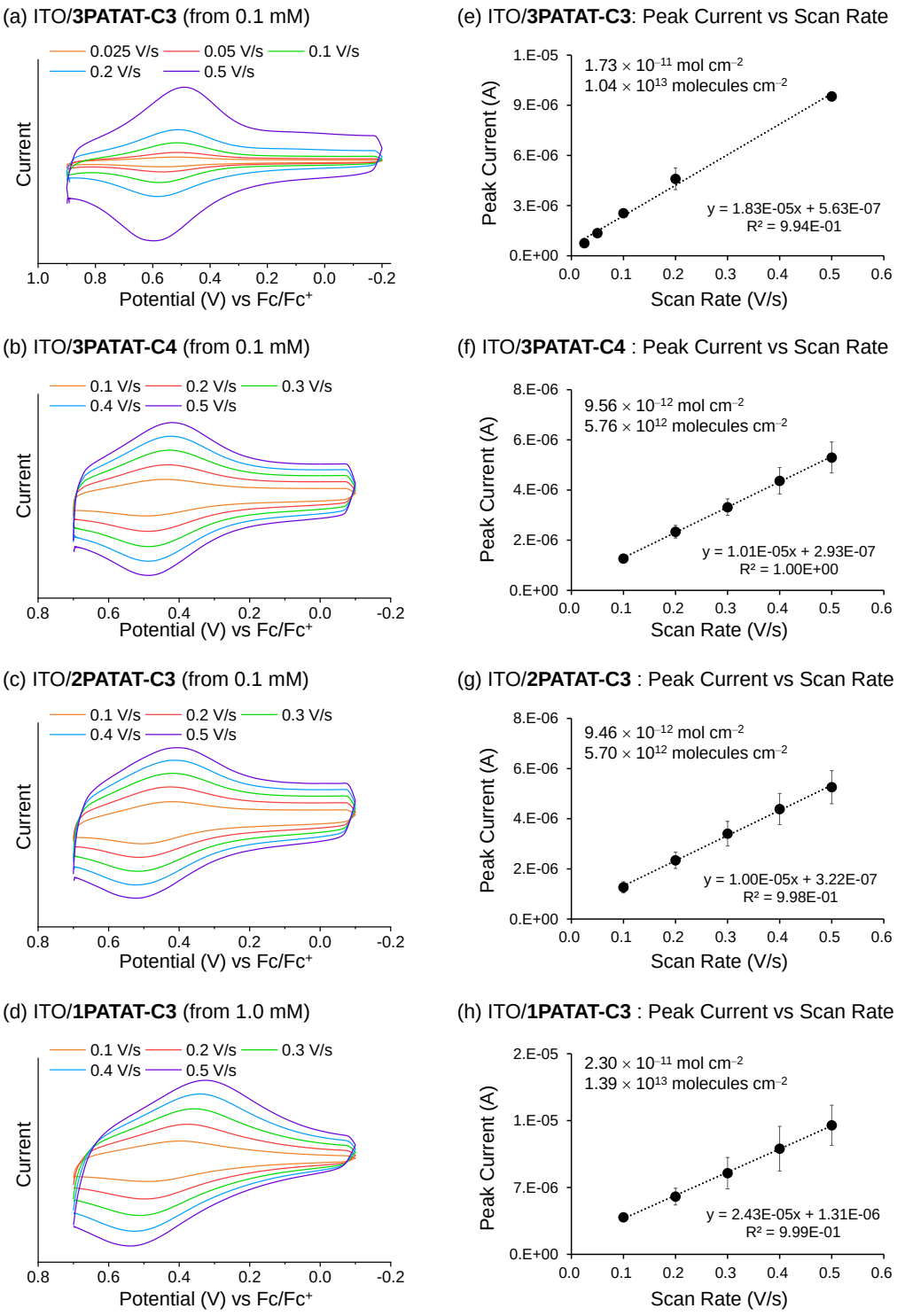

Figure S10. Cyclic voltammograms of the **PATAT** derivatives adsorbed on ITO substrates measured in *o*-DCB solution under different scan rate (a–d) and their corresponding peak current vs scan rate chart (e–h).

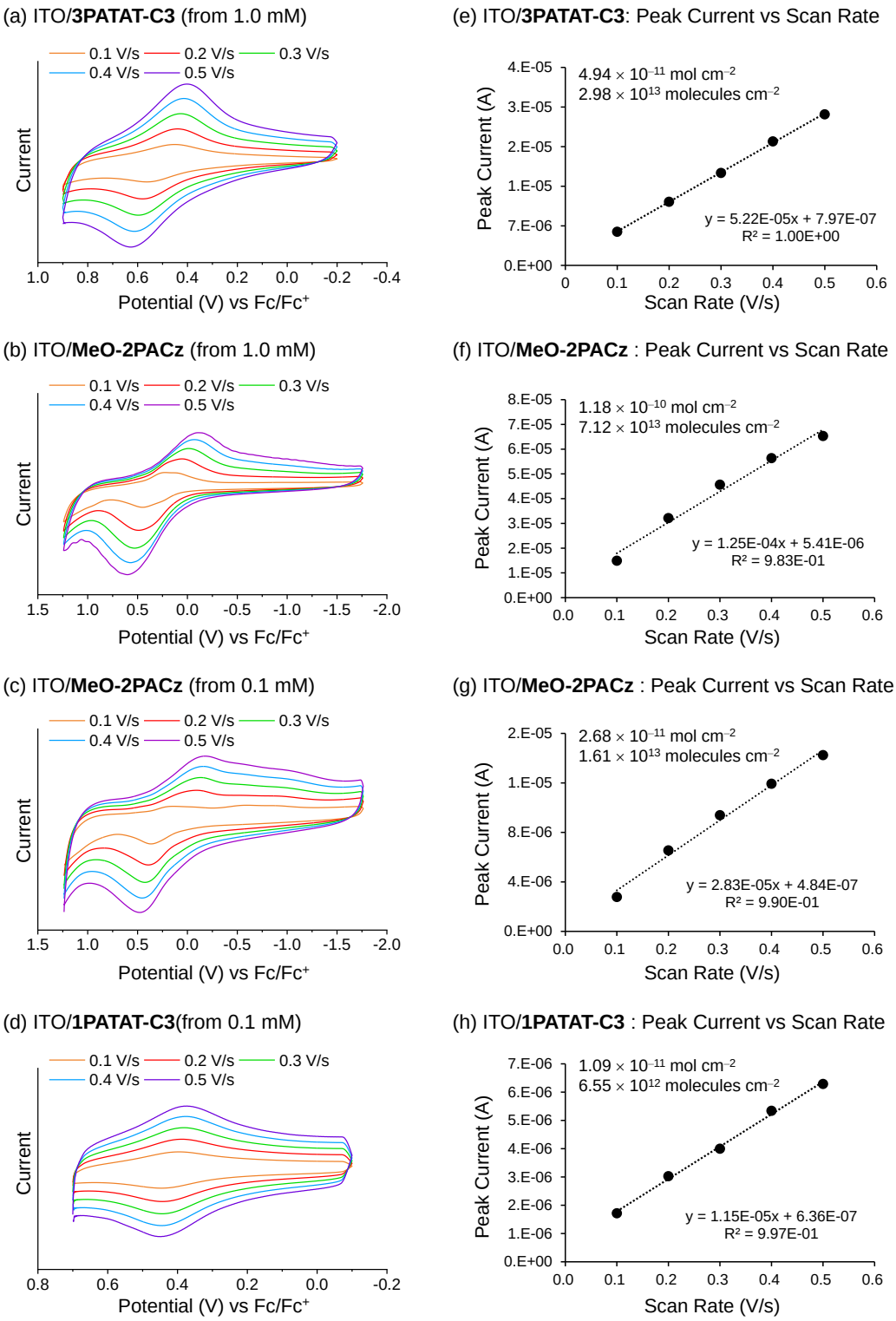

Figure S11. Cyclic voltammograms of **3PATAT-C3** (1.0 mM), **MeO-2PACz** (1.0 mM, 0.1 mM), and **1PATAT-C3** (0.1 mM) adsorbed on ITO substrates measured in *o*-DCB solution under different scan rate (a–d) and their corresponding peak current vs scan rate chart (e–h).

Notes:

The surface density of **1PATAT-C3**, **3PATAT-C3**, and **MeO-2PACz** on ITO substrates fabricated from 0.1 mM DMF solutions were determined to be 6.6×10^{12}, 1.0×10^{13}, and 1.6×10^{13} molecules cm^{-2}, respectively.

When 1.0 mM DMF solutions were used, the surface density of **1PATAT-C3**, **3PATAT-C3**, and **MeO-2PACz** increased to 1.4×10^{13}, 2.9×10^{13}, and 7.1×10^{13} molecules cm^{-2}, respectively

The surface density of tripodal **3PATAT-C3** molecule is higher than the monopodal **1PATAT-C3**. Although the number of adsorbed molecules for monopodal **MeO-2PACz** was higher than **3PATAT-C3**, using the molecular footprint of **3PATAT-C3** and **MeO-2PACz** (estimated as 132.1 and 51.6 $Å^2$, respectively, from the shadow projection of the DFT optimized structures as shown in **Figure S12**), the effective coverage of "face-on" oriented **3PATAT-C3** was calculated to be 1.1–1.6 times more than "edge-on" oriented **MeO-2PACz**.

As shown in concentration optimization for perovskite solar cells part (**Figure S26**), compared to PSCs using **3PATAT-C3** fabricated from 1.0 mM in DMF solution, devices fabricated from 0.1 mM **3PATAT-C3** show better performance with higher V_{OC}, higher J_{SC} and FF, and better reproducibility. Together with data obtained from MAES measurement, we think that 0.1 mM of **3PATAT-C3** in DMF solution is enough to fabricate a monolayer, while films fabricated from 1.0 mM solution may contain physically adsorbed parts.

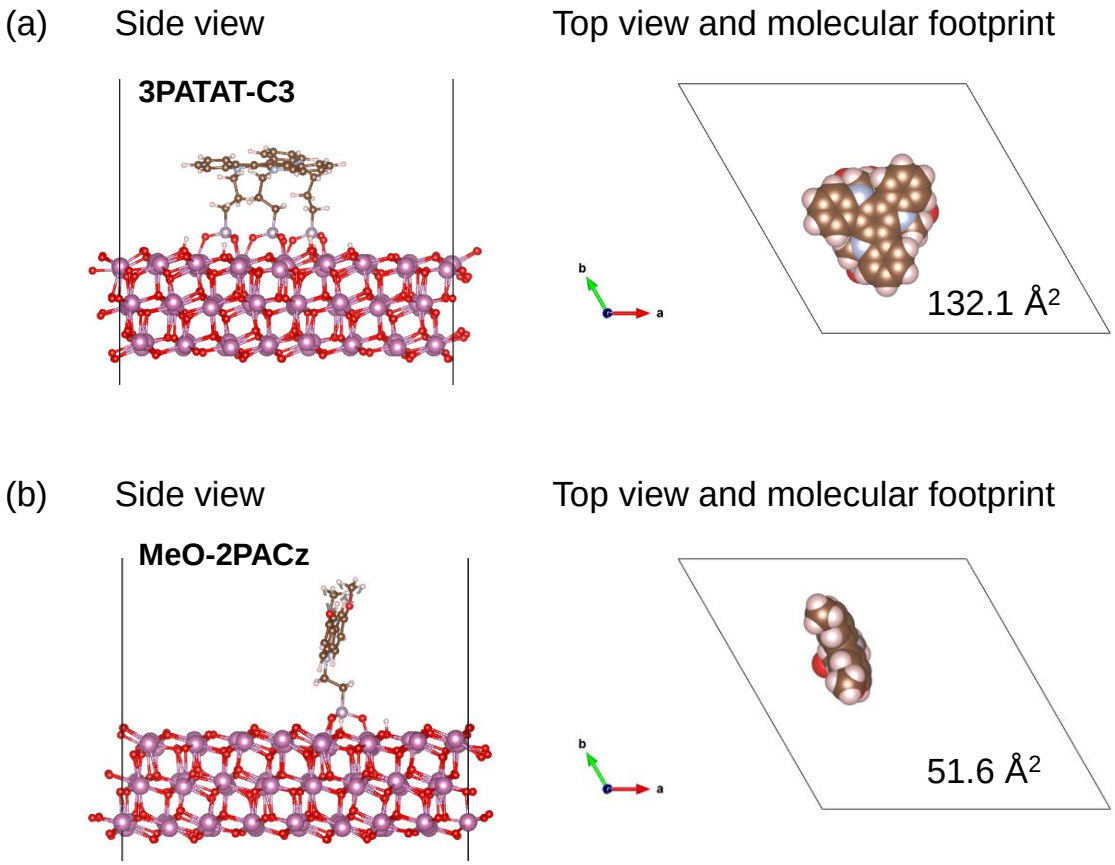

Figure S12. Adsorption model of (a) **3PATAT-C3** and (b) **MeO-2PACz** on the ITO (111) surfaces and their corresponding molecular footprints.

Device Fabrication.

Preparation of Transparent Conductive Oxide (TCO) Substrates

Glass/ITO substrates (10 Ω sq^{-1}) or glass/FTO substrates (10 Ω sq^{-1}, AGC Inc.) were etched with zinc powder and HCl (6 M in de-ionized water), and consecutively cleaned with 15 min ultrasonic bath in water, acetone, detergent solution (Semico Clean 56, Furuuchi chemical), water, and isopropanol, followed by drying with an air gun, and finally plasma treatment. The substrates were transferred to an inert gas filled glove box for further processing.

Preparation of Hole Collecting Layers

The PEDOT:PSS layer was fabricated from an aqueous dispersion which was filtered through a 0.45 μm PVDF filter and then spin coated on the TCO substrate using a spin program of 10 s at 500 rpm followed by 30 s at 4000 rpm. The films were then annealed in air at 140 °C for 20 min. After transferring to an Ar-filled glove box (H_2O, O_2 < 0.1 ppm), the substrates were degassed at 140 °C for 30 min.

The hole collecting material PTAA (2.0 mg mL^{-1} in anhydrous toluene) was deposited using spin-coating (4000 rpm for 30 s, 5 s acceleration), followed by heating on a hot plate at 100 °C for 10 min.

The hole collecting monolayer **MeO-2PACz** (1.0 mmol L^{-1} in anhydrous ethanol) was deposited using spin-coating (3000 rpm for 30 s, 5 s acceleration), followed by heating on a hot plate at 100 °C for 10 min.[11]

The DMF solution of **1PATAT-C3** (1.0 mmol L^{-1}), **2PATAT-C3** (0.1 mmol L^{-1}), **3PATAT-C3** (0.1 mmol L^{-1}), and **3PATAT-C4** (0.1 mmol L^{-1}) were deposited using spin-coating (3000 rpm for 30 s, 5 s acceleration), followed by heating on a hot plate at 110 °C for 10 min.

Fabrication of $Cs_{0.05}FA_{0.80}MA_{0.15}PbI_{2.75}Br_{0.25}$ Layer

The precursor solution was prepared from CsI (69 mg, 0.27 mmol), MABr (85 mg, 0.76 mmol), PbI_2 (2.24 g, 4.85 mmol), $PbBr_2$ (96 mg, 0.26 mmol), and FAI (703 mg, 4.09 mmol) dissolved in a mixture of DMF (3.0 mL) and DMSO (0.90 mL). After stirring at 40 °C for 30 min, the solution was filtered with a 0.45 μm PTFE filter. 190 μL of the solution was placed on a TCO/HCM substrate and spread by spin-coating (slope 1 s, 1000 rpm 10 s, slope 5 s, 6000 rpm 20 s, slope 1 s) to make a thin film. 300 μL of chlorobenzene was dripped over the rotating substrate at 3 s before the end of the spinning at 6000 rpm. The films were then annealed on a hot plate at 150 °C for 10 min.

For $EDAI_2$ surface treatment: The above perovskite samples were moved under Ar to a vacuum deposition chamber, where 0.5 nm of $EDAI_2$ (deposition rate 0.01 nm s^{-1}) was deposited by thermal evaporation.

Fabrication of Electron Transporting Layer and Metal Electrode

The above samples were moved under Ar to a vacuum deposition chamber, where 20 nm of C_{60} (deposition rate 0.05 nm s^{-1}) and 8 nm of BCP (deposition rate 0.01 nm s^{-1}) were deposited by thermal evaporation.

The top electrode was prepared by depositing 100 nm of silver (deposition rate 0.005 nm s^{-1}) through a shadow mask.

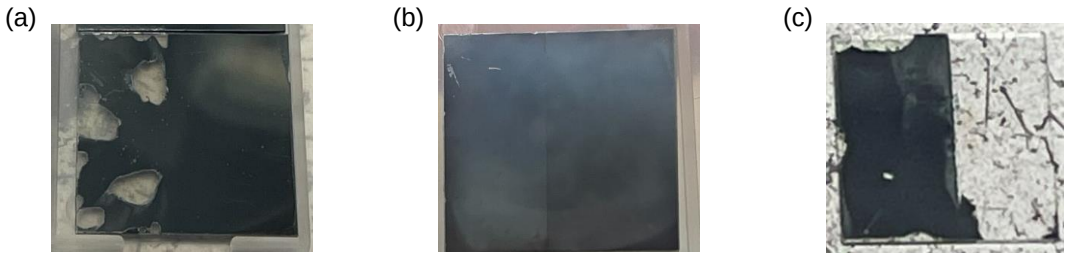

FTO/PTAA/Perovskite

FTO/**3PATAT-C3** (spin coated from DMF) /Perovskite

FTO/**3PATAT-C3** (spin coated from DMSO) /Perovskite

Figure S13. Photos of perovskite films fabricated on FTO/PTAA and FTO/**3PATAT-C3** substrates.

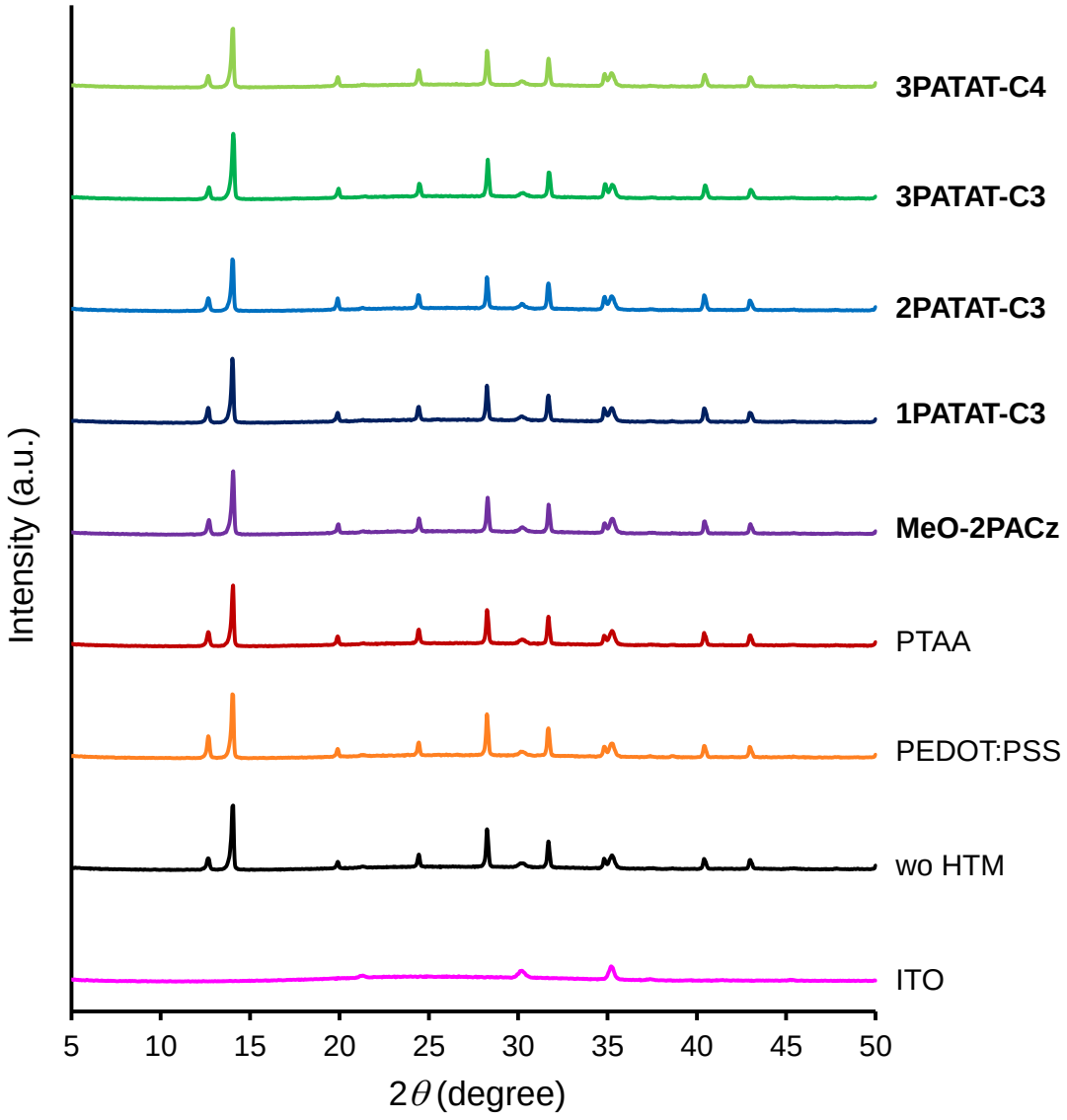

Figure S14. XRD spectra of perovskite films deposited on different ITO/HCM substrates.

(a) bare ITO

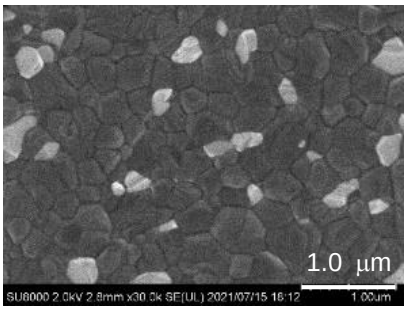

(b) ITO/PEDOT:PSS

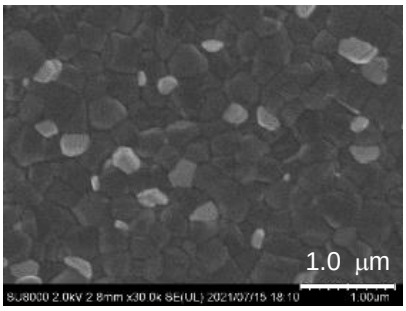

(c) ITO/PTAA

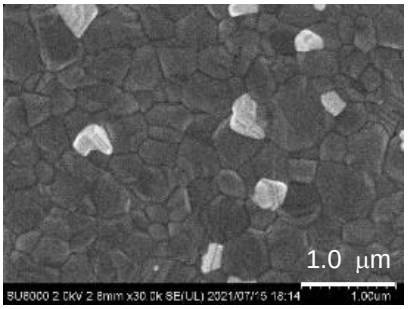

(d) ITO/**MeO-2PACz**

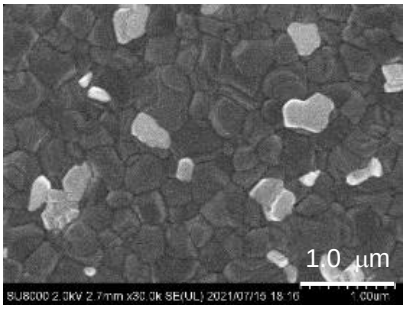

(e) ITO/**1PATAT-C3**

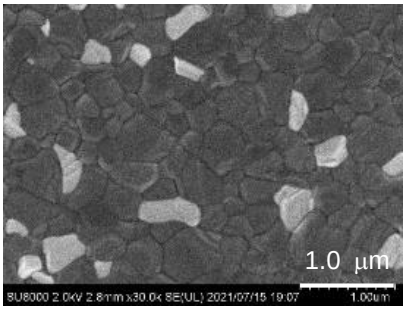

(f) ITO/**2PATAT-C3**

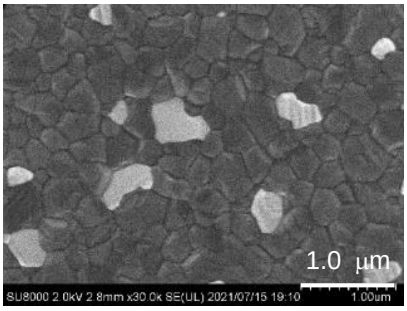

(g) ITO/**3PATAT-C3**

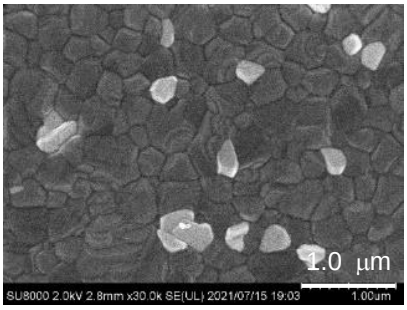

(h) ITO/**3PATAT-C4**

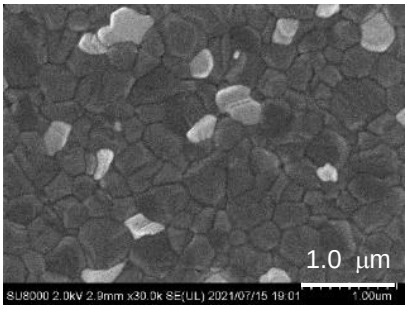

Figure S15. Top-view SEM images of perovskite films deposited on different ITO/HCM substrates.

(a) Bare ITO

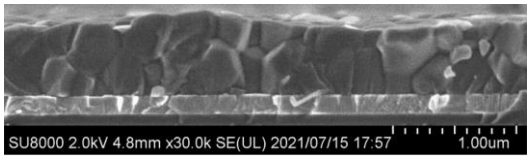

(b) ITO/PEDOT:PSS

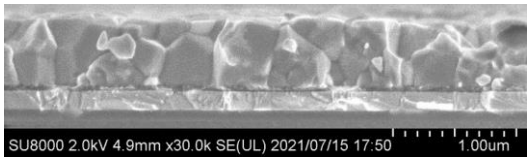

(c) ITO/PTAA

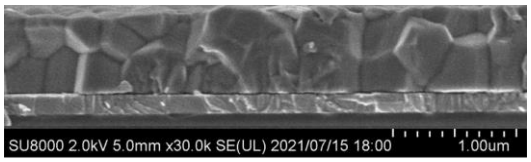

(d) ITO/**MeO-2PACz**

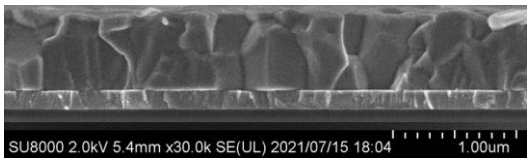

(e) ITO/**1PATAT-C3**

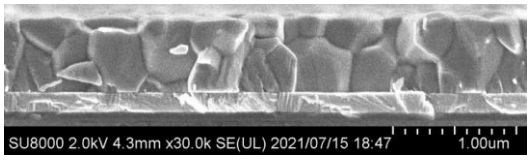

(f) ITO/**2PATAT-C3**

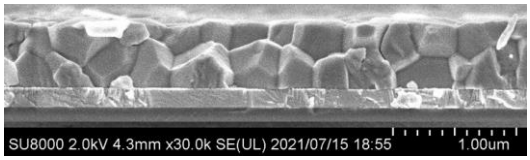

(g) ITO/**3PATAT-C3**

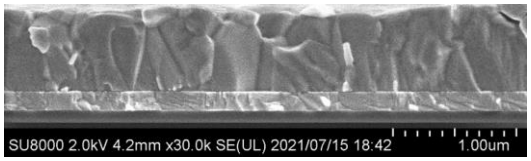

(h) ITO/**3PATAT-C4**

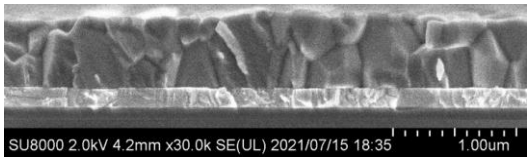

Figure S16. Cross-sectional SEM images of perovskite films fabricated on different ITO/HCM substrates.

(a) FTO/PTAA

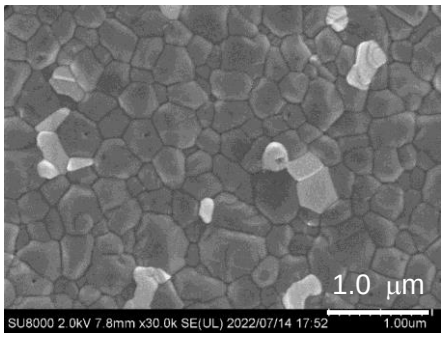

(b) FTO/**MeO-2PACz**

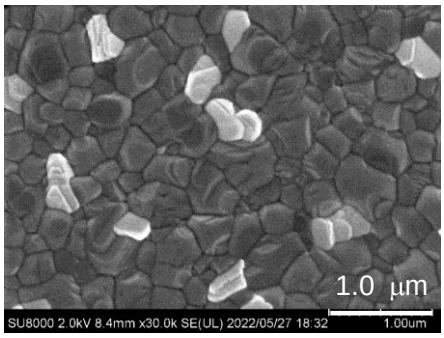

(c) FTO/**1PATAT-C3**

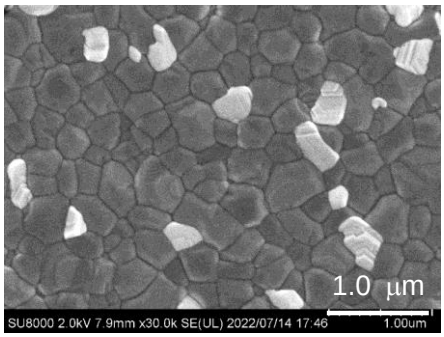

(d) FTO/**2PATAT-C3**

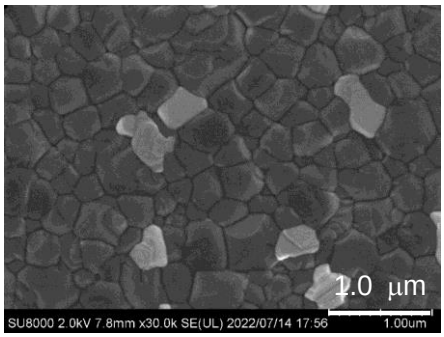

(e) FTO/**3PATAT-C3**

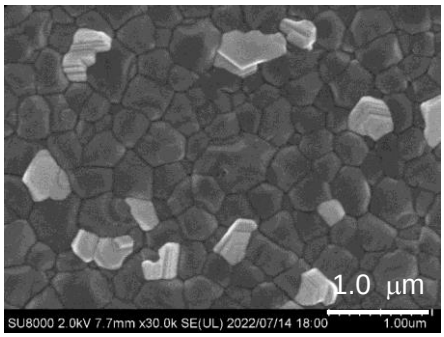

(f) FTO/**3PATAT-C4**

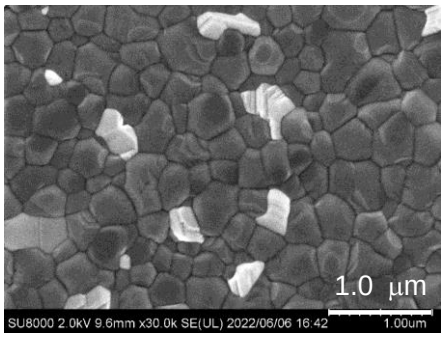

Figure S17. Top-view SEM images of perovskite films deposited on different FTO/HCM substrates.

(a) Bare FTO

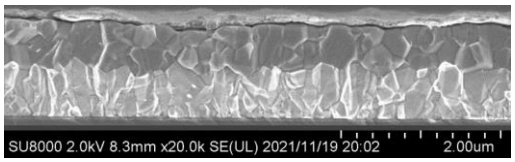

(b) FTO/PEDOT:PSS

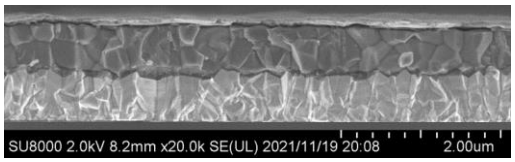

(c) FTO/PTAA

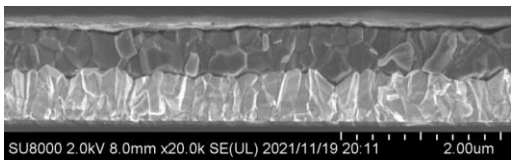

(d) FTO/**MeO-2PACz**

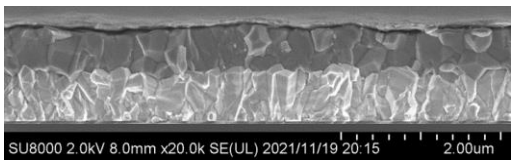

(e) FTO/**1PATAT-C3**

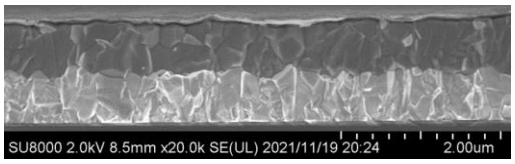

(f) FTO/**2PATAT-C3**

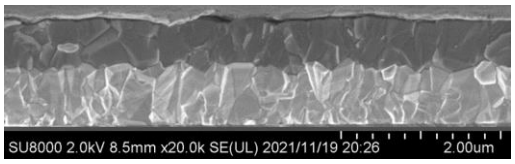

(g) FTO/**3PATAT-C3**

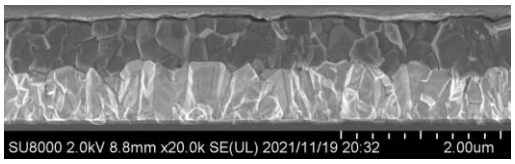

(h) FTO/**3PATAT-C4**

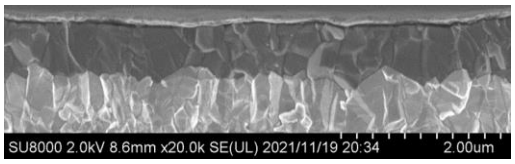

Figure S18. Cross-sectional SEM images of PSCs fabricated on different FTO/HCM substrates.

For Devices using ITO Substrates

The performance of the ITO-based PSC devices was evaluated under AM 1.5 G simulated sunlight and shown in **Figure S19–S21**. The corresponding photovoltaic parameters are also summarized in **Table S2** and **S3**. The device based on tripodal **3PATAT-C3** exhibits the best performance with a PCE of 19.5% and 20.1% obtained under forward and reverse scan conditions. The statistical PCE distribution of the PSC devices in the forward scan are shown in **Figure S22**. The average PCE values in the forward scan were 19.1, 19.0, 18.3, and 16.8% for **3PATAT-C3**, **2PATAT-C3**, **3PATAT-C4**, and **1PATAT-C3**, respectively. Except monopodal **1PATAT-C3**, devices using **PATAT** molecules as hole collecting monolayer materials show slightly higher performance than those using **MeO-2PACz** monolayer and PTAA. PEDOT:PSS-based and HCM free devices showed poor performance of less than 8%.

The V_{OC} depends on the component and electronic structures such as band gap, valence band, etc. of perovskite material. In case of ITO/**MeO-2PACz**, the V_{OC} was reported to be lower when perovskite with narrower bandgap was used.

Table S1. V_{OC} Data of Reported PSCs Fabricated on ITO/MeO-2PACz Substrates

Perovskite	Bandgap (eV)	V_{OC} (V)	References
$Cs_{0.05}FA_{0.79}MA_{0.16}PbI_{2.49}Br_{0.51}$	1.63	1.14	Al-Ashouri, A et al. *Energy Environ. Sci.* **2019**, *12*, 3356–3369.
$Cs_{0.05}FA_{0.87}MA_{0.08}PbI_{2.76}Br_{0.24}$	1.56	1.09	Zhang, S et al. *ACS Materials Lett.* **2022**, *4*, 1976–1983.
$Cs_{0.05}FA_{0.80}MA_{0.15}PbI_3$	1.56[a)]	1.02	Deng, X et al. *Angew. Chem., Int. Ed.* **2022**, *61*, e202203088.

[a)] The bandgap was estimated from Ozaki, M et al. *J. Mater. Chem. A* **2019**, *7*, 16947–16953.

In our work, we used $Cs_{0.05}FA_{0.80}MA_{0.15}PbI_{2.75}Br_{0.25}$ (bandgap = 1.57 eV) as the perovskite material. The champion V_{OC} of the device using ITO/**MeO-2PACz** without $EDAI_2$ surface treatment was 1.06 V, which is in good agreement with reported works using perovskite materials with similar bandgaps. When **3PATAT-C3** was used instead of **MeO-2PACz**, the champion V_{OC} increased to 1.09 V, indicating the advantage of face-on oriented molecule.

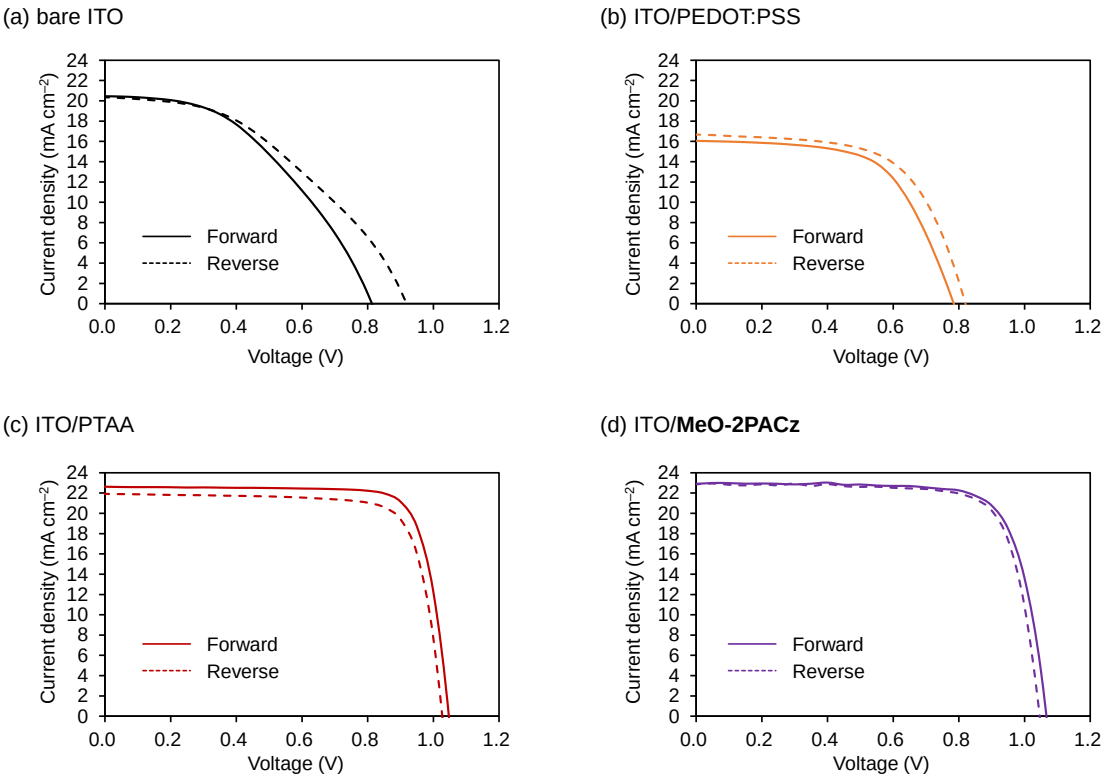

Figure S19. *J–V* curves of PSCs fabricated on (a) bare ITO, (b) ITO/PEDOT:PSS, (c) ITO/PTAA, and (d) ITO/**MeO-2PACz** substrate.

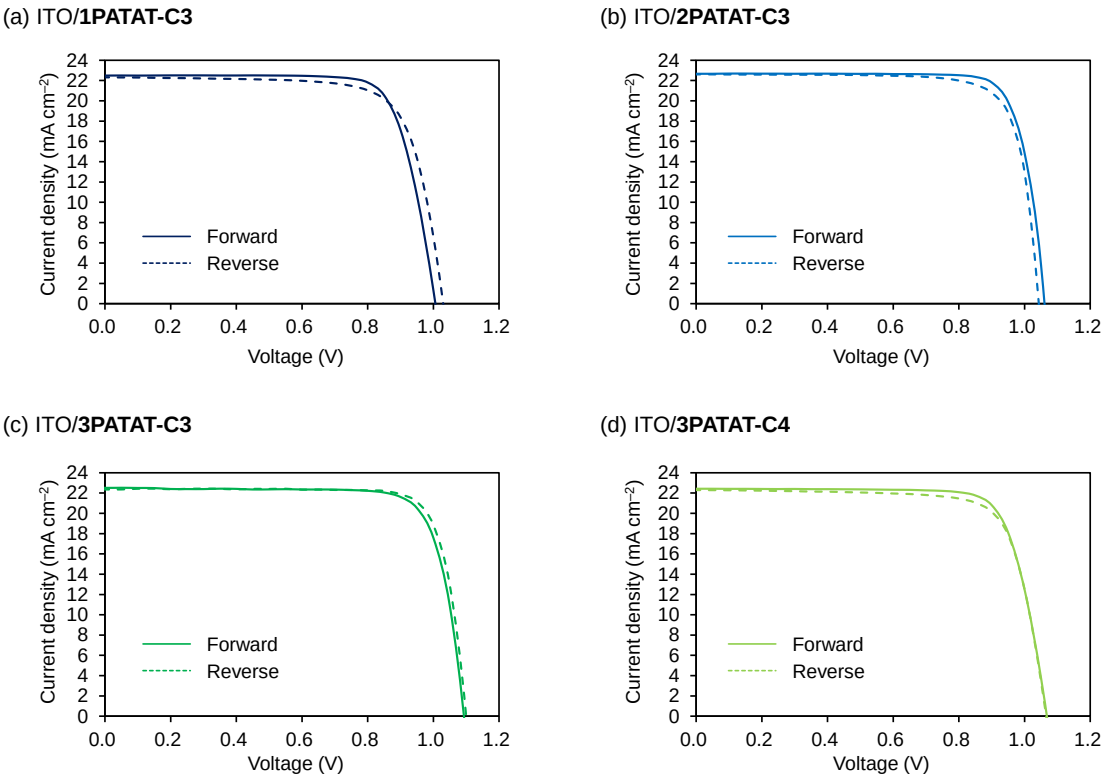

Figure S20. *J–V* curves of PSCs fabricated on (a) ITO/**1PATAT-C3**, (b) ITO/**2PATAT-C3**, (c) ITO/**3PATAT-C3**, and (d) ITO/**3PATAT-C4** substrate.

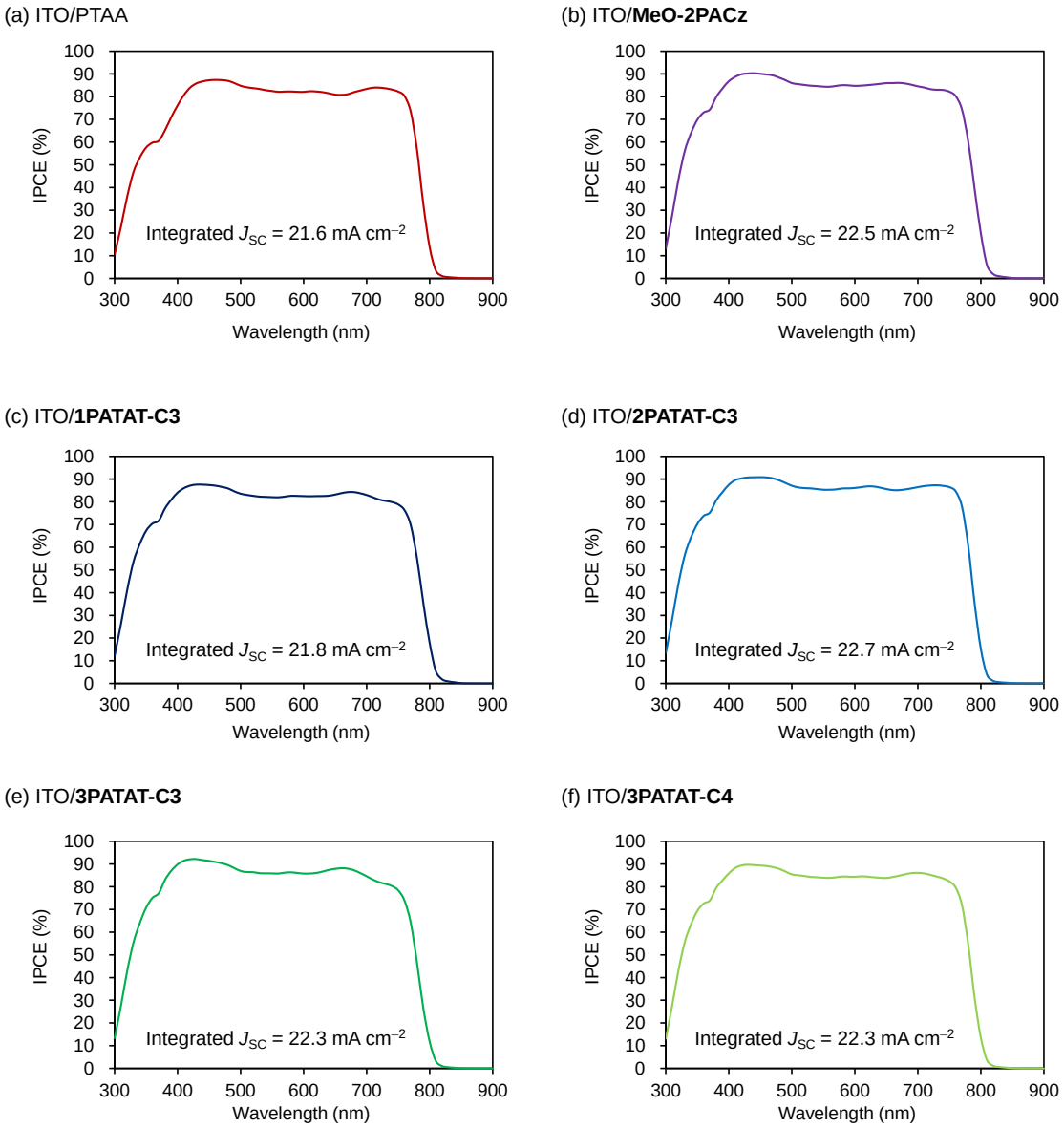

Figure S21. IPCE spectra of PSCs fabricated on (a) ITO/PTAA, (b) ITO/**MeO-2PACz**, (c) ITO/**1PATAT-C3**, (d) ITO/**2PATAT-C3**, (e) ITO/**3PATAT-C3**, and (f) ITO/**3PATAT-C4** substrate.

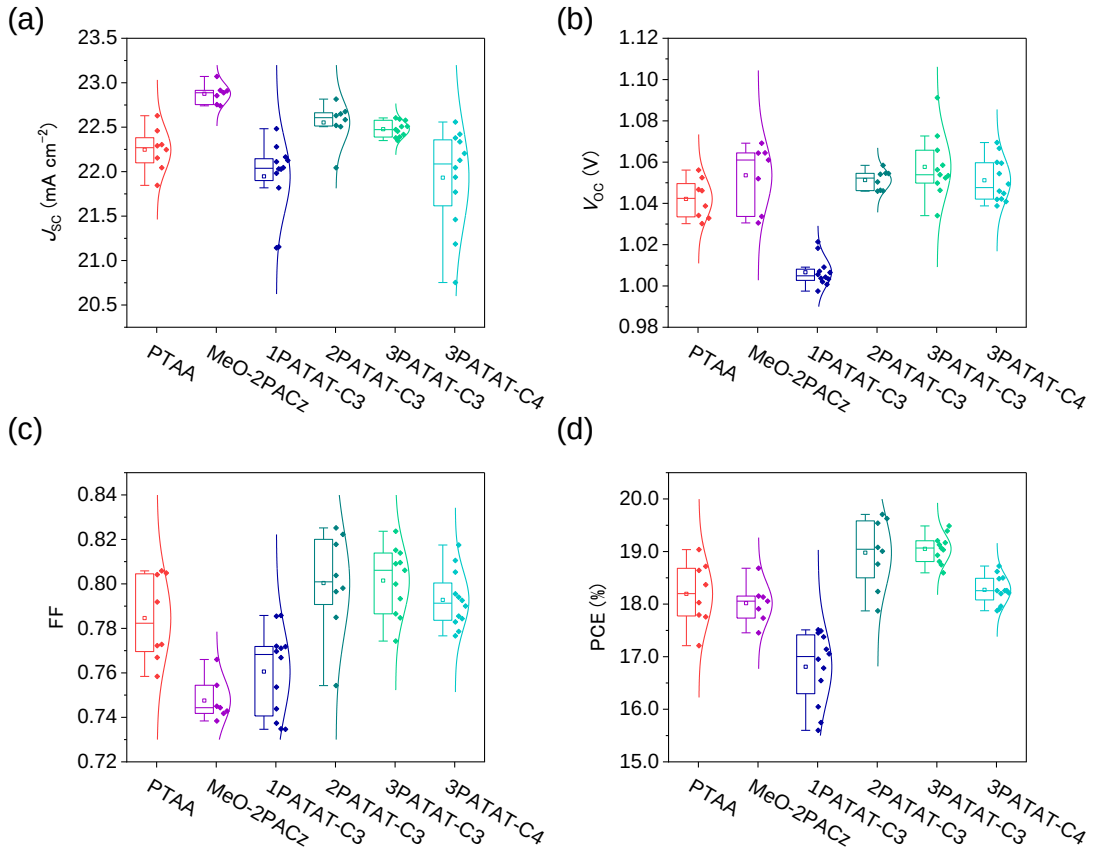

Figure S22. Box plots of (a) J_{SC}, (b) V_{OC}, (c) FF, and (d) PCE of the PSCs fabricated by using ITO/PTAA, ITO/**MeO-2PACz**, ITO/**1PATAT-C3**, ITO/**2PATAT-C3**, ITO/**3PATAT-C3**, and ITO/**3PATAT-C4** substrates obtained in the forward scan.

Table S2. Photovoltaic Parameters of PSCs Fabricated on Different ITO/Conventional HCM Substrates Derived from *J–V* Measurements

HCM[a]	Scan[b]	J_{SC} [mA cm^{-2}][c]	V_{OC} [V][c]	FF[c]	PCE [%][c]	HI[d]
MeO-2PACz	Forward	22.9	1.06	0.77	18.7	
		(22.9 ± 0.1)	(1.05 ± 0.01)	(0.75 ± 0.01)	(18.0 ± 0.4)	–0.027
	Reverse	22.9	1.05	0.76	18.2	
		(22.8 ± 0.1)	(1.05 ± 0.01)	(0.76 ± 0.01)	(18.2 ± 0.4)	
PTAA	Forward	22.6	1.05	0.80	19.0	
		(22.2 ± 0.2)	(1.04 ± 0.01)	(0.78 ± 0.02)	(18.2 ± 0.6)	–0.086
	Reverse	21.9	1.02	0.78	17.5	
		(21.9 ± 0.2)	(1.03 ± 0.01)	(0.76 ± 0.02)	(17.1 ± 0.6)	
PEDOT:PSS	Forward	16.1	0.78	0.60	7.6	
		(14.7 ± 0.8)	(0.77 ± 0.03)	(0.61 ± 0.02)	(6.9 ± 0.7)	–0.084
	Reverse	16.7	0.82	0.61	8.3	
		(15.4 ± 0.9)	(0.80 ± 0.02)	(0.61 ± 0.02)	(7.6 ± 0.7)	
none	Forward	20.4	0.81	0.44	7.4	
		(20.0 ± 0.3)	(0.82 ± 0.01)	(0.43 ± 0.01)	(7.1 ± 0.2)	0.063
	Reverse	20.3	0.92	0.43	7.9	
		(20.0 ± 0.4)	(0.92 ± 0.01)	(0.41 ± 0.01)	(7.6 ± 0.3)	

[a] HCMs were spin-coated on ITO substrates; [b] Forward and reverse indicate the scan direction from J_{SC} to V_{OC} and from V_{OC} to J_{SC}, respectively; [c] The average and standard deviation values were given in parentheses; [d] Hysteresis index (HI) = ($PCE_{Reverse}$ – $PCE_{Forward}$)/$PCE_{Reverse}$.

Table S3. Photovoltaic Parameters of PSCs Fabricated on Different ITO/PATAT-based HCM Substrates Derived from *J–V* Measurements

HCM[a)]	Scan[b)]	J_{SC} [mA cm^{-2}][c)]	V_{OC} [V][c)]	FF[c)]	PCE [%][c)]	HI[d)]
3PATAT-C4	Forward	22.4	1.07	0.78	18.7	
		(21.9 ± 0.5)	(1.05 ± 0.01)	(0.79 ± 0.01)	(18.3 ± 0.3)	–0.033
	Reverse	22.3	1.06	0.76	18.1	
		(21.9 ± 0.5)	(1.04 ± 0.01)	(0.75 ± 0.03)	(17.1 ± 0.8)	
3PATAT-C3	Forward	22.5	1.09	0.79	19.5	
		(22.5 ± 0.1)	(1.06 ± 0.01)	(0.80 ± 0.01)	(19.1 ± 0.3)	0.030
	Reverse	22.4	1.10	0.82	20.1	
		(22.4 ± 0.1)	(1.04 ± 0.03)	(0.77 ± 0.03)	(18.0 ± 1.1)	
2PATAT-C3	Forward	22.7	1.06	0.82	19.6	
		(22.6 ± 0.2)	(1.05 ± 0.01)	(0.80 ± 0.02)	(19.0 ± 0.6)	–0.048
	Reverse	22.6	1.04	0.80	18.7	
		(22.5 ± 0.2)	(1.03 ± 0.01)	(0.76 ± 0.02)	(17.5 ± 0.7)	
1PATAT-C3	Forward	22.5	1.01	0.77	17.5	
		(21.9 ± 0.4)	(1.01 ± 0.01)	(0.76 ± 0.02)	(16.8 ± 0.7)	–0.023
	Reverse	22.3	1.03	0.75	17.1	
		(21.7 ± 0.4)	(1.00 ± 0.01)	(0.67 ± 0.04)	(14.6 ± 1.2)	

[a)] HCMs were spin-coated on ITO substrates; [b)] Forward and reverse indicate the scan direction from J_{SC} to V_{OC} and from V_{OC} to J_{SC}, respectively; [c)] The average and standard deviation values were given in parentheses; [d)] Hysteresis index (HI) = ($PCE_{Reverse}$ – $PCE_{Forward}$)/$PCE_{Reverse}$.

For Comparison of Devices using ITO and FTO Substrates:

As shown in **Figure S23a**, high reflection (>10%) which can be attributed to the interference of planar ITO thin film was observed over the spectral range of 400–750 nm. This reflection loss resulted in a reduction of corresponding incident photon-to-current efficiency (IPCE). In contrast to planar ITO substrates, textured FTO substrates are reported to have less optical interference in the visible spectrum. Therefore, FTO substrates were used in this work to maximize the output current of the devices. As shown in **Figure S23b**, the reflectance of FTO based device is significantly lower than ITO based device over the spectral range of 400–750 nm, e.g., 2.7 times lower at around 550 nm (4.6% for FTO vs 12.7% for ITO). In line with the above results, the IPCE at a wavelength shorter than 400 nm is quite similar for both the FTO and ITO based PSCs, while it is clearly higher for the textured FTO based PSCs over the rest of the spectrum, resulting in an integrated short-circuit current density (J_{SC}) of 24.0 mA cm^{-2} as compared to 22.3 mA cm^{-2} for the planar ITO. Consequently, the PCE of **3PATAT-C3** based PSCs fabricated on FTO substrates significantly increases up to 21.0% (**Table S4**, **Figure S23c**). However, the improvement in open-circuit voltage (V_{oc}) was not observed in this case (**Figure S24**).

(a) ITO/**3PATAT-C3**

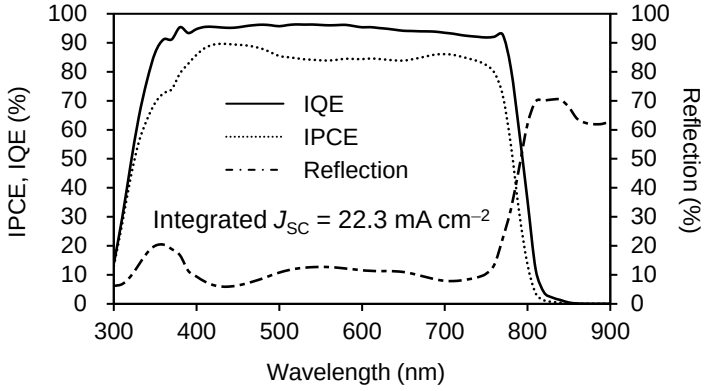

(b) FTO/**3PATAT-C3**

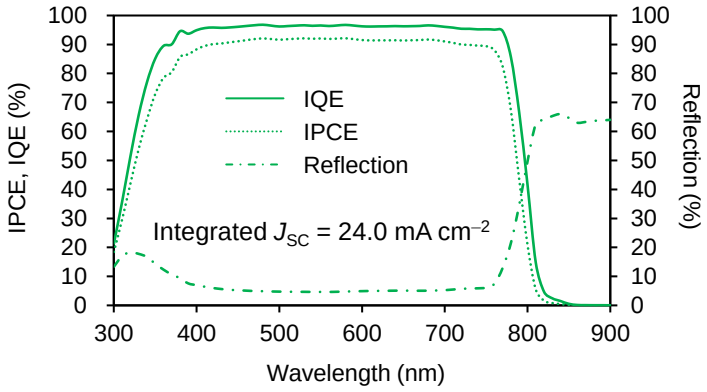

(c) FTO/**3PATAT-C3**

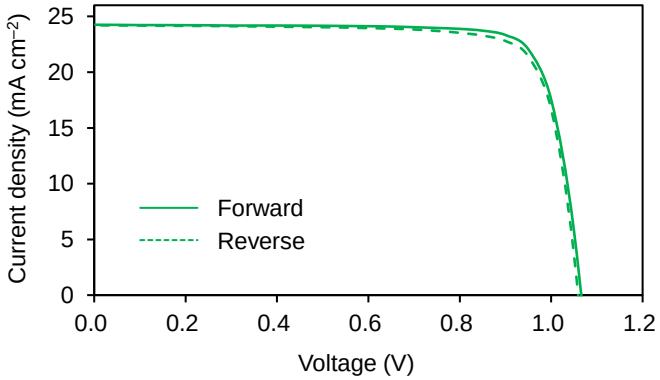

Figure S23. IPCE, IQE, and reflection spectra of PSCs fabricated on (a) ITO/**3PATAT-C3** and (b) FTO/**3PATAT-C3**, and (c) *J*–*V* curves of PSCs fabricated on FTO/**3PATAT-C3** without $EDAI_2$ surface treatment.

Table S4. Photovoltaic Parameters of PSCs Fabricated on ITO/3PATAT-C3 and FTO/3PATAT-C3 Substrates Derived from *J–V* Measurements

Substrate	Scan[a)]	J_{SC} [mA cm^{-2}][b)]	V_{OC} [V][b)]	FF[b)]	PCE [%][b)]	HI[c)]
ITO	Forward	22.5	1.09	0.79	19.5	0.030
		(22.5 ± 0.1)	(1.06 ± 0.01)	(0.80 ± 0.01)	(19.1 ± 0.3)	
	Reverse	22.4	1.10	0.82	20.1	
		(22.4 ± 0.1)	(1.04 ± 0.03)	(0.77 ± 0.03)	(18.0 ± 1.1)	
FTO	Forward	24.3	1.06	0.81	21.0	–0.024
		(24.0 ± 0.3)	(1.06 ± 0.01)	(0.78 ± 0.02)	(20.0 ± 0.8)	
	Reverse	24.2	1.06	0.80	20.5	
		(24.0 ± 0.3)	(1.05 ± 0.01)	(0.78 ± 0.01)	(19.5 ± 0.5)	

[a)] Forward and reverse indicate the scan direction from J_{SC} to V_{OC} and from V_{OC} to J_{SC}, respectively; [b)] The average and standard deviation values were given in parentheses; [c)] Hysteresis index (HI) = $(PCE_{Reverse} – PCE_{Forward})/PCE_{Reverse}$.

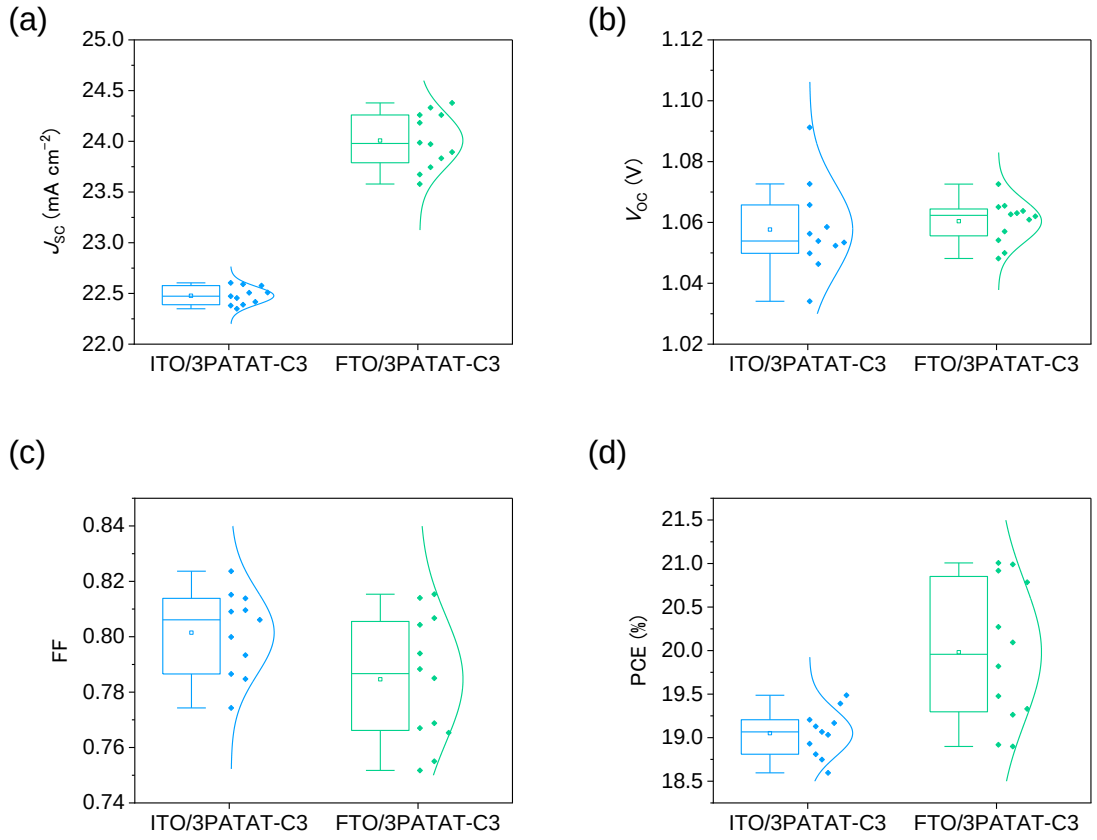

Figure S24. Box plots of (a) J_{SC}, (b) V_{OC}, (c) FF, and (d) PCE of the PSCs fabricated by using ITO/**3PATAT-C3** and FTO/**3PATAT-C3** substrates obtained in the forward scan.

We confirmed the effectiveness of DMF as the solvent for the fabrication of the **3PATAT-C3** monolayers. **3PATAT-C3** monolayers were spin-coated from DMF, MeOH, or NMP solutions and their respective device performance was compared. Monolayers fabricated from DMF solution were found to give the highest device performance (**Figure S25**).

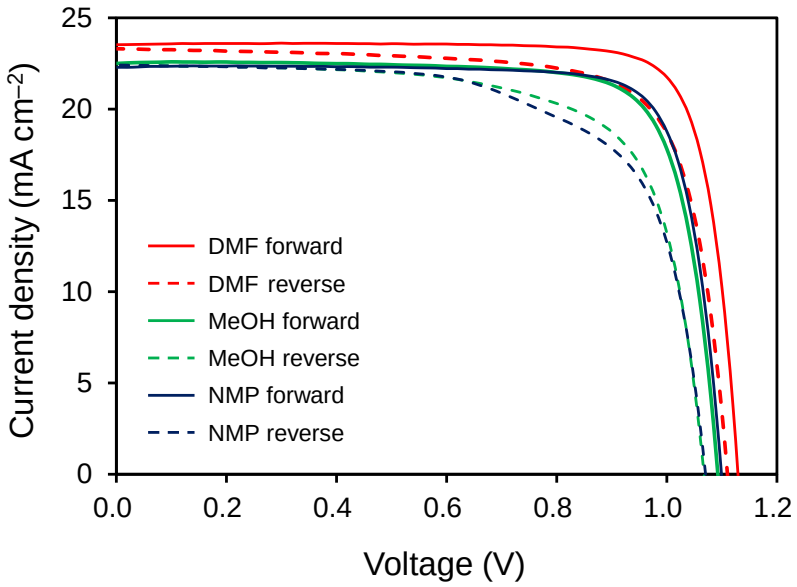

Solvent	Scan	J_{sc} (mA cm^{-2})	V_{oc} (V)	FF	PCE (%)
DMF	Forward	23.5	1.13	0.82	21.8
	Reverse	23.3	1.11	0.76	19.6
MeOH	Forward	22.5	1.09	0.79	19.4
	Reverse	22.4	1.07	0.71	16.9
NMP	Forward	22.3	1.10	0.81	19.8
	Reverse	22.4	1.07	0.67	16.1

Figure S25. *J–V* curves of PSCs fabricated on FTO/**3PATAT-C3** using DMF, MeOH, and NMP as a solvent for **3PATAT-C3**.

According to the CV measurements (**Figure S10–S11**), the adsorption density of **PATAT** molecules on ITO substrates increased when high concentration (1.0 mM) was used. With the expectation that high concentration of **PATAT** derivatives can improve device performance, we fabricated and compared devices using 0.1 mM and 1.0 mM **PATAT** solutions. Conversely, we found that PSCs fabricated by using multipodal molecules from 0.1 mM solution showed higher performance with higher V_{OC}, FF, and better reproducibility (**Figure S26**). Considering the device performance, we decided to prepare **2PATAT-C3**, **3PATAT-C3** and **3PATAT-C4** monolayers from 0.1 mM solutions, while **1PATAT-C3** monolayer was fabricated by using 1.0 mM solution.

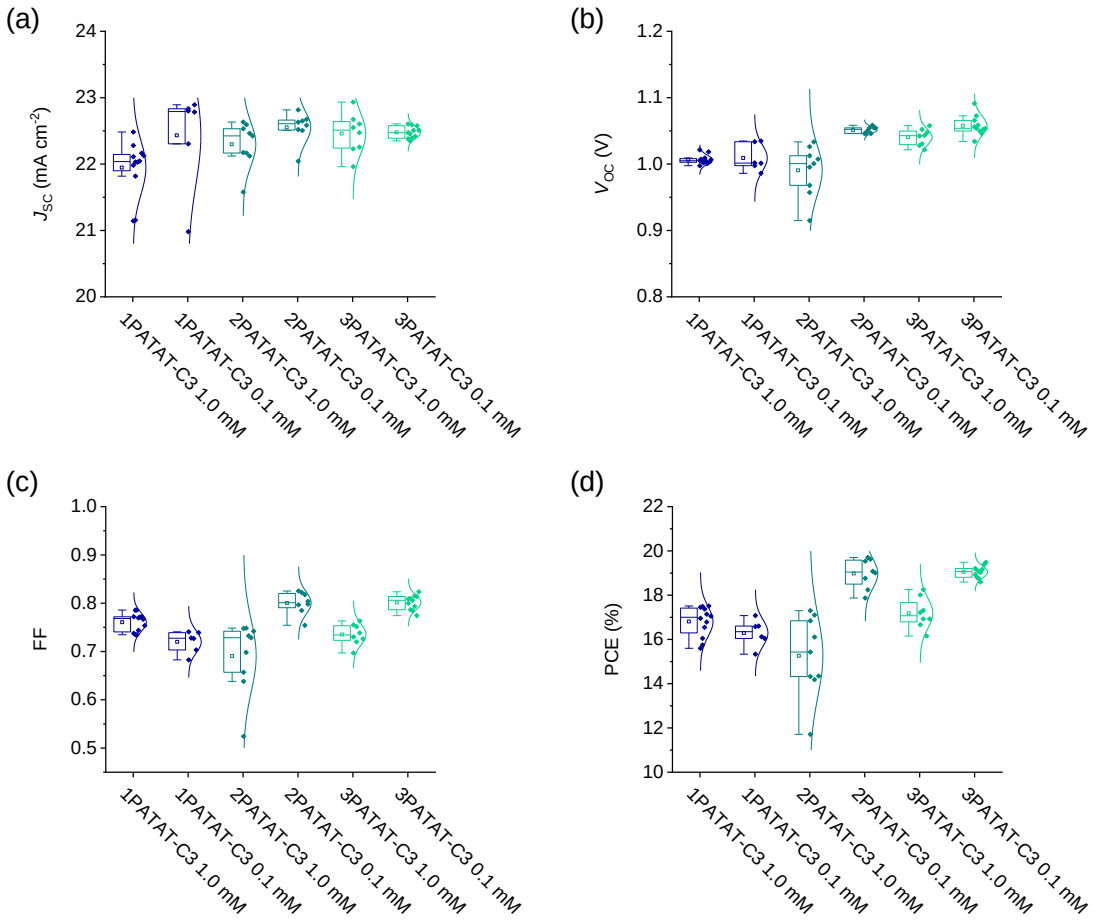

Figure S26. Box plots of (a) J_{SC}, (b) V_{OC}, (c) FF, and (d) PCE of the PSCs fabricated by using ITO/**1PATAT-C3**, ITO/**2PATAT-C3**, and ITO/**3PATAT-C3** substrates with 0.1 mM and 1.0 mM **PATAT** precursor in DMF solutions obtained in the forward scan.

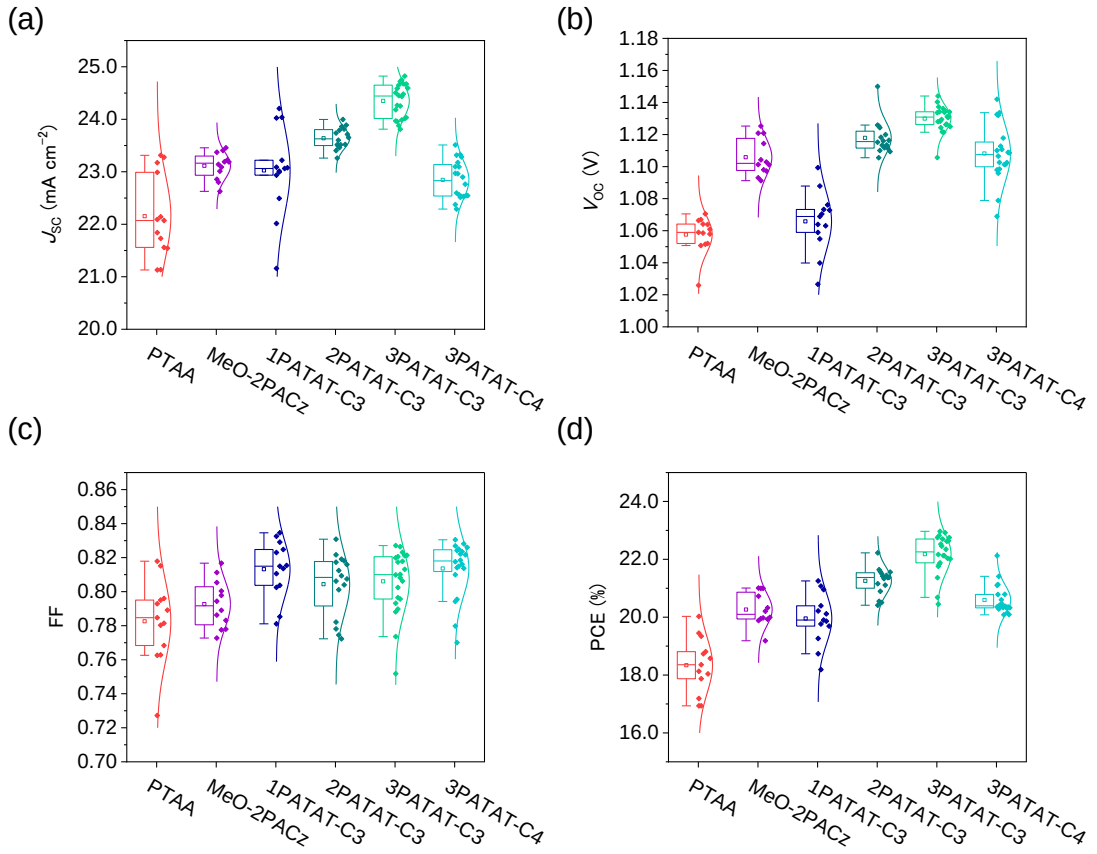

Figure S27. Box plots of (a) J_{SC}, (b) V_{OC}, (c) FF, and (d) PCE of the PSCs fabricated by using FTO/PTAA, FTO/**MeO-2PACz**, FTO/**1PATAT-C3**, FTO/**2PATAT-C3**, FTO/**3PATAT-C3**, and FTO/**3PATAT-C4** substrates with $EDAI_2$ treatment on perovskite surface.

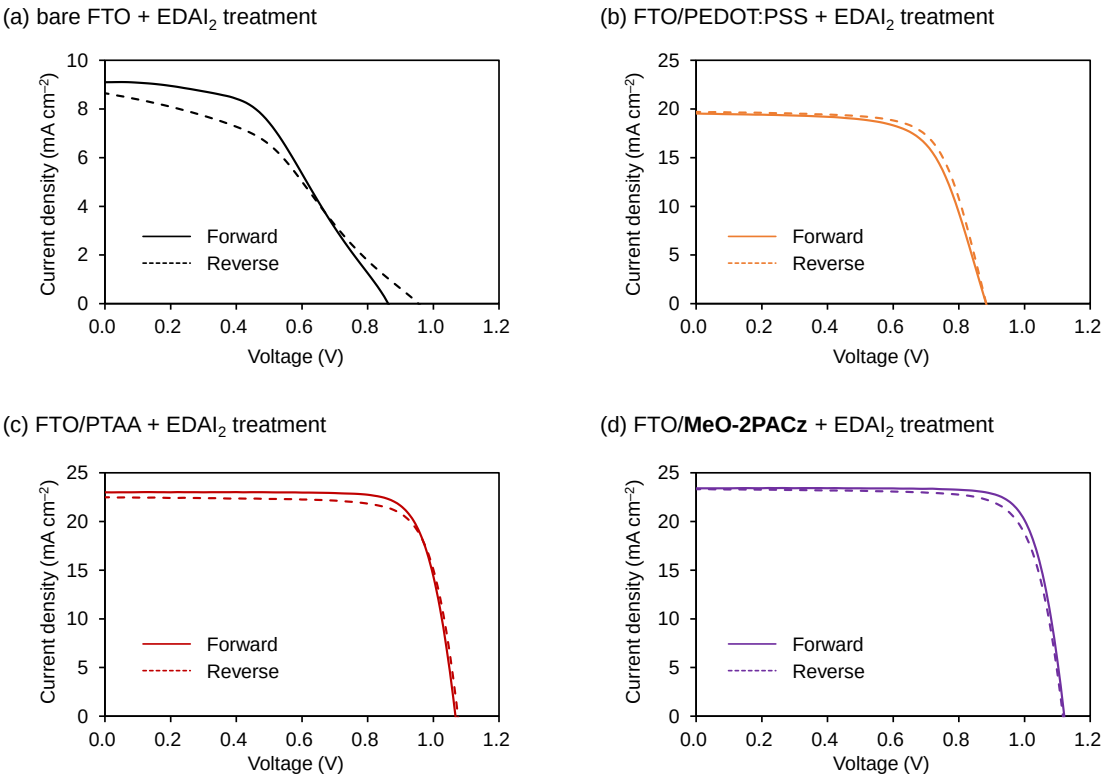

Figure S28. *J–V* curves of PSCs fabricated on (a) bare FTO, (b) FTO/PEDOT:PSS, (c) FTO/PTAA, and (d) FTO/**MeO-2PACz** substrate with $EDAI_2$ treatment on perovskite surface.

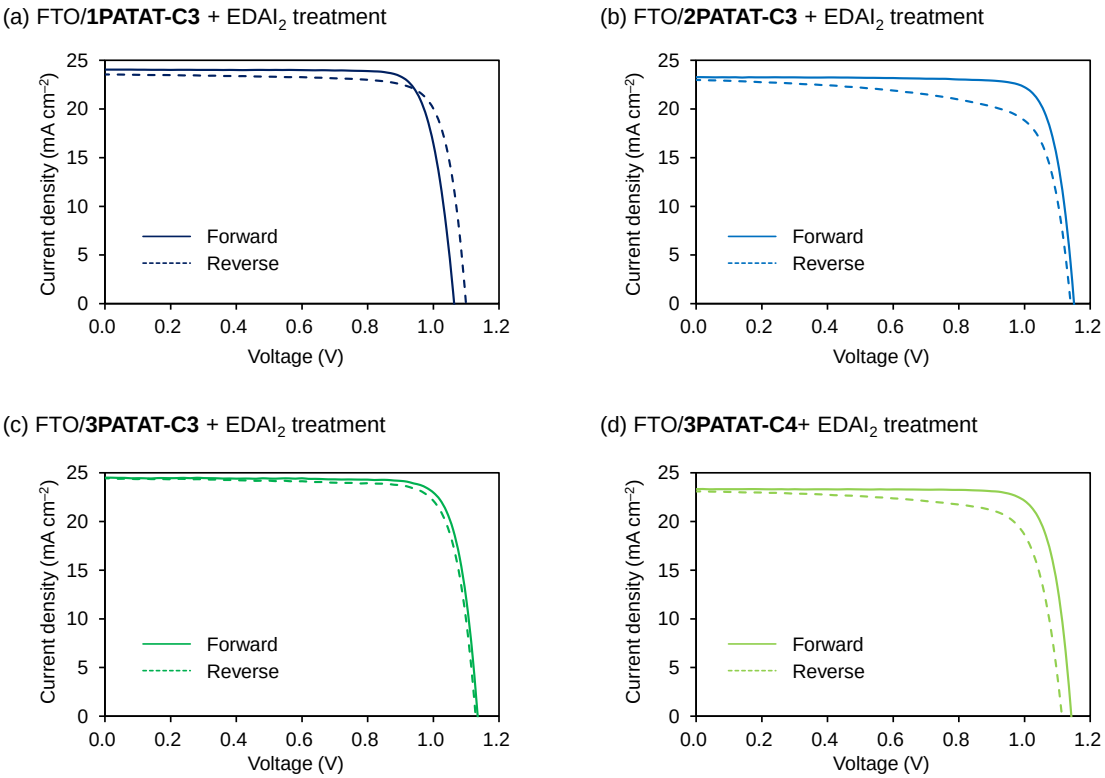

Figure S29. *J–V* curves of PSCs fabricated on (a) FTO/**1PATAT-C3**, (b) FTO/**2PATAT-C3**, (c) FTO/**3PATAT-C3**, and (d) FTO/**3PATAT-C4** substrate with $EDAI_2$ treatment on perovskite surface.

Table S5. Reports on TCO-Anchorable Molecules for Inverted PSCs

Molecules	Champion PCE (Average PCE)	References
CbzNaph	24.1%[1] (21.4%)	Jiang, W.; Jen, A. K.-Y. *et al*. *Angew. Chem. Int. Ed.* **2022**, e202213560.
DC-PA/IAHA co-adsorption	23.59%[2] (20.62%)	Deng, X.; Jen, A. K.-Y. *et al*. *Angew. Chem. Int. Ed.* **2022**, e202203088.
3PATAT-C3	**23.0% (22.2%)**	**This Work**
2BrPXZPA	22.93%[3] (22.56%)	He, Z. *et al*. *Nanoscale* **2023**, *15*, 1676–1686.
Br-2EPSe	22.73%[4] (22.36%)	Ullah, A.; Hong, S. *et al*. *Adv. Funct. Mater.* **2022**, 2208793.
MPA-Ph-CA	22.53%[5] (≈ 22%)	Zhang, S.; Zhu, W.-H. *et al. ACS Materials Lett.* **2022**, *4*, 1976–1983.
Br-2EPT	22.44%[6] (21.81%)	Ullah, A.; Hong, S. *et al*. *Adv. Energy Mater.* **2022**, *12*, 2103175.
MPA-BT-CA	21.81%[7] (no data)	Liao, Q.; Guo, X. *et al*. *J. Energy Chem.* **2021**, *68*, 87–95.
TPT-P6	21.43%[8] (20.77%)	Li, E.; Zhu, W.-H. *et al*. *Adv. Energy Mater.* **2021**, 2103847.
EADR03/LiF/ AR coating	21.2%[9] (< 20%)	Aktas, E.; Palomares, E. *et al*. *Energy Environ. Sci.* **2021**, *14*, 3976–3985.
2PACz	20.9%[10] (< 20%)	Al-Ashouri, A.; Albrecht, S. *et al*. *Energy Environ. Sci.* **2019**, *12*, 3356–3369.
RC-24	19.8%[11] (< 19.5%)	Aktas, E.; Palomares, E. *et al*. *ACS Appl. Mater. Interfaces.* **2022**, *14*, 17461–17469.
Spiro-Acid	18.15%[12] (17.63%)	Li, W.; Palomares, E. *et al*. *ACS Appl. Energy Mater.* **2023**, *6*, 1239–1247.
V1036/C4 co-adsorption	17.8%[13] (15.78%)	Magomedov, A.; Getautis, V. *et al*. *Adv. Energy Mater.* **2018**, *8*, 1801892.
MC-43	17.3%[14] (16. 8%)	Yalcin, E.; Palomares, E. *et al*. *Energy Environ. Sci.* **2019**, *12*, 230–237.
TPA-PT-C6/CA-Br	17.5%[15]	Li, E.; Zhu, W.-H. *et al*. *Adv. Funct Mater.*

co-adsorption	(17.19%)	**2020**, *30*, 1909509.
TT1	14.85%[16] (12.89%)	Aktas, E.; Palomares, E. *et al*. *Nanoscale Horiz.* **2020**, *5*, 1415–1419.

[1] $Cs_{0.05}MA_{0.15}FA_{0.80}PbI_3$

[2] $Cs_{0.05}MA_{0.15}FA_{0.80}PbI_3$

[3] $Cs_{0.05}(FA_{0.85}MA_{0.15})_{0.95}Pb(I_{0.85}Br_{0.15})_3$, certified PCE: 22.38%

[4] $Cs_{0.05}(FA_{0.92}MA_{0.08})_{0.95}Pb(I_{0.92}Br_{0.08})_3$, certified PCE: 22.26%

[5] $Cs_{0.05}(FA_{0.92}MA_{0.08})_{0.95}Pb(I_{0.92}Br_{0.08})_3$, certified PCE: 22.12%

[6] $Cs_{0.05}(FA_{0.92}MA_{0.08})_{0.95}Pb(I_{0.92}Br_{0.08})_3$, certified PCE: 21.81%

[7] $(FA_{0.17}MA_{0.94}PbI_{3.11})_{0.95}(PbCl_2)_{0.05}$

[8] $Cs_{0.05}FA_{0.83}MA_{0.12}Pb(I_{0.85}Br_{0.15})_3$

[9] $Cs_{0.05}FA_{0.79}MA_{0.16}Pb(I_{0.84}Br_{0.16})_3$

[10] $Cs_{0.05}(FA_{0.83}MA_{0.17})_{0.95}Pb(I_{0.83}Br_{0.17})_3$, certified PCE: 20.7%

[11] $Cs_{0.05}FA_{0.79}MA_{0.16}Pb(I_{0.84}Br_{0.16})_3$

[12] $Cs_{0.05}(FA_{0.85}MA_{0.15})Pb(I_{0.85}Br_{0.15})_3$

[13] $Cs_{0.05}(FA_{0.83}MA_{0.17})_{0.95}Pb(I_{0.83}Br_{0.17})_3$

[14] $MAPbI_3$

[15] $MAPbI_3$

[16] $MAPbI_3$

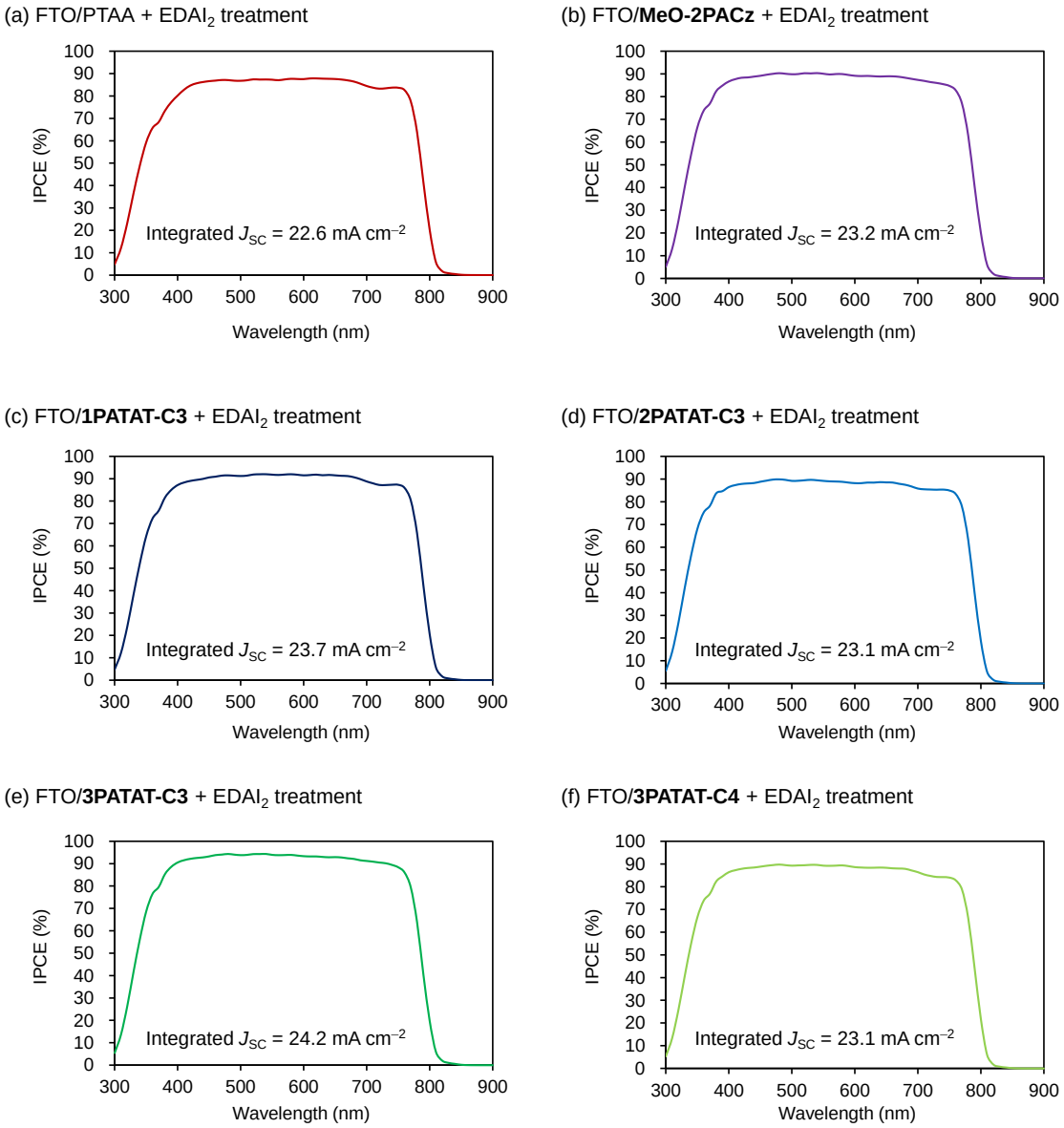

Figure S30. IPCE spectra of PSCs fabricated on (a) FTO/PTAA, (b) FTO/**MeO-2PACz**, (c) FTO/**1PATAT-C3**, (d) FTO/**2PATAT-C3**, (e) FTO/**3PATAT-C3**, and (f) FTO/**3PATAT-C4** substrate with $EDAI_2$ treatment on perovskite surface.

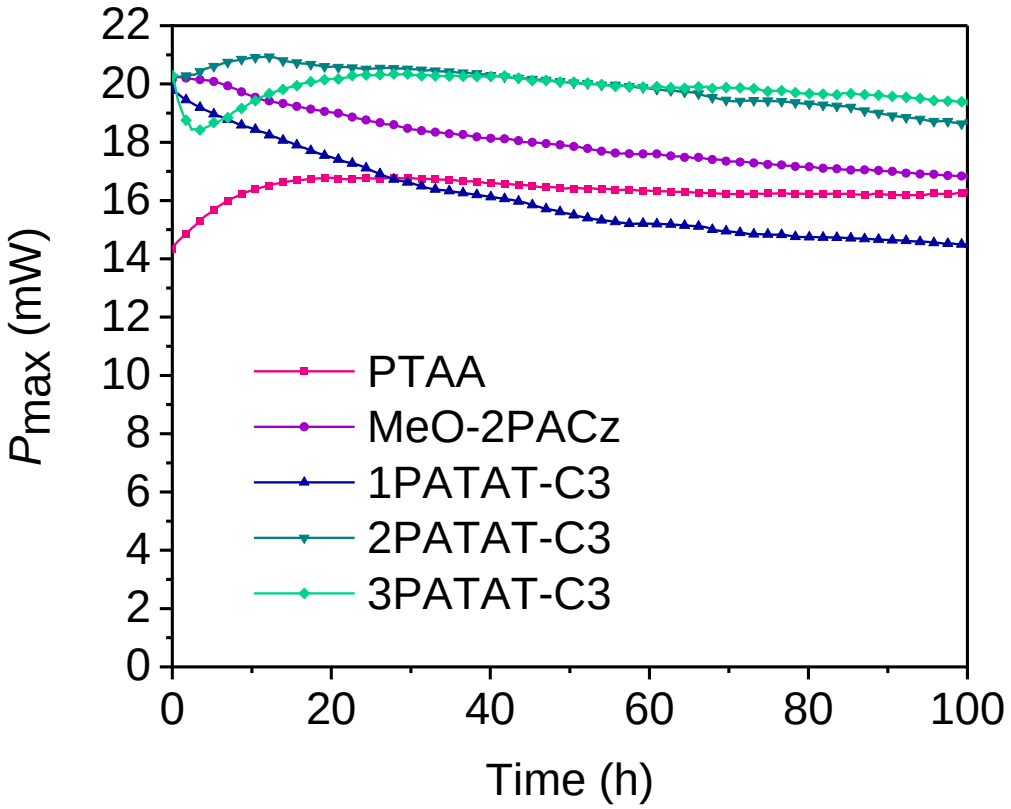

Figure S31. Maximum power point tracking data for the unencapsulated PSCs (AM 1.5G in an inert atmosphere).

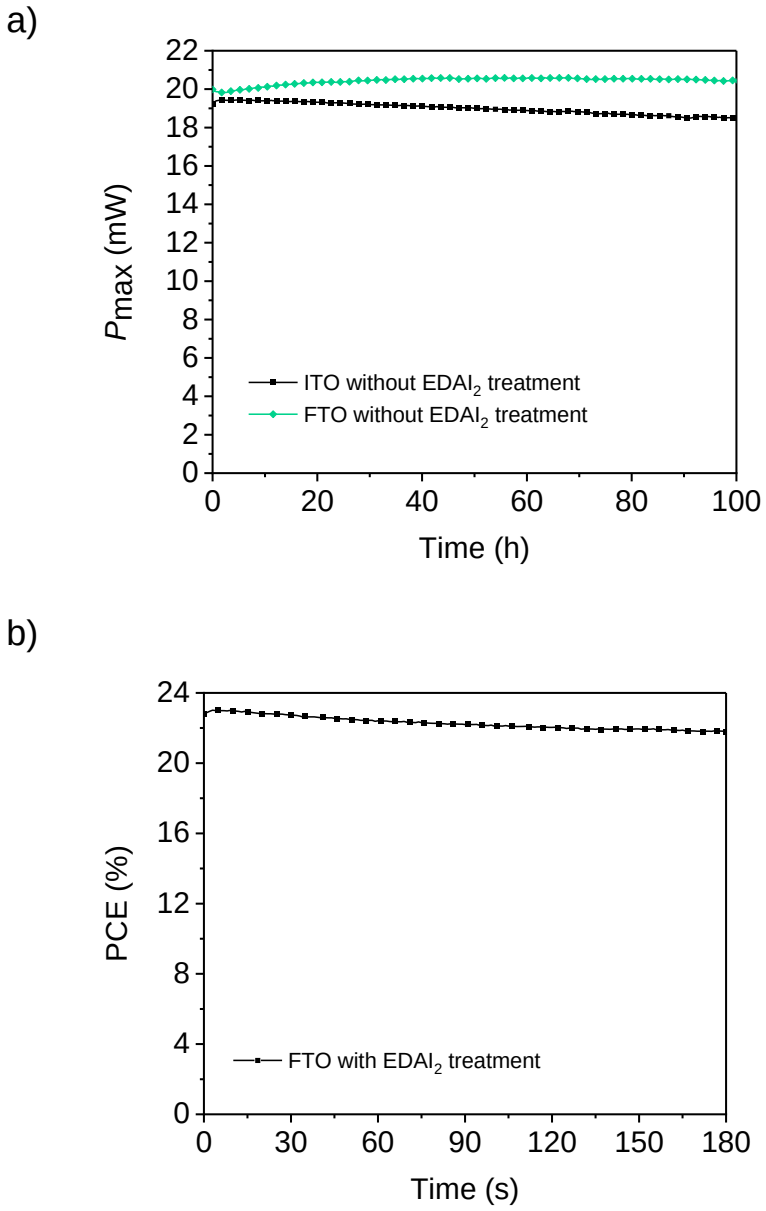

Figure S32. (a) Maximum power point tracking (MPPT) data measured under AM 1.5G in an inert atmosphere of PSCs fabricated on ITO/**3PATAT-C3** and FTO/**3PATAT-C3** substrates without $EDAI_2$ surface treatment, and (b) The stabilized power output under a fixed bias (0.975 V) of PSC using FTO/**3PATAT-C3** substrate with $EDAI_2$ surface treatment.

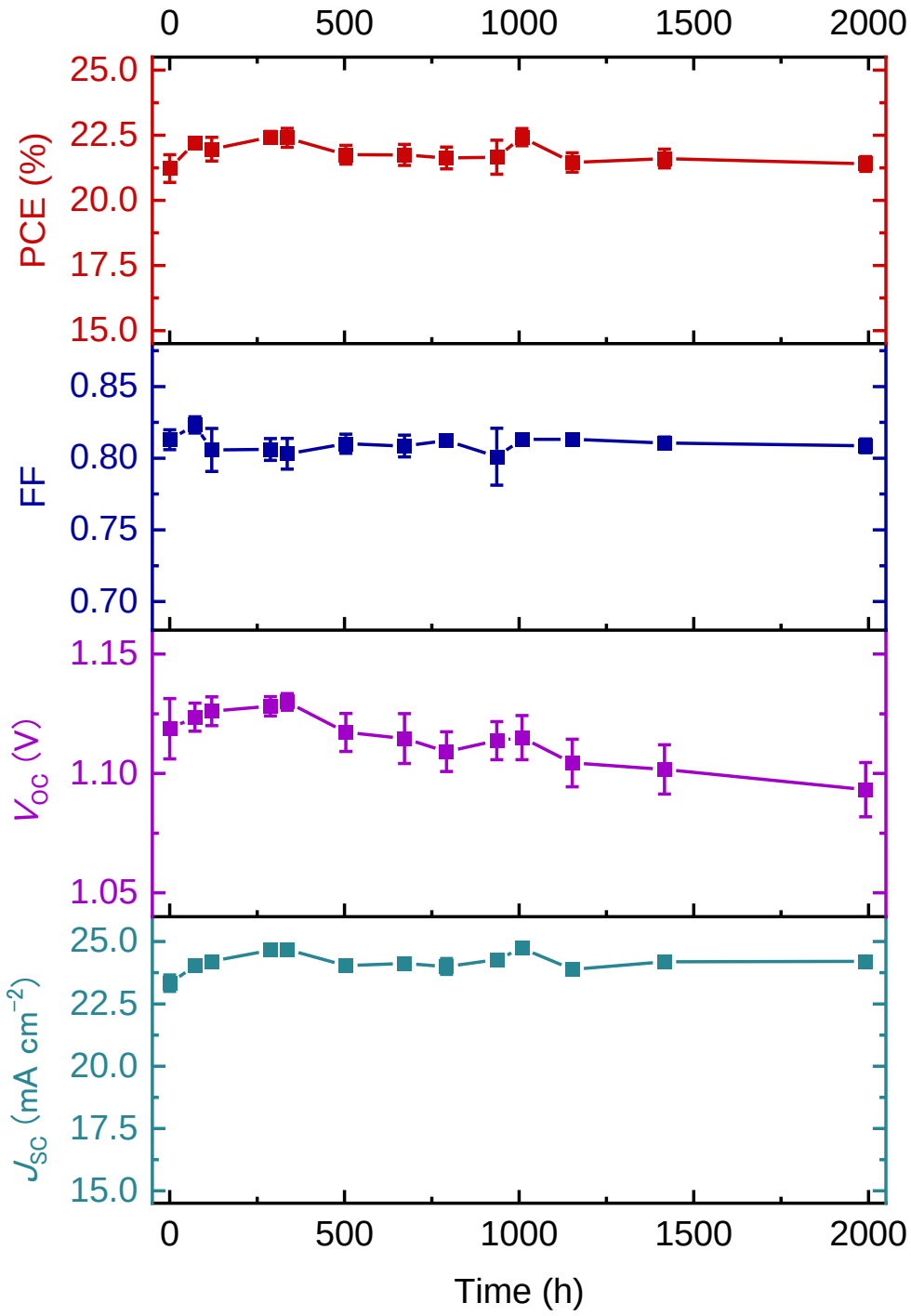

Figure S33. The shelf-stability test in the inert atmosphere under dark condition for the un-encapsulated devices fabricated with **3PATAT-C3** (9 devices, the error bars denote standard deviation).

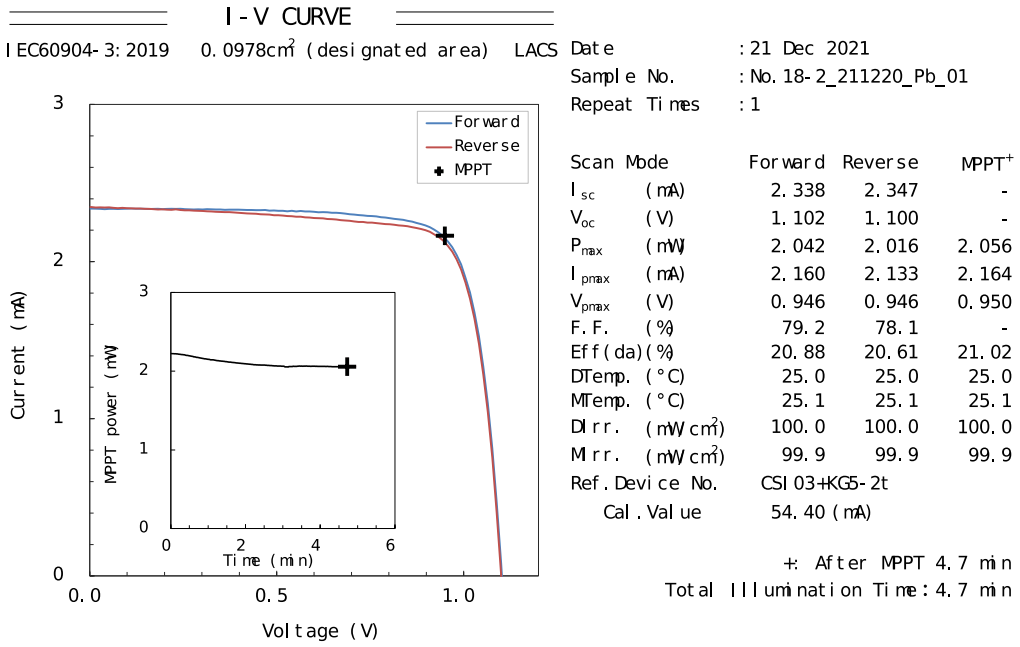

Figure S34. The certified results from National Institute of Advanced Industrial Science and Technology (AIST, Japan) of a representative **3PATAT-C3** cell.

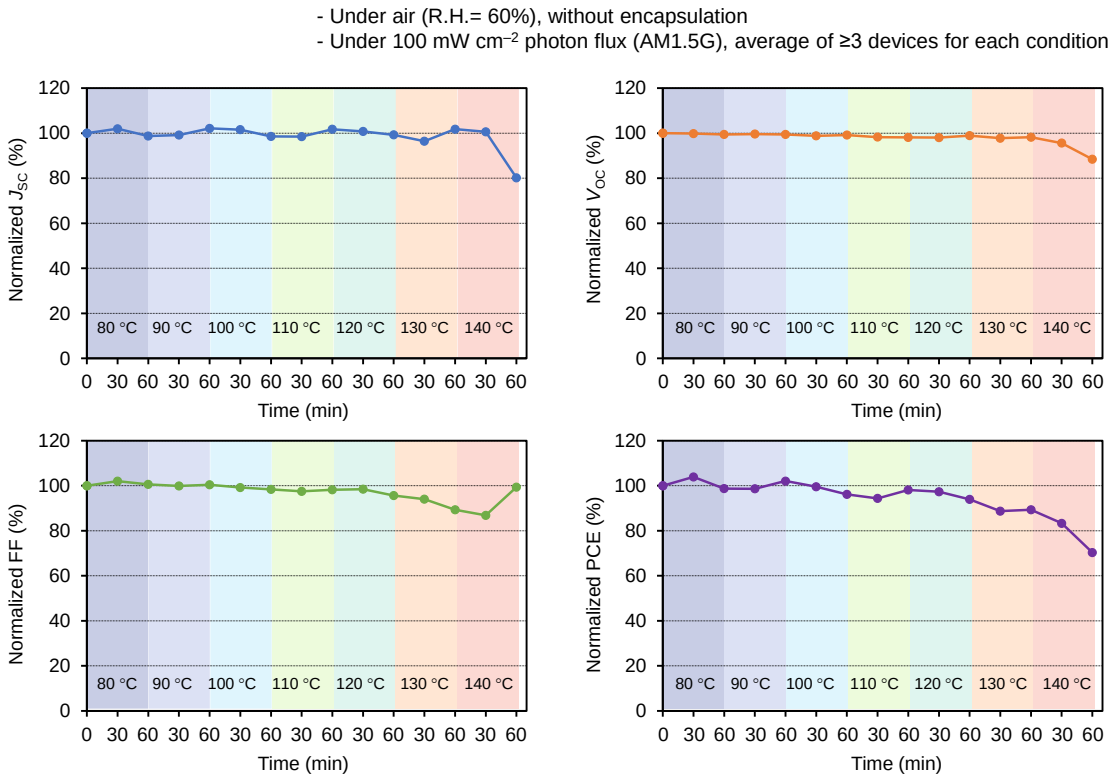

Figure S35. (a) J_{SC}, (b) V_{OC}, (c) FF, and (d) PCE evolution of the PSC devices under air (R.H.= 60%) without encapsulation, under 100 mW cm^{-2} photon flux (AM 1.5G).

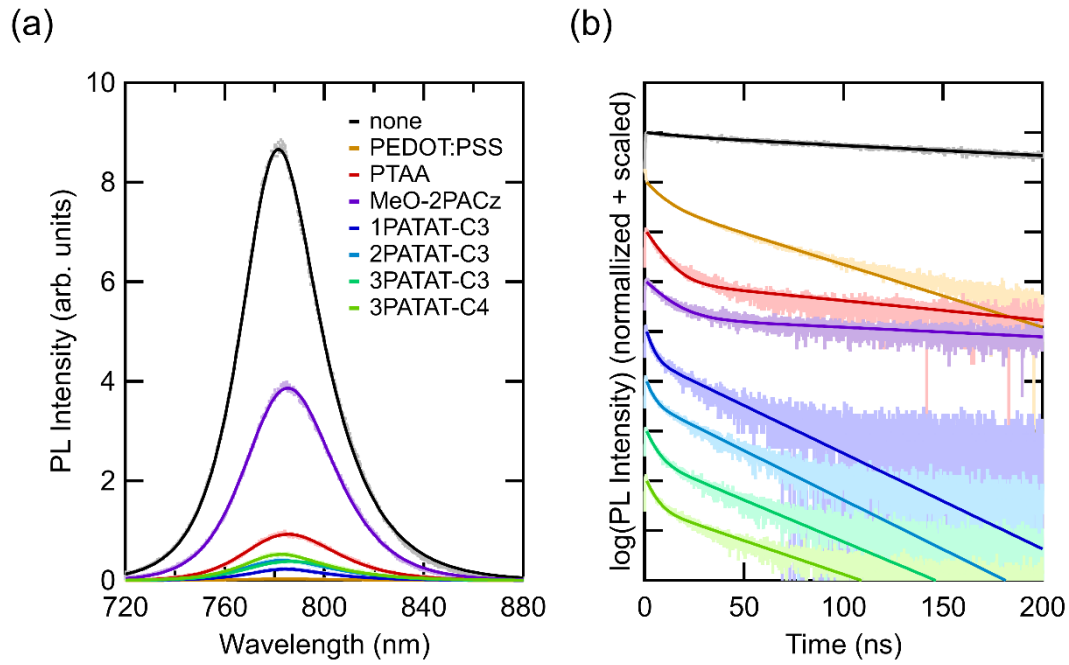

HCM	PL intensity	Life time
none	100%	189 ns
MeO-2PACz	45%	51 ns
PTAA	11%	17 ns
3PATAT-C4	6.1%	12 ns
2PATAT-C3	4.6%	10 ns
3PATAT-C3	4.4%	10 ns
1PATAT-C3	2.6%	8 ns
PEDOT:PSS	0.4%	18 ns

Figure S36. (a) Steady-state PL and (b) time-resolved PL spectra of the perovskite films ($Cs_{0.05}FA_{0.80}MA_{0.15}PbI_{2.75}Br_{0.25}$) fabricated on ITO and ITO/HCM substrates excited at 688 nm with an excitation fluence of 100 nJ cm^{-2}.

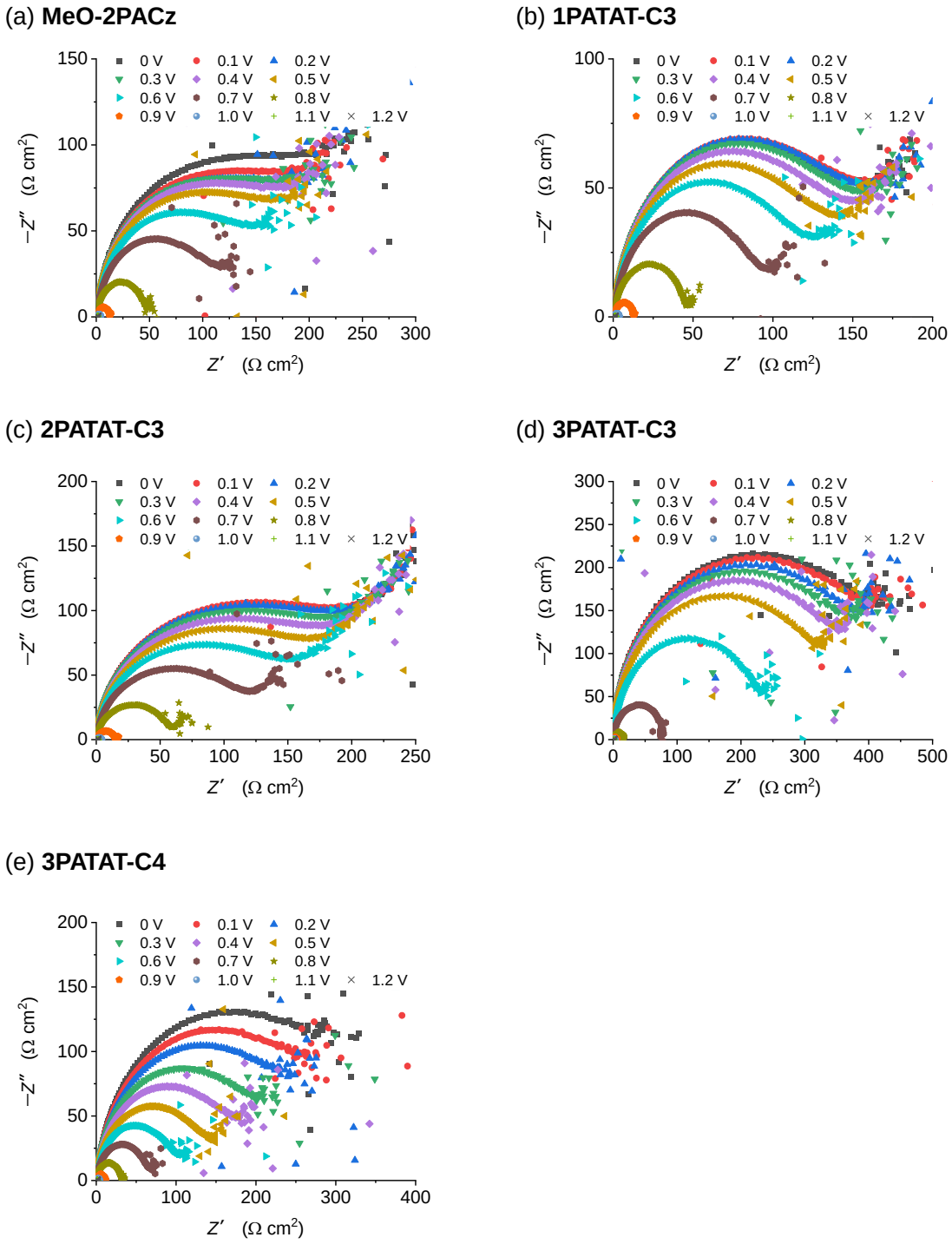

Figure S37. Complex impedance plots under an inert atmosphere at AM 1.5G illumination and varied applied bias.

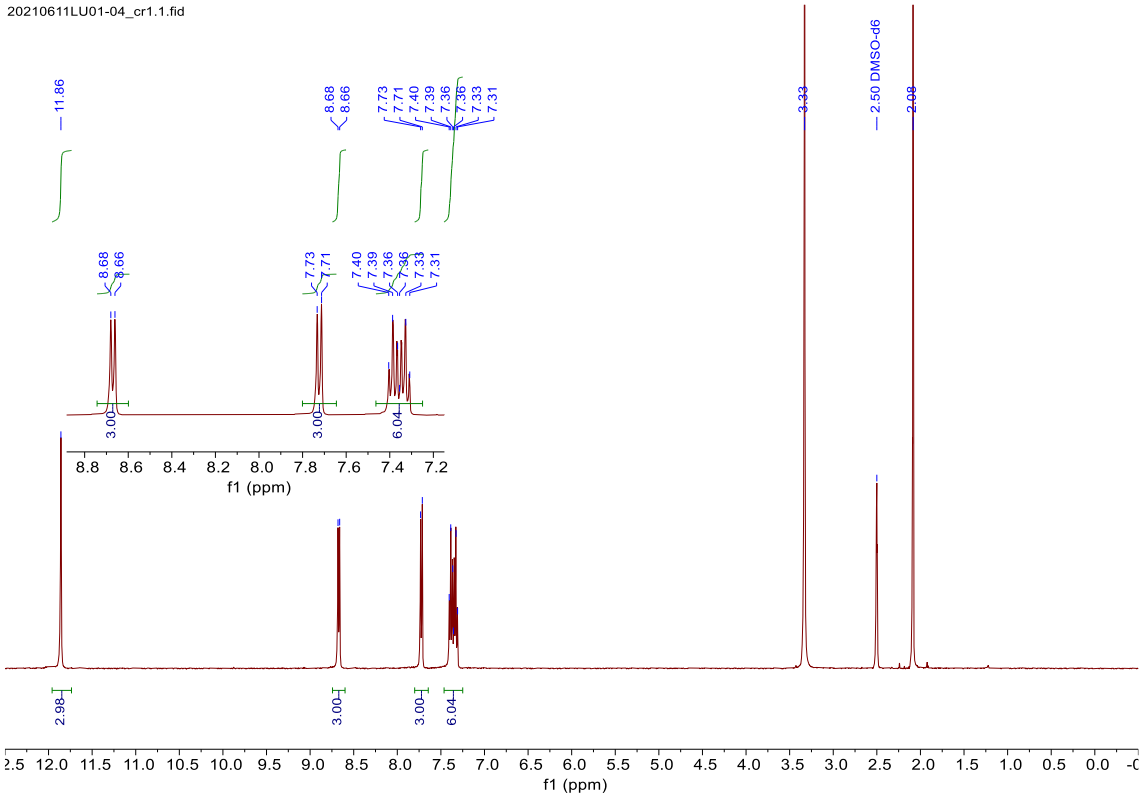

Figure S38. ^{1}H NMR spectrum of **TAT** in DMSO-d_6.

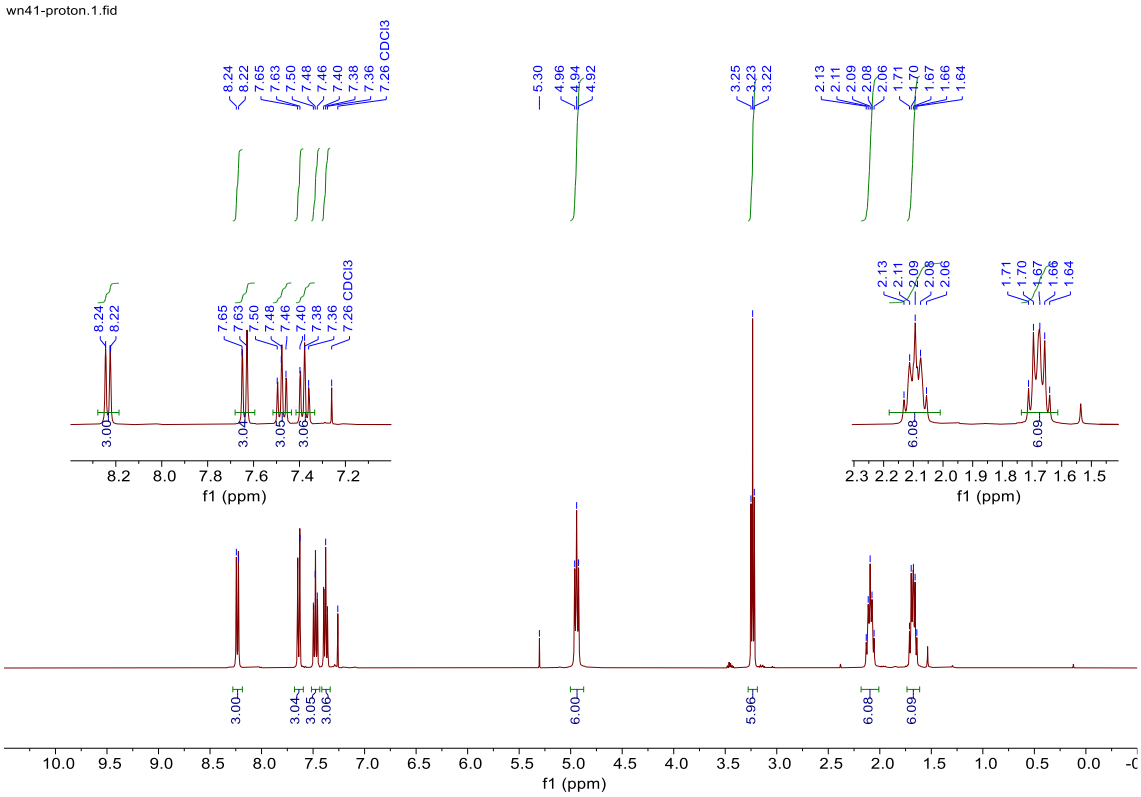

Figure S39. ^{1}H NMR spectrum of **3TAT-C4Br** in $CDCl_3$.

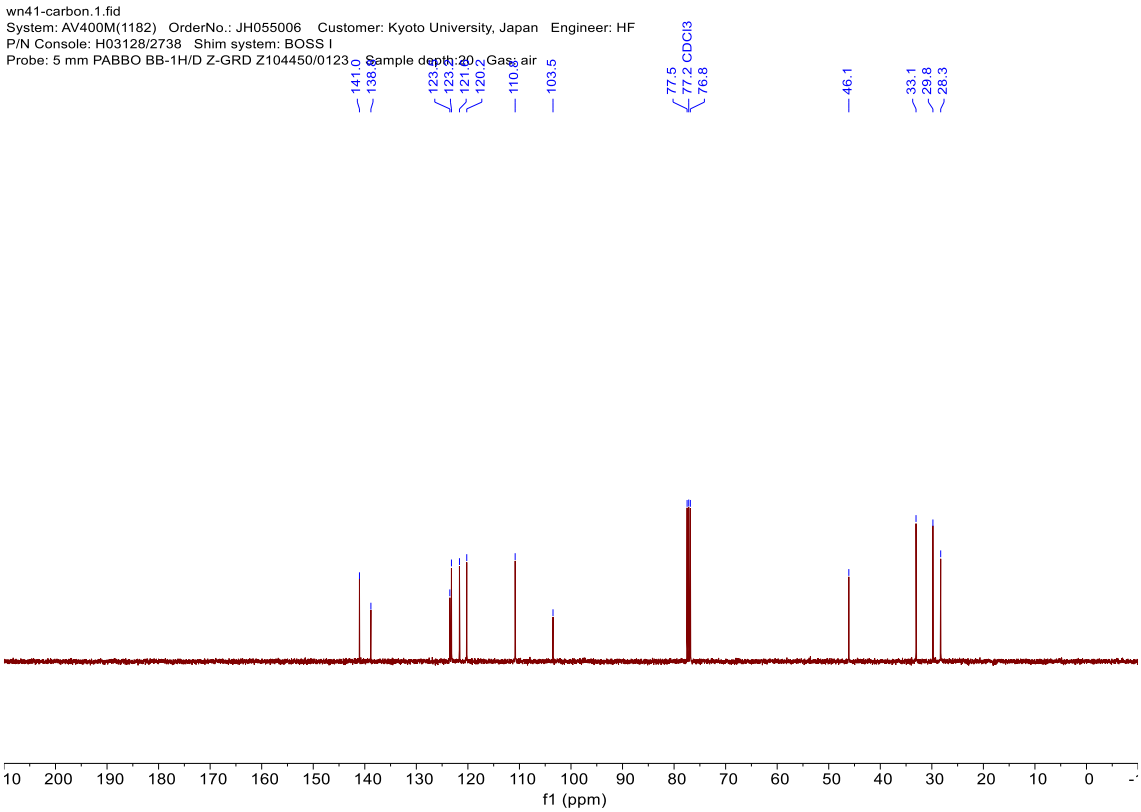

Figure S40. ^{13}C NMR spectrum of **3TAT-C4Br** in $CDCl_3$.

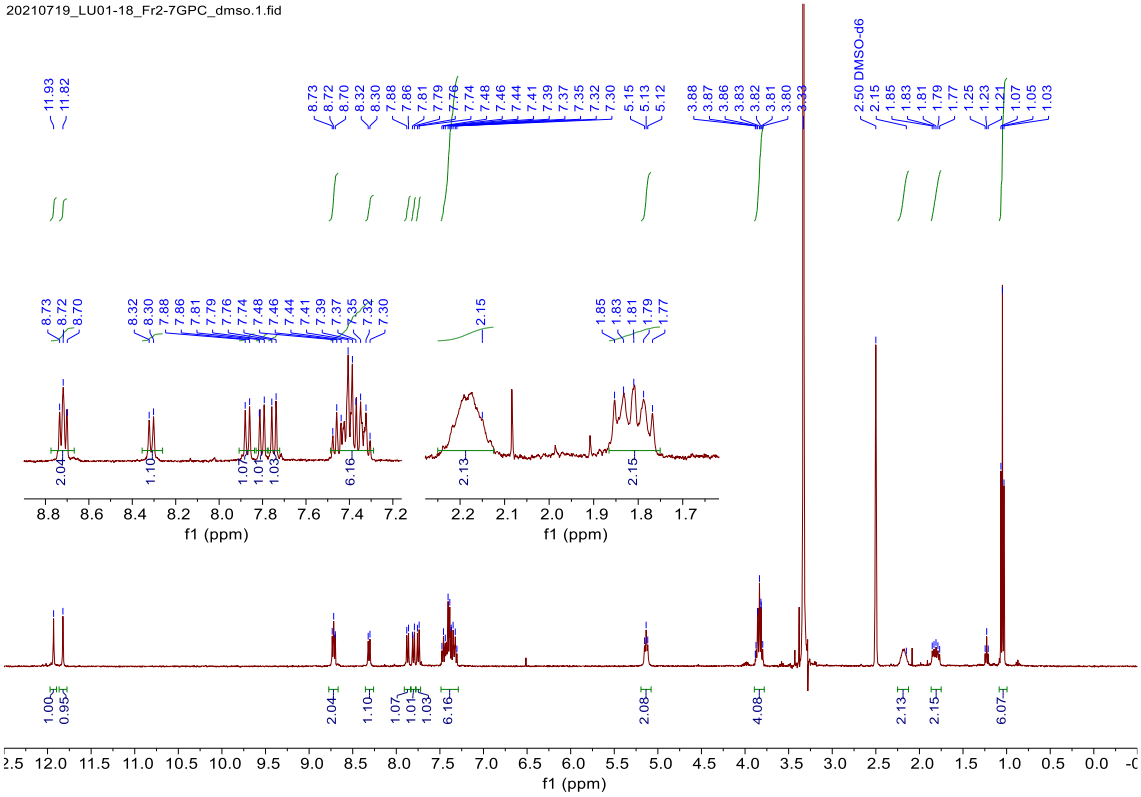

Figure S41. ^{1}H NMR spectrum of **1** in DMSO-d_6.

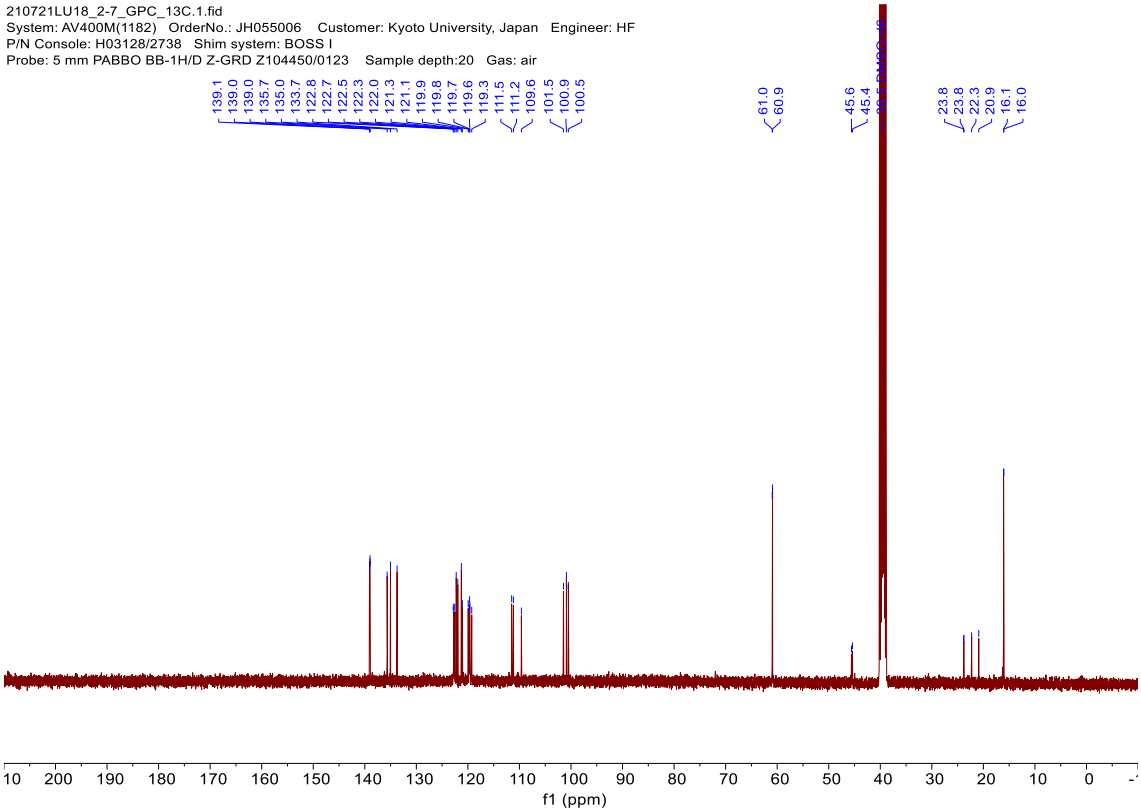

Figure S42. ^{13}C NMR spectrum of **1** in DMSO-d_6.

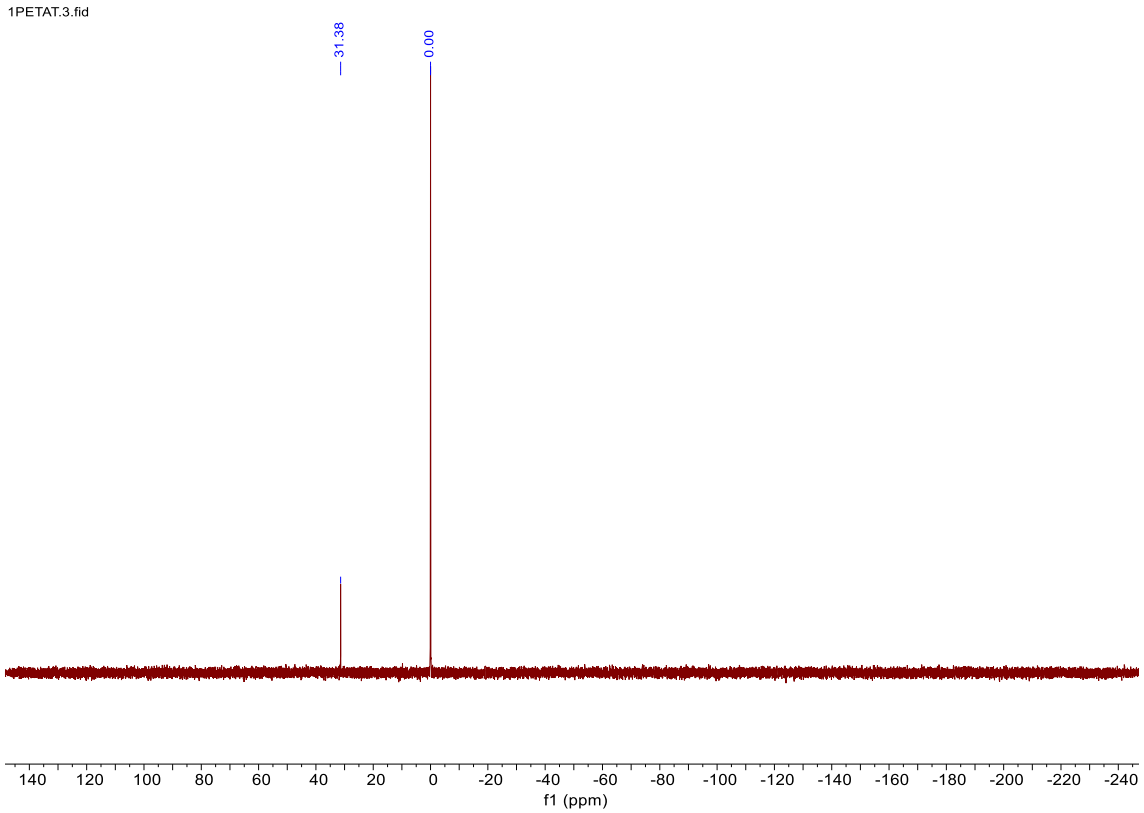

Figure S43. ^{31}P NMR spectrum of **1** in DMSO-d_6.

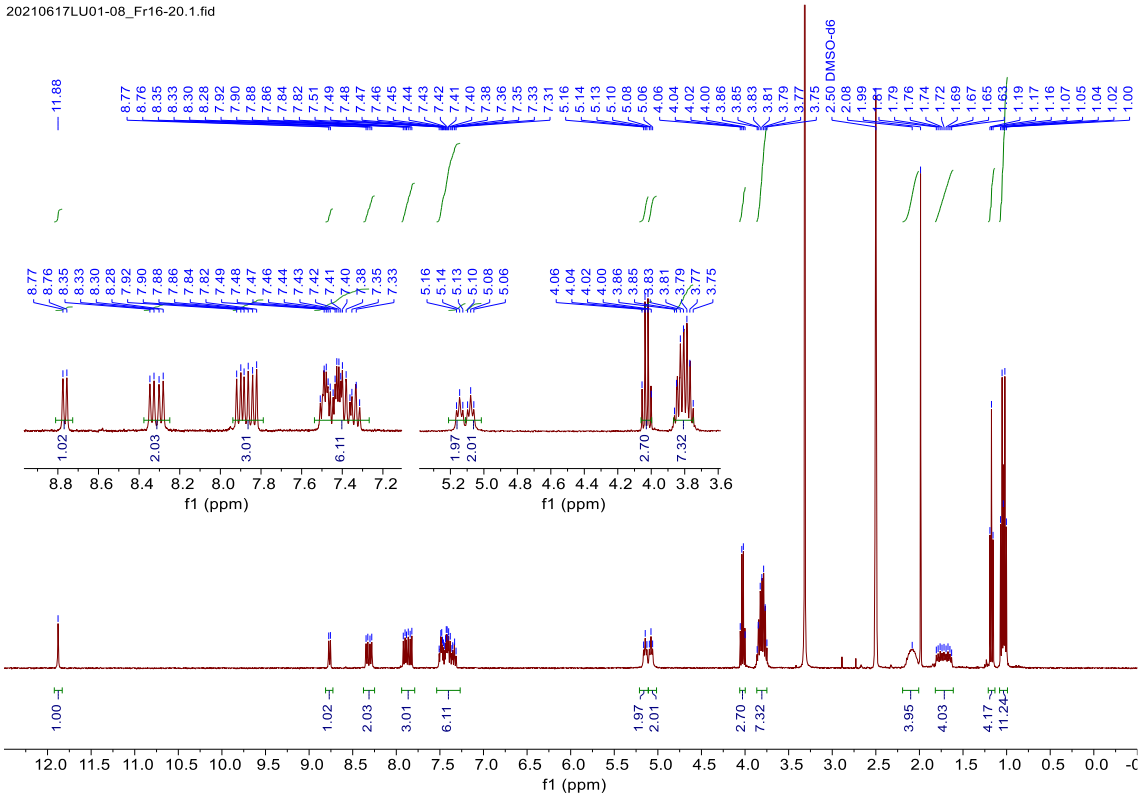

Figure S44. ^{1}H NMR spectrum of **2** in DMSO-d_6.

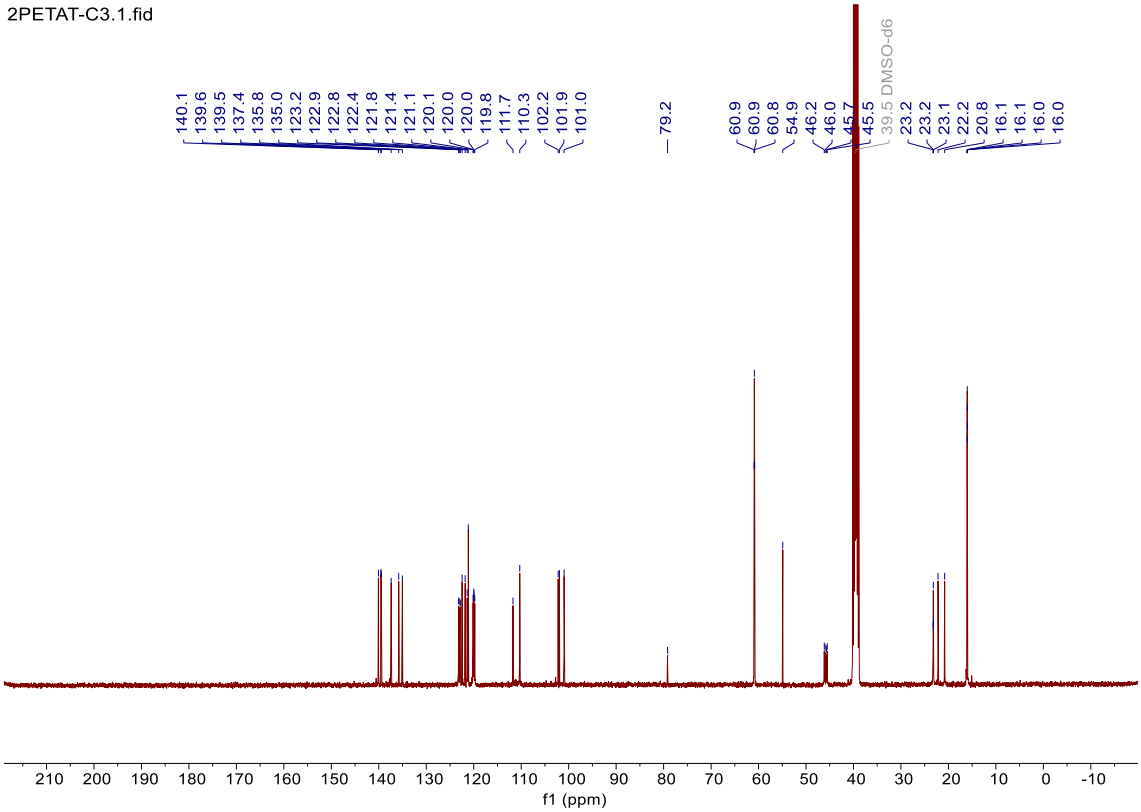

Figure S45. ^{13}C NMR spectrum of **2** in DMSO-d_6.

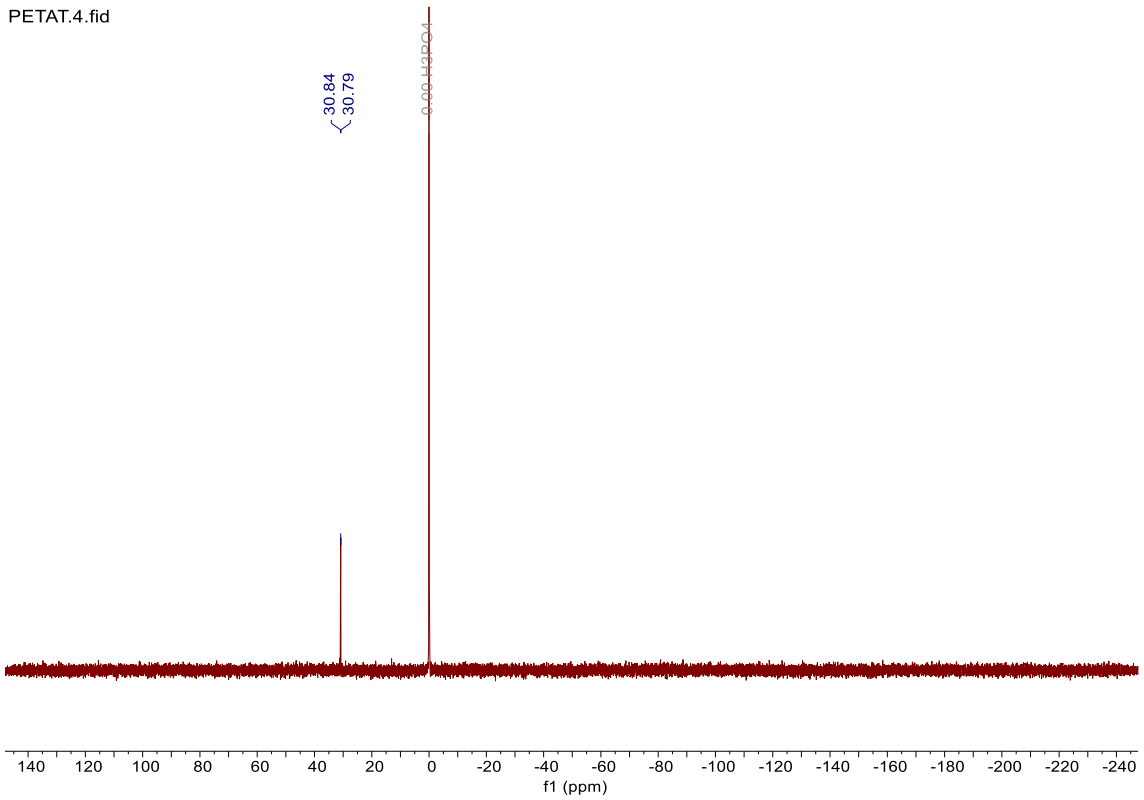

Figure S46. ^{31}P NMR spectrum of **2** in DMSO-d_6.

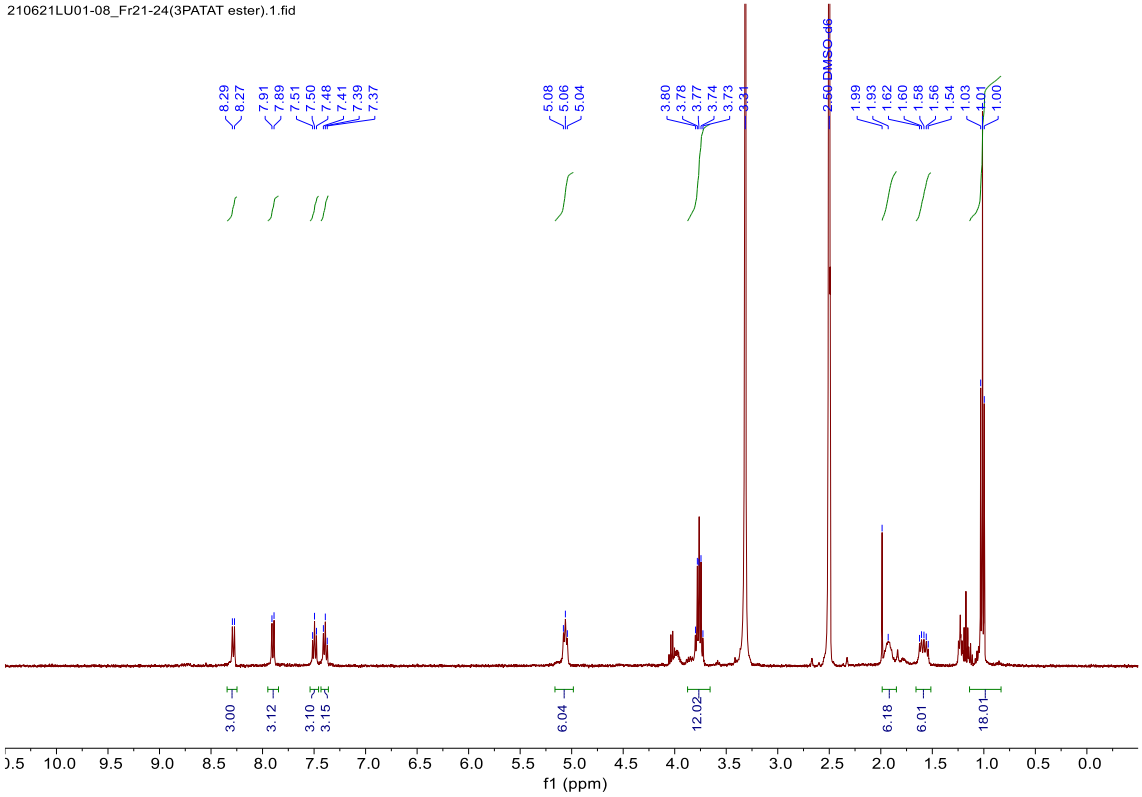

Figure S47. ^{1}H NMR spectrum of **3** in DMSO-d_6.

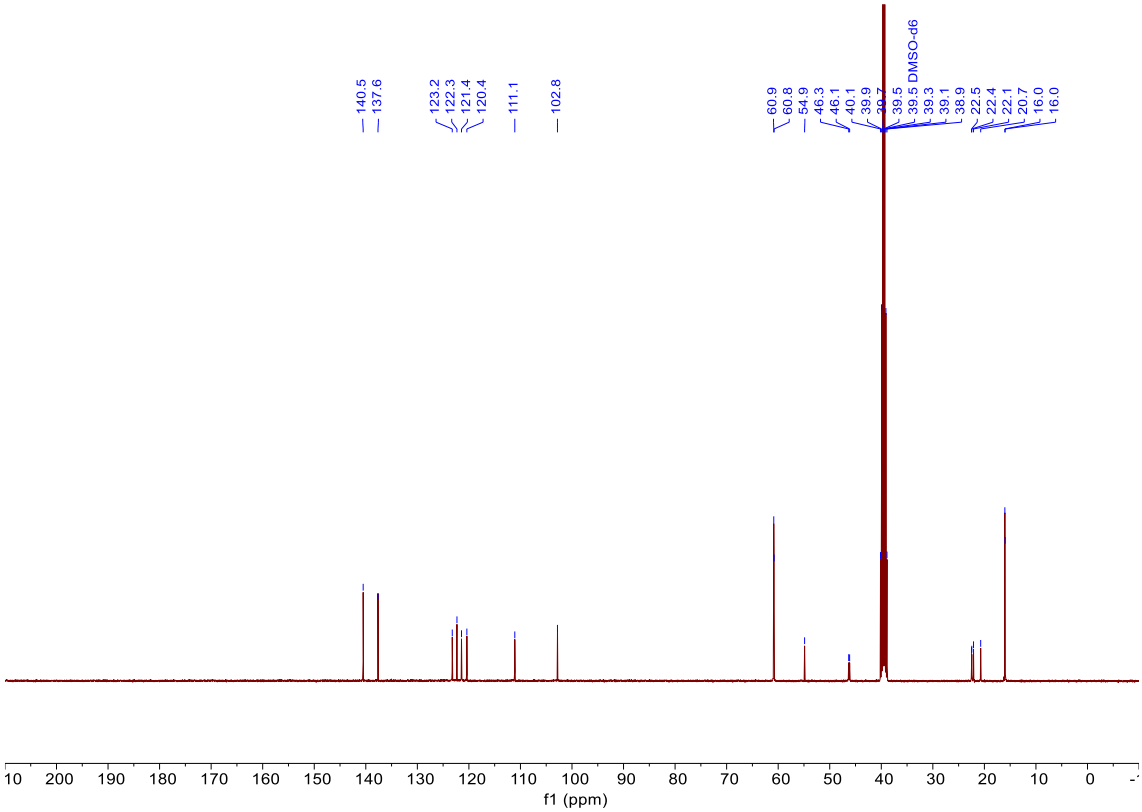

Figure S48. ^{13}C NMR spectrum of **3** in DMSO-d_6.

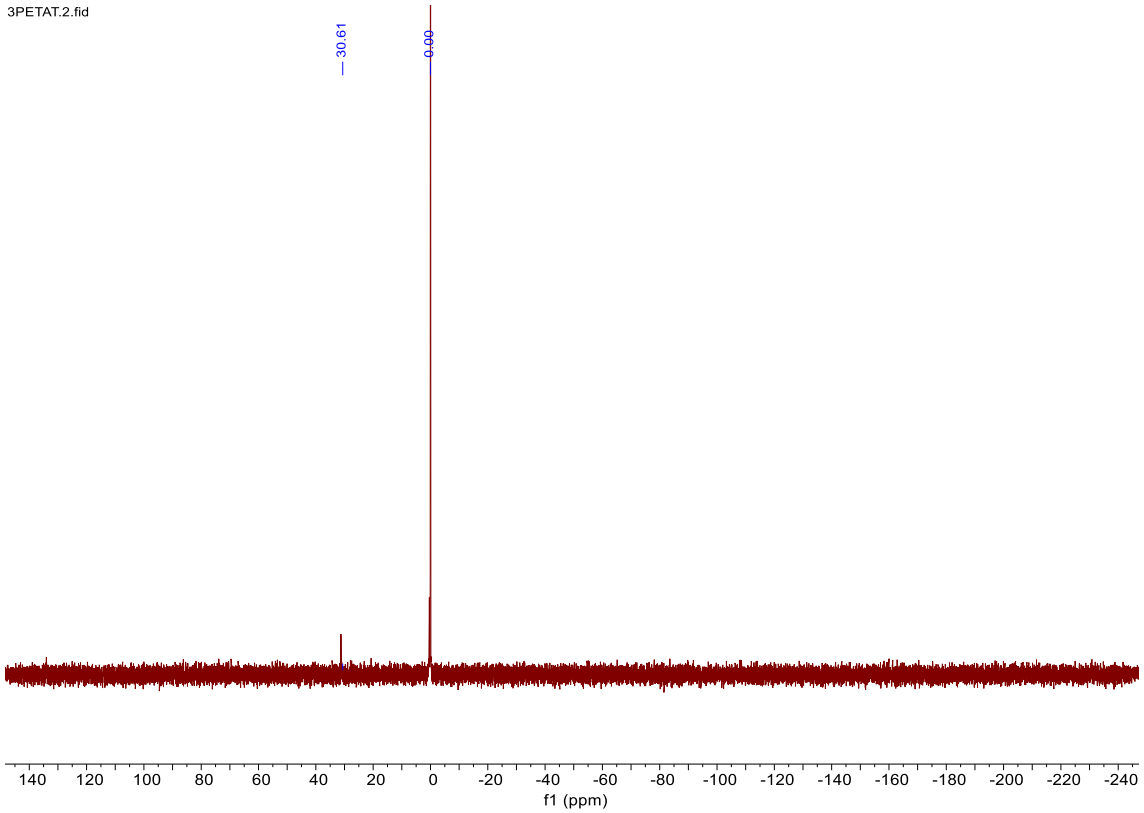

Figure S49. ^{31}P NMR spectrum of **3** in DMSO-d_6.

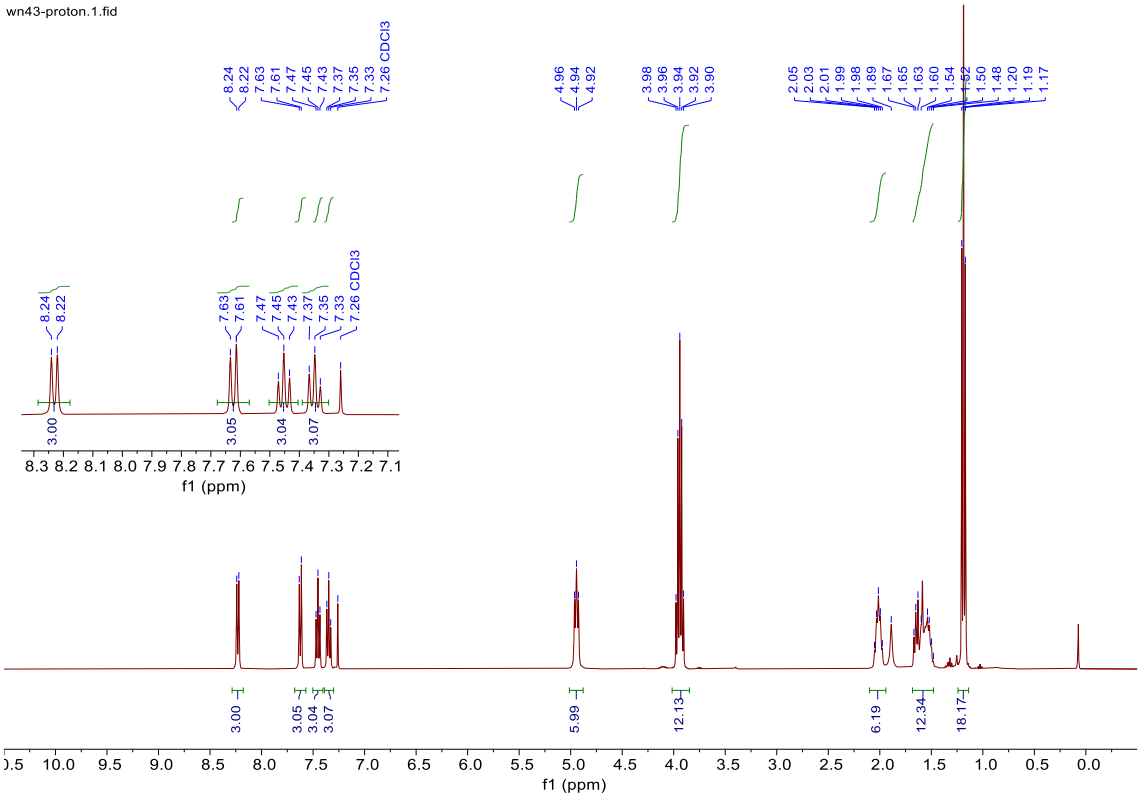

Figure S50. ^{1}H NMR spectrum of **4** in $CDCl_3$.

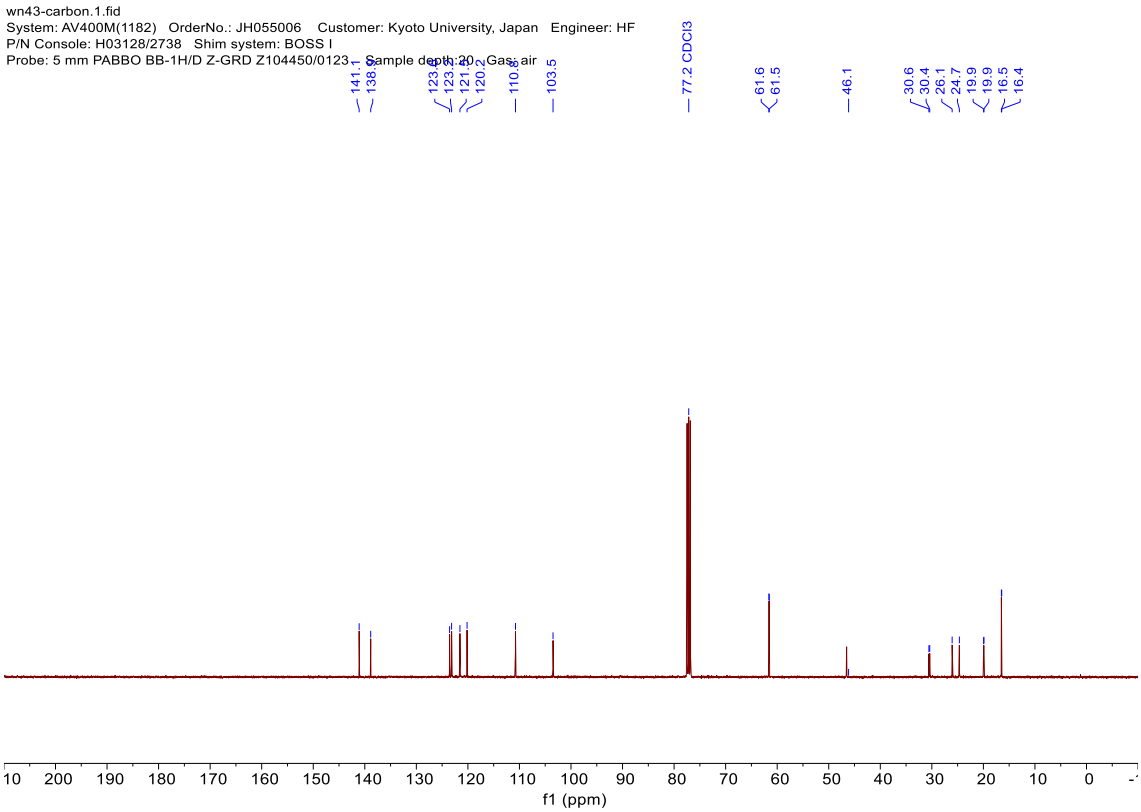

Figure S51. ^{13}C NMR spectrum of **4** in $CDCl_3$.

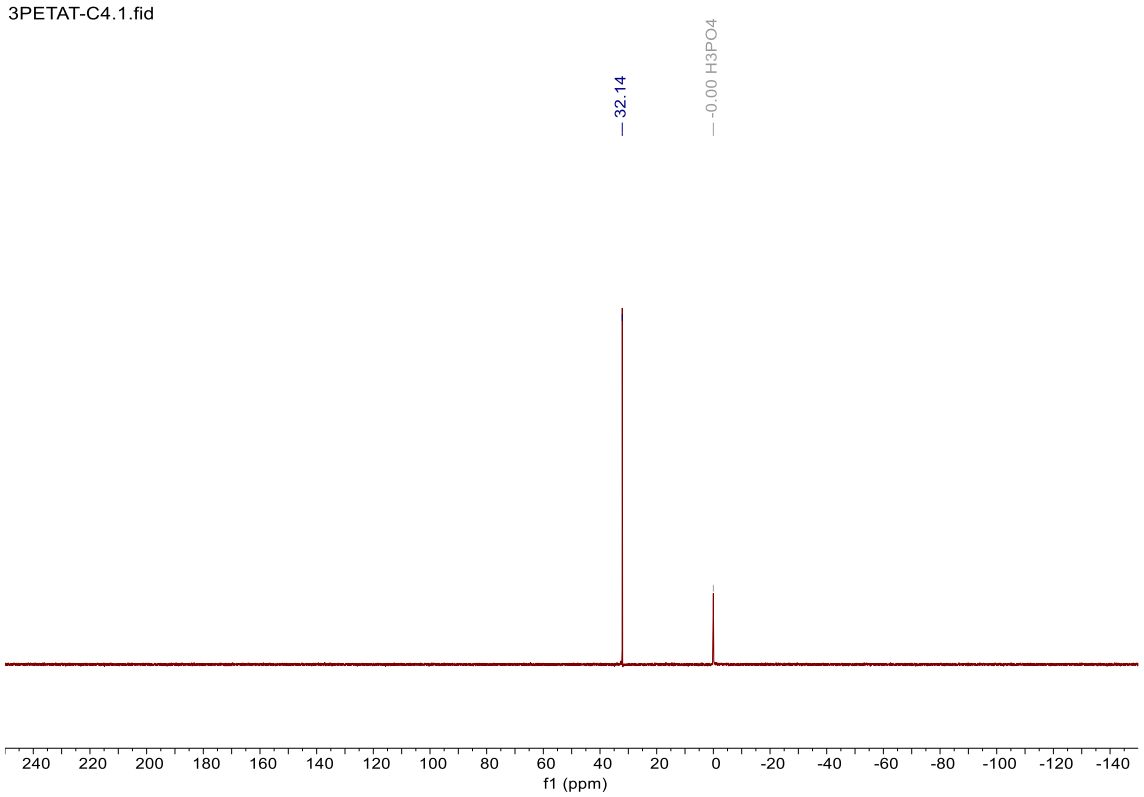

Figure S52. ^{31}P NMR spectrum of **4** in DMSO-d_6.

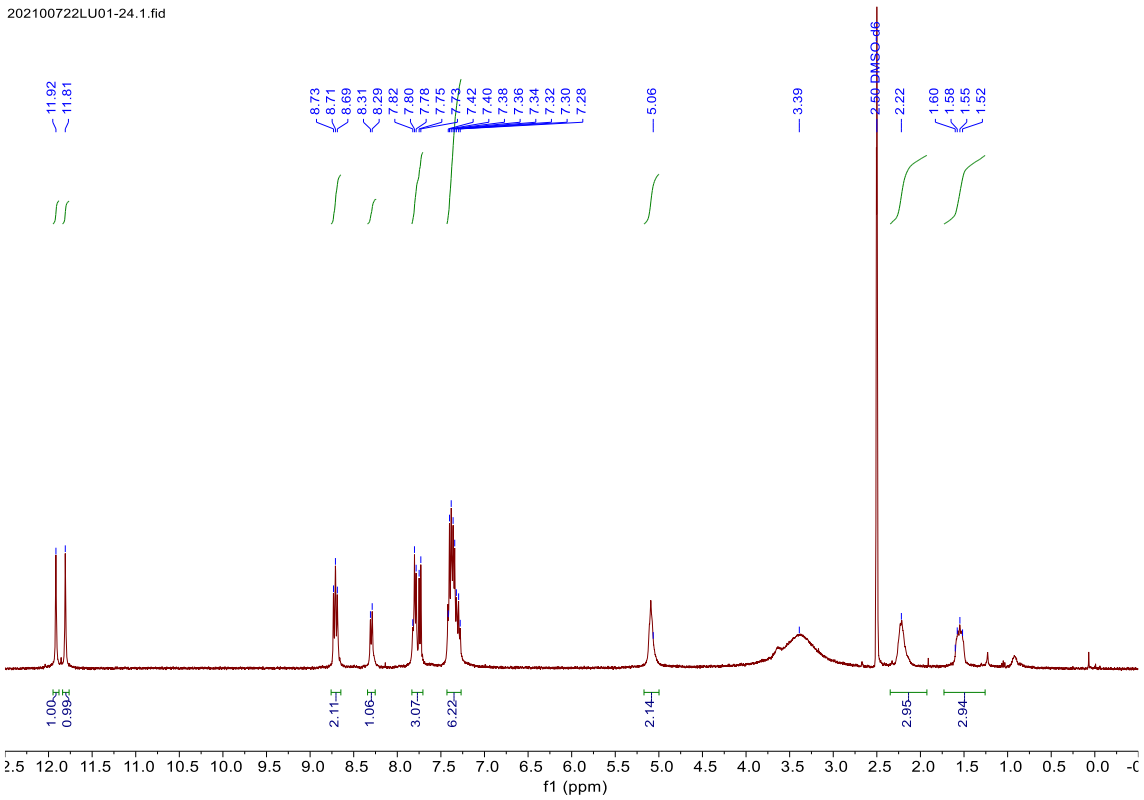

Figure S53. ^{1}H NMR spectrum of **1PATAT-C3** in DMSO-d_6.

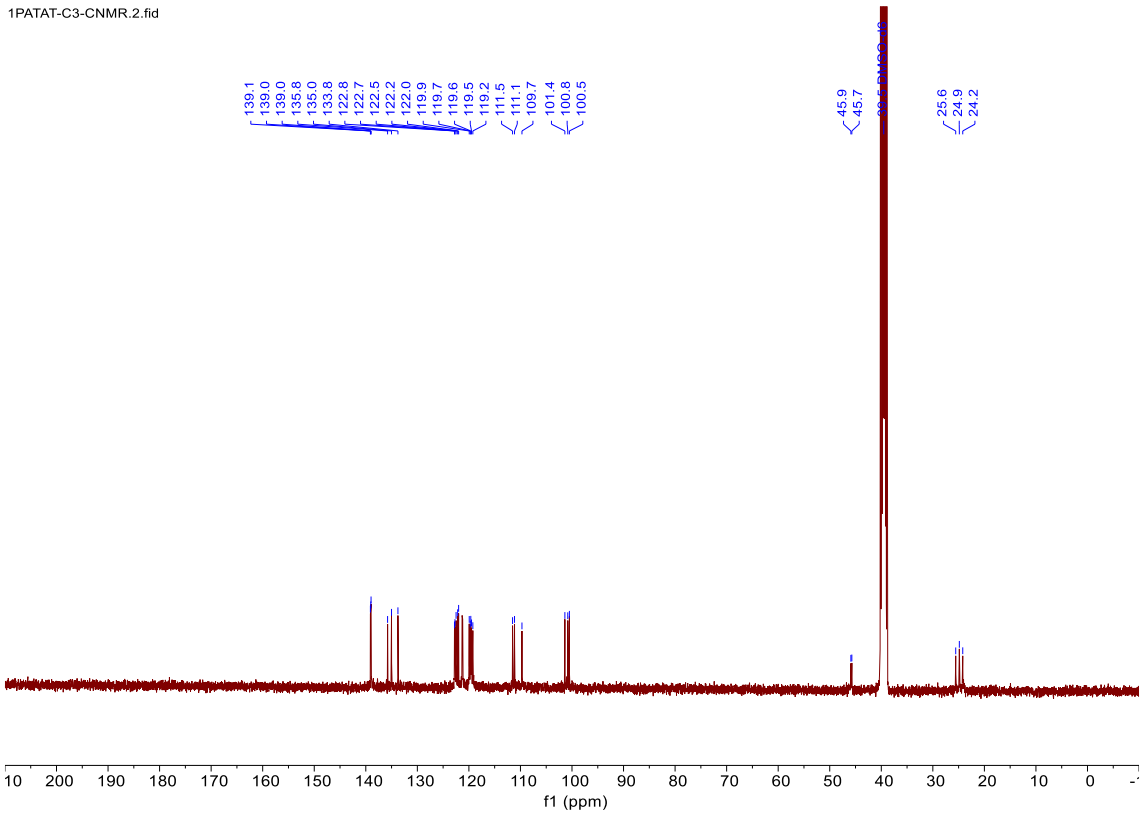

Figure S54. ^{13}C NMR spectrum of **1PATAT-C3** in DMSO-d_6.

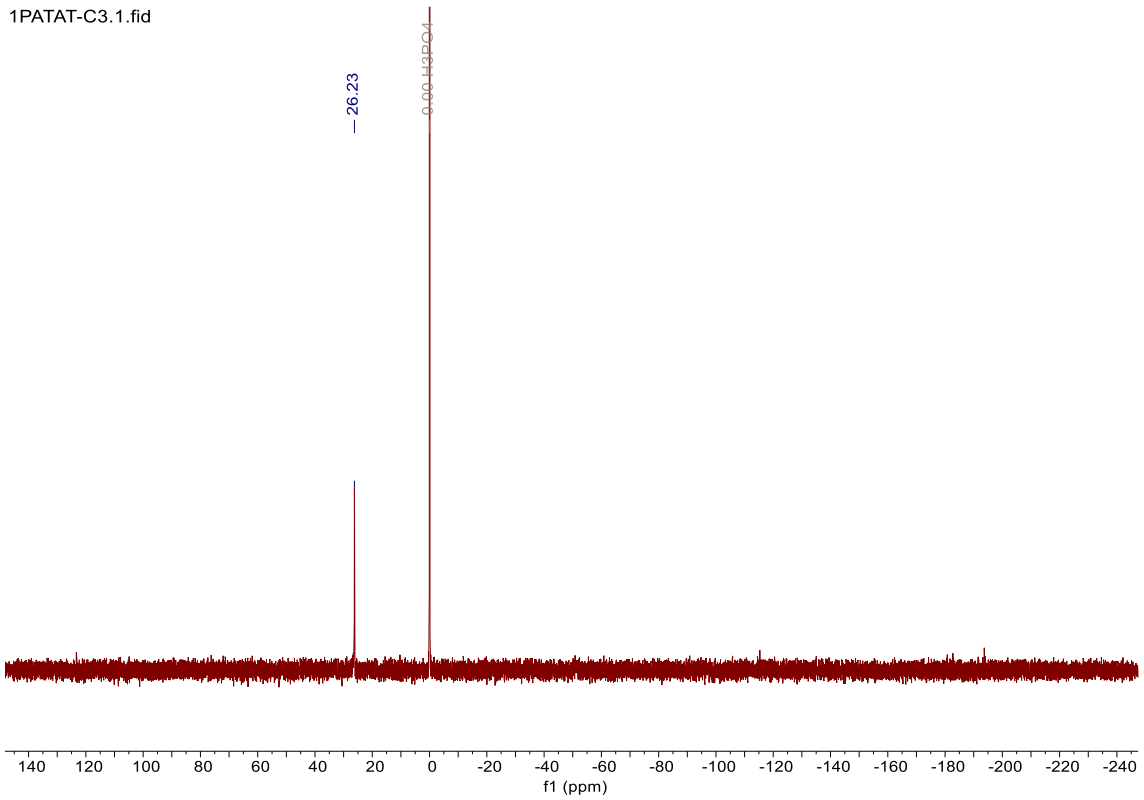

Figure S55. ^{31}P NMR spectrum of **1PATAT-C3** in DMSO-d_6.

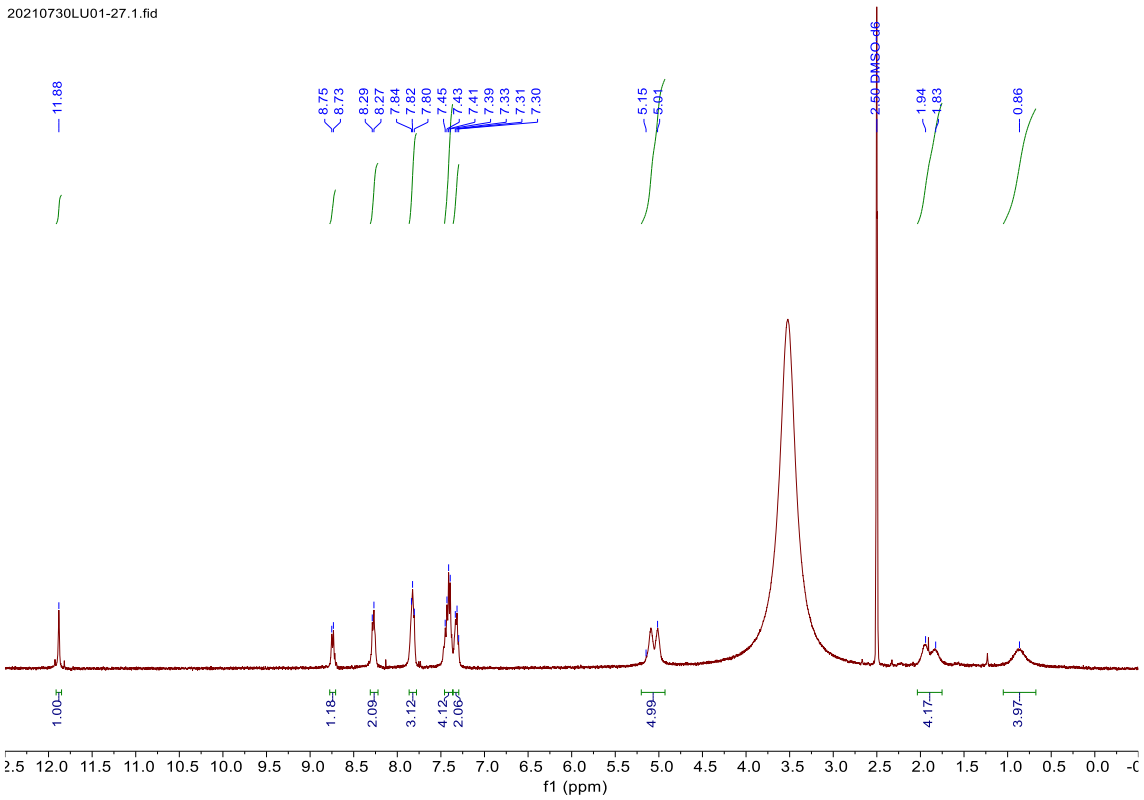

Figure S56. ^{1}H NMR spectrum of **2PATAT-C3** in DMSO-d_6.

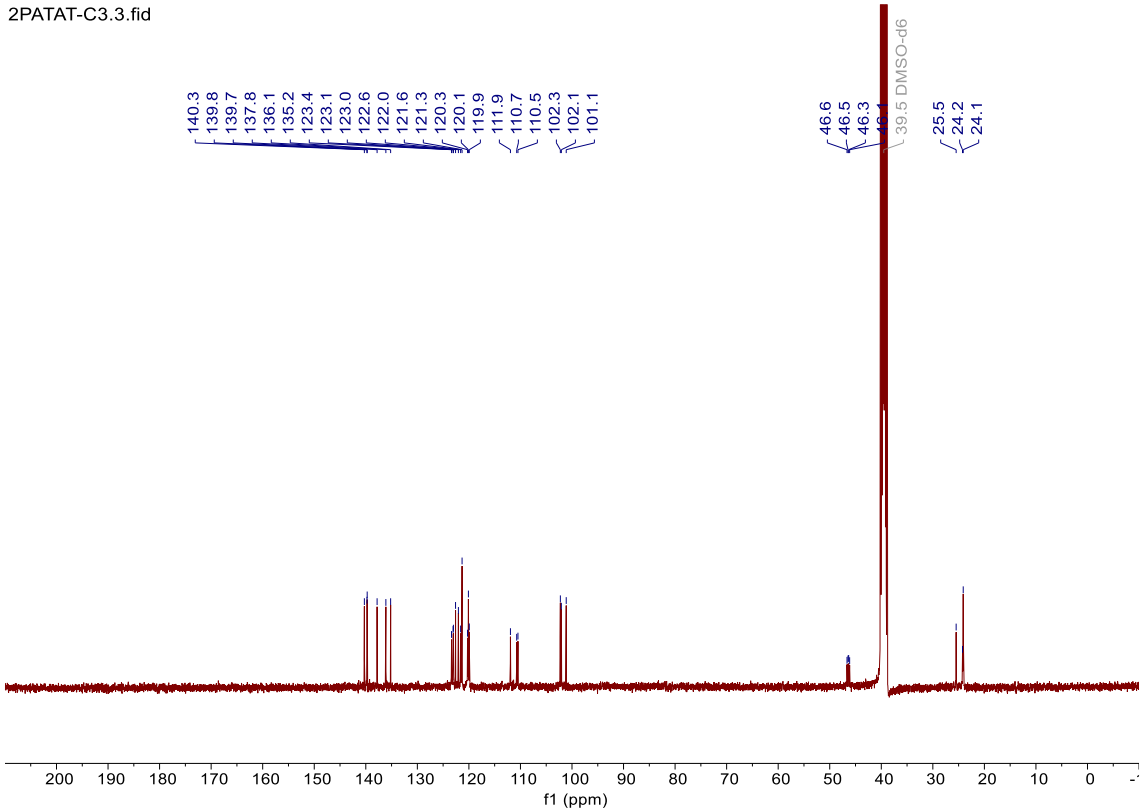

Figure S57. ^{13}C NMR spectrum of **2PATAT-C3** in DMSO-d_6.

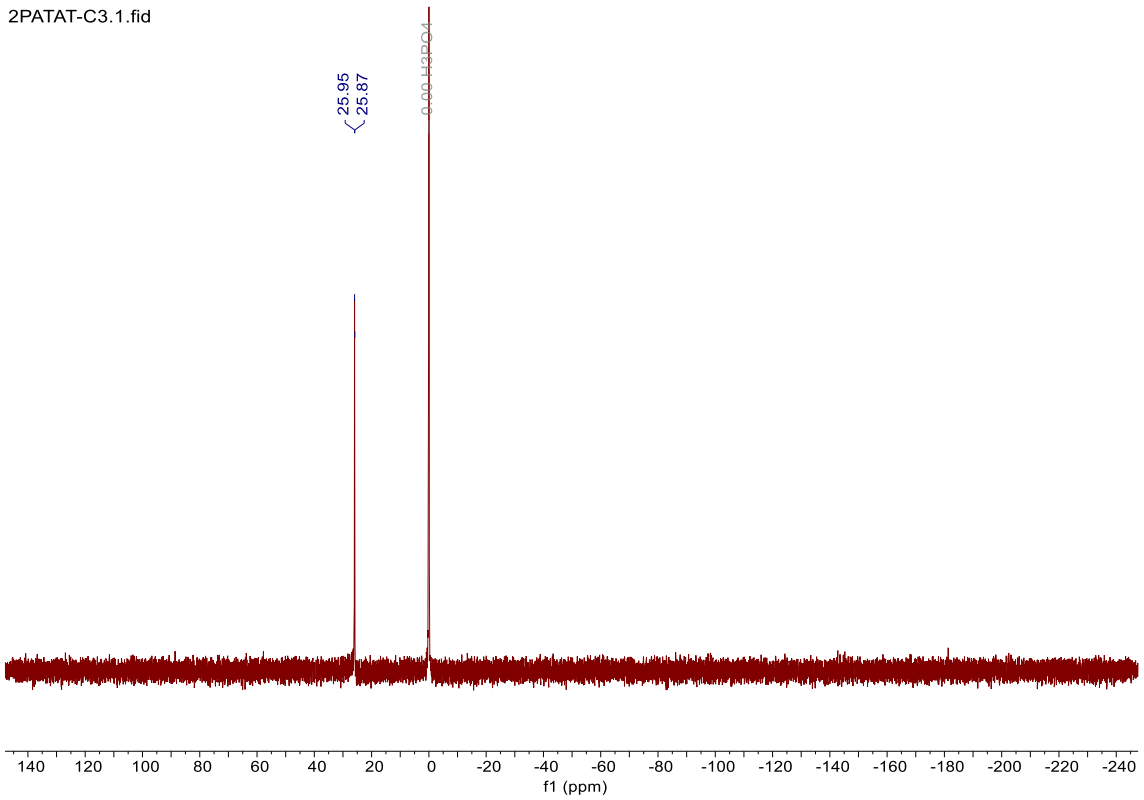

Figure S58. ^{31}P NMR spectrum of **2PATAT-C3** in DMSO-d_6.

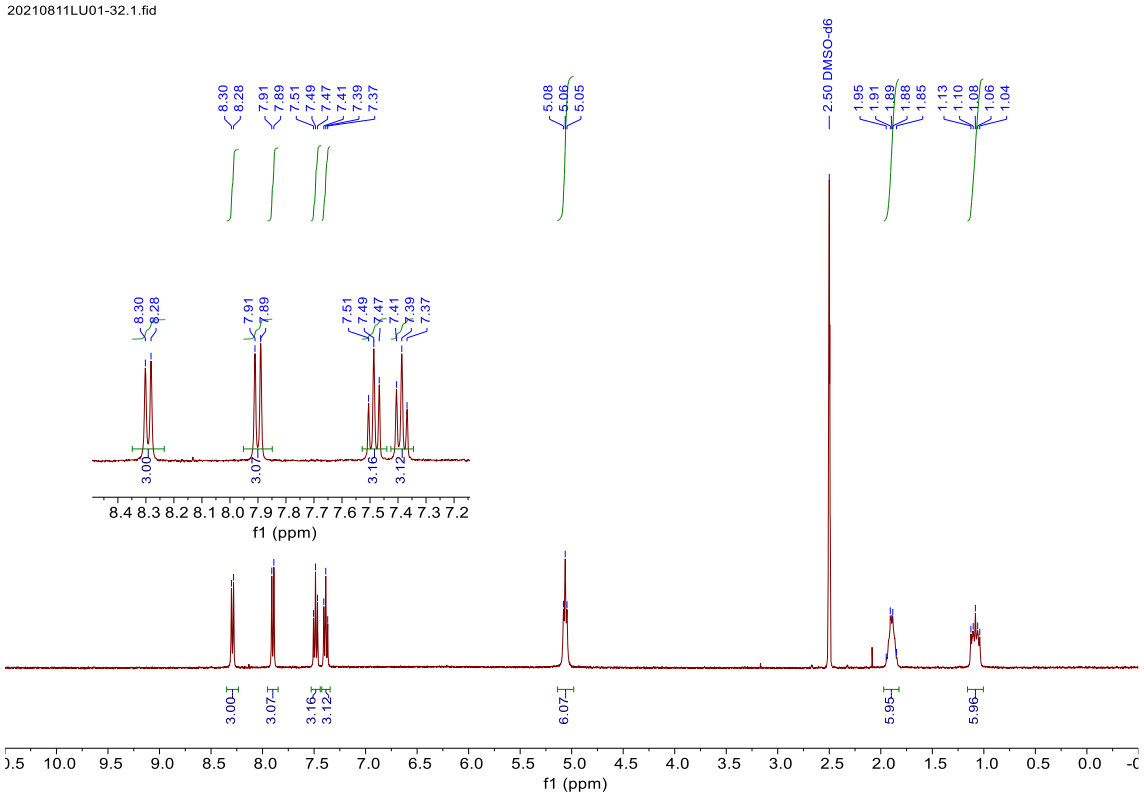

Figure S59. ^{1}H NMR spectrum of **3PATAT-C3** in DMSO-d_6.

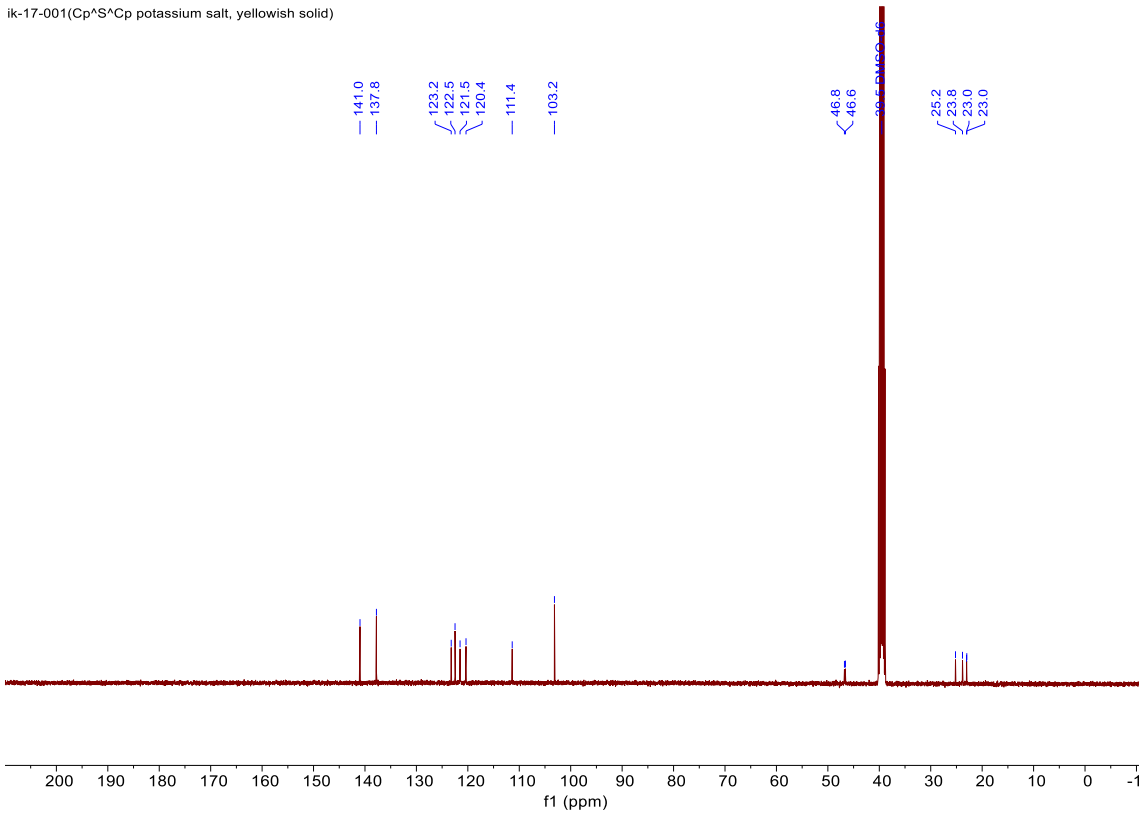

Figure S60. ^{13}C NMR spectrum of **3PATAT-C3** in DMSO-d_6.

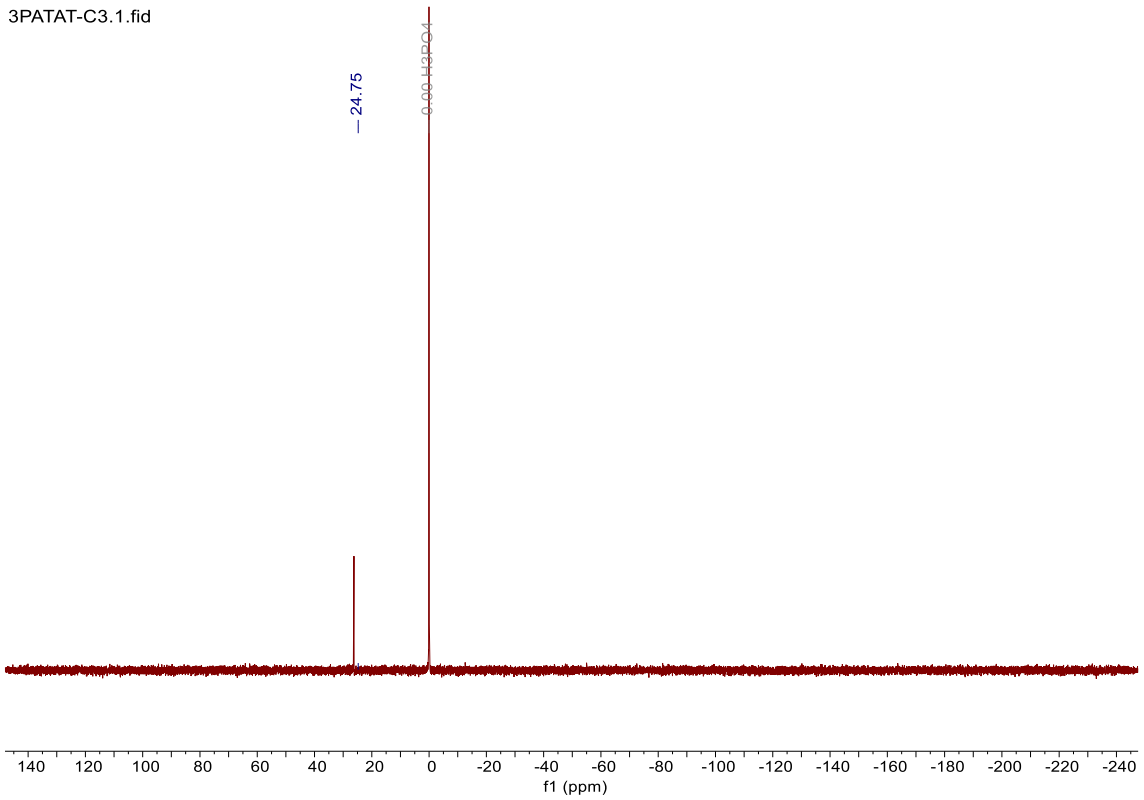

Figure S61. ^{31}P NMR spectrum of **3PATAT-C3** in DMSO-d_6.

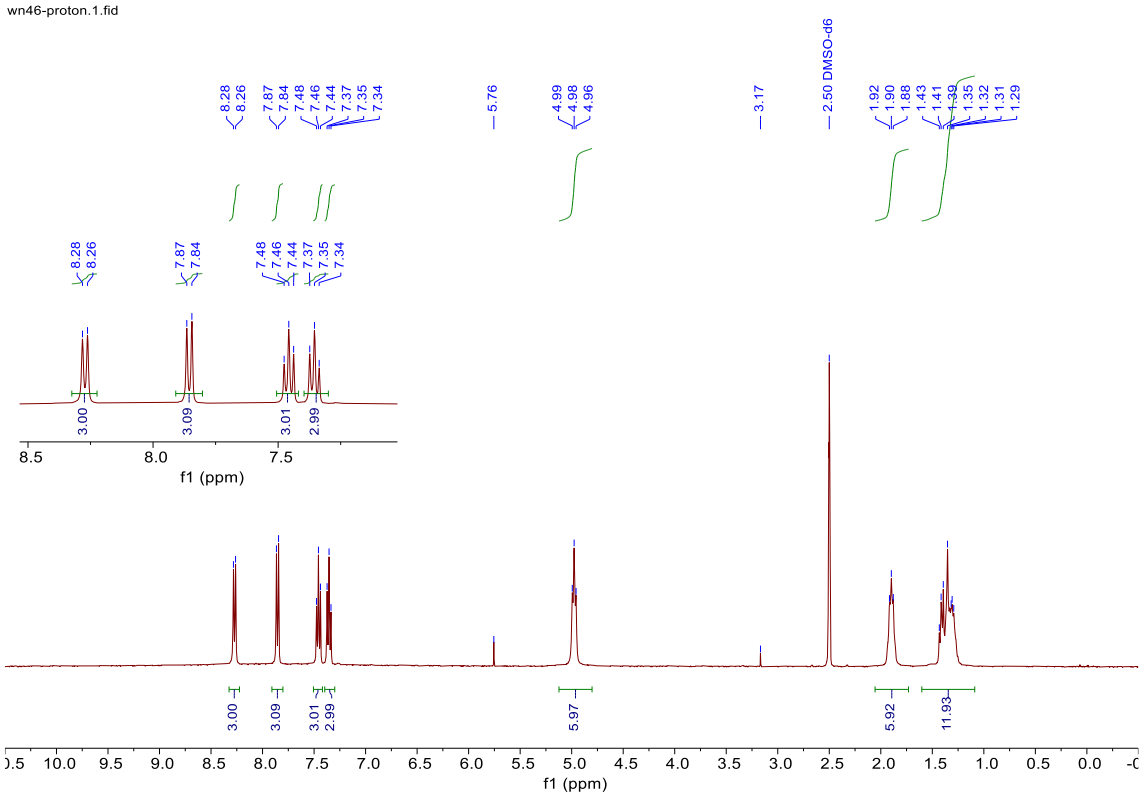

Figure S62. ^{1}H NMR spectrum of **3PATAT-C4** in DMSO-d_6.

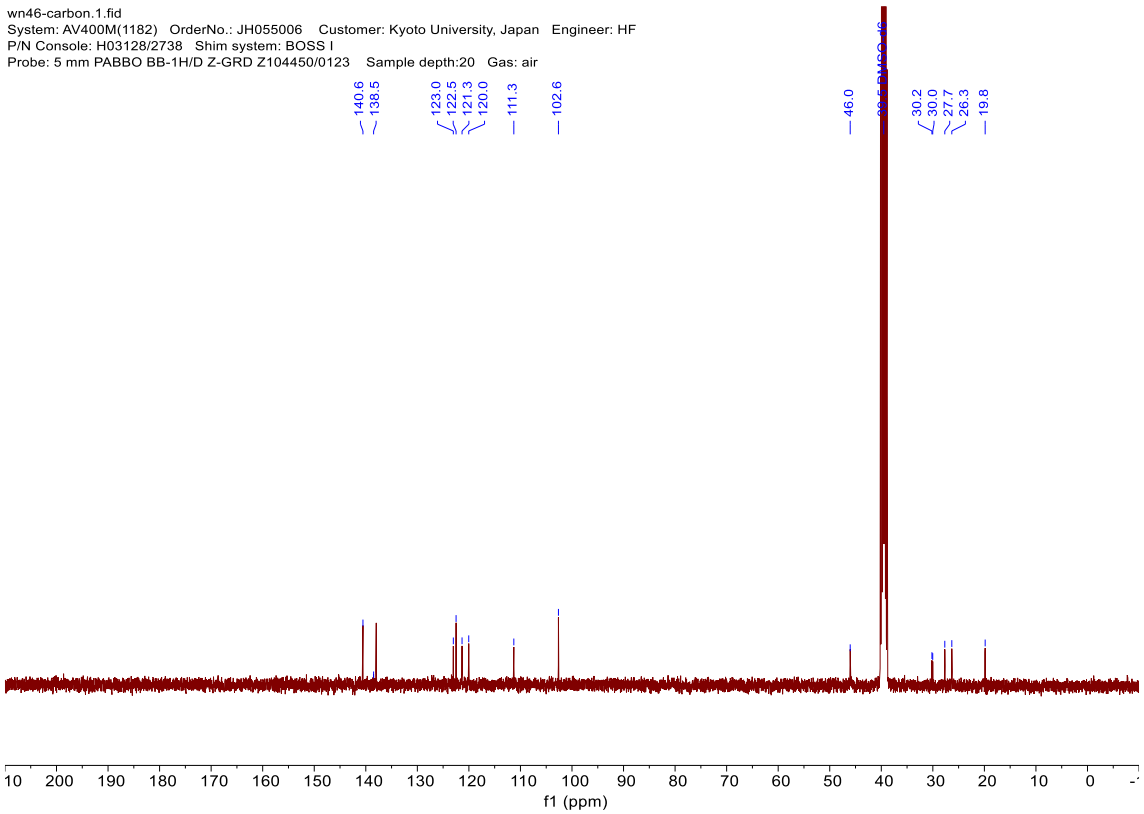

Figure S63. ^{13}C NMR spectrum of **3PATAT-C4** in DMSO-d_6.

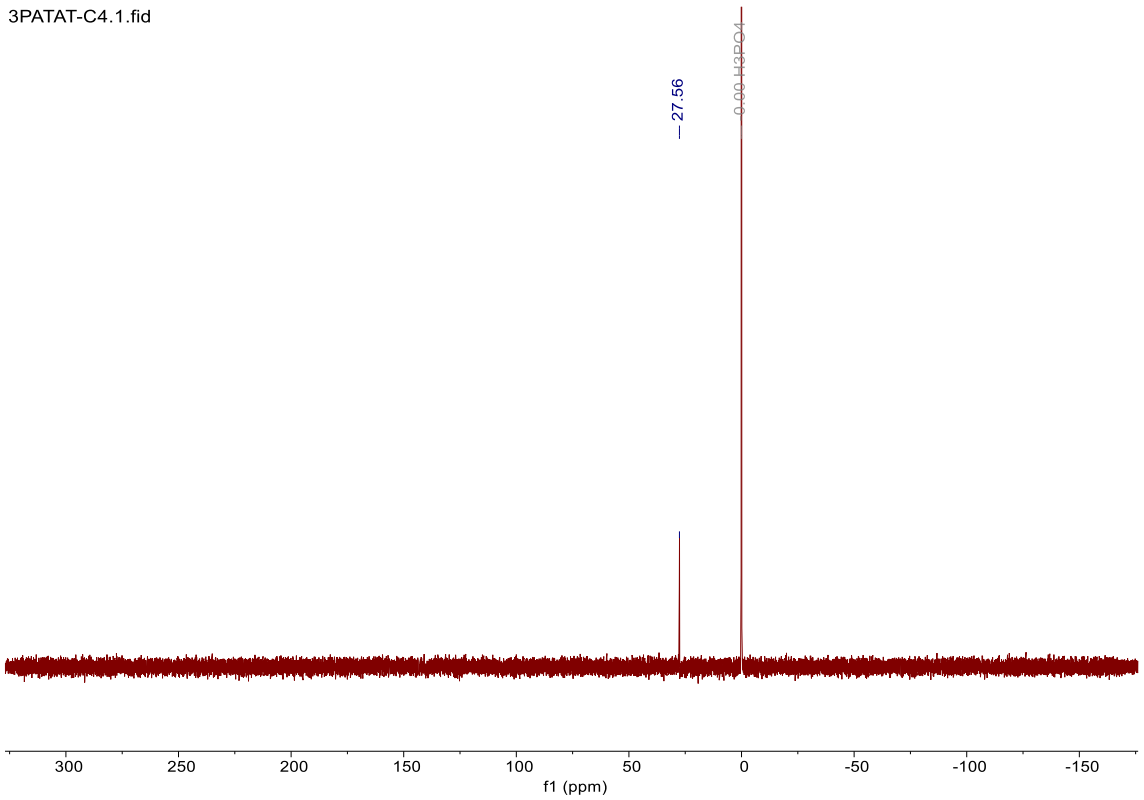

Figure S64. ^{31}P NMR spectrum of **3PATAT-C4** in DMSO-d_6.

References

(1) Gaussian 09, Revision C.01, Frisch, M. J.; Trucks, G. W.; Schlegel, H. B.; Scuseria, G. E.; Robb, M. A.; Cheeseman, J. R.; Scalmani, G.; Barone, V.; Petersson, G. A.; Nakatsuji, H.; Li, X.; Caricato, M.; Marenich, A. V.; Bloino, J.; Janesko, B. G.; Gomperts, R.; Mennucci, B.; Hratchian, H. P.; Ortiz, J. V.; Izmaylov, A. F.; Sonnenberg, J. L.; Williams-Young, D.; Ding, F.; Lipparini, F.; Egidi, F.; Goings, J.; Peng, B.; Petrone, A.; Henderson, T.; Ranasinghe, D.; Zakrzewski, V. G.; Gao, J.; Rega, N.; Zheng, G.; Liang, W.; Hada, M.; Ehara, M.; Toyota, K.; Fukuda, R.; Hasegawa, J.; Ishida, M.; Nakajima, T.; Honda, Y.; Kitao, O.; Nakai, H.; Vreven, T.; Throssell, K.; Montgomery, J. A., Jr.; Peralta, J. E.; Ogliaro, F.; Bearpark, M. J.; Heyd, J. J.; Brothers, E. N.; Kudin, K. N.; Staroverov, V. N.; Keith, T. A.; Kobayashi, R.; Normand, J.; Raghavachari, K.; Rendell, A. P.; Burant, J. C.; Iyengar, S. S.; Tomasi, J.; Cossi, M.; Millam, J. M.; Klene, M.; Adamo, C.; Cammi, R.; Ochterski, J. W.; Martin, R. L.; Morokuma, K.; Farkas, O.; Foresman, J. B.; Fox, D. J. Gaussian, Inc., Wallingford CT, 2016.

(2) Rakstys, K.; Abate, A.; Dar, M. I.; Gao, P.; Jankauskas, V.; Jacopin, G.; Kamarauskas, E.; Kazim, S.; Ahmad, S.; Grätzel, M.; Nazeeruddin, M. K. Triazatruxene-Based Hole Transporting Materials for Highly Efficient Perovskite Solar Cells. *J. Am. Chem. Soc.* **2015**, *137*, 16172–16178.

(3) Kresse, G.; Furthmüller, J. Efficient Iterative Schemes for ab initio Total-Eenergy Calculations using a Plane-Wave Basis Set. *Phys. Rev. B* **1996**, *54*, 11169–11186.

(4) Kresse, G.; Furthmüller, J. Efficiency of ab-initio Total Energy Calculations for Metals and Semiconductors using a Plane-Wave Basis Set. *Comput. Mater. Sci.* **1996**, *6*, 15–50.

(5) Blöchl, P. E. Projector Augmented-Wave Method. *Phys. Rev. B* **1994**, *50*, 17953–17979.

(6) Kresse, G.; Joubert, D. From Ultrasoft Pseudopotentials to the Projector Augmented-Wave Method. *Phys. Rev. B* **1999**, *59*, 1758–1775.

(7) Perdew, J. P.; Burke, K.; Ernzerhof, M. *Phys. Rev. Lett.* **1996**, *77*, 3865–3868.

(8) Donley, C.; Dunphy, D.; Paine, D.; Carter, C.; Nebesny, K.; Lee, P.; Alloway, D.; Armstrong, N. R. Characterization of Indium-Tin Oxide Interfaces Using X-ray Photoelectron Spectroscopy and Redox Processes of a Chemisorbed Probe Molecule: Effect of Surface Pretreatment Conditions. *Langmuir* **2002**, *18*, 450–457.

(9) Forget, A.; Limoges, B.; Balland, V. Efficient Chemisorption of Organophosphorous Redox Probe on Indium Tin Oxide Surfaces under Mild Conditions. *Langmuir* **2015**, *31*, 1931–1940.

(10) Paramonov, P. B.; Paniagua, S. A.; Hotchkiss, P. J.; Jones, S. C.; Armstrong, N. R.; Marder, S. R.; Brédas, J.-L. Theoretical Characterization of the Indium Tin Oxide Surface and of Its Binding Sites for Adsorption of Phosphonic Acid Monolayers. *Chem. Mater.* **2008**, *20*, 5131–5133.

(11) Al-Ashouri, A.; Magomedov, A.; Roß, M.; Jošt, M.; Talaikis, M.; Chistiakova, G.; Bertram, T.; Márquez, J. A.; Köhnen, E.; Kasparavičius, E.; Levcenco, S.; Gil-Escrig, L.; Hages, C. J.; Schlatmann, R.; Rech, B.; Malinauskas, T.; Unold, T.; Kaufmann, C. A.; Korte, L.; Niaura, G.; Getautis, V.; Albrecht, S. Conformal Monolayer Contacts with Lossless Interfaces for Perovskite Single Junction and Monolithic Tandem Solar Cells. *Energy Environ. Sci.* **2019**, *12*, 3356–3369.

Author Contributions

M.A.T. and A.W. conceived the idea and supervised the project. T.F., L.U., and W.N. contributed equally to this work. T.F., L.U., and W.N. carried out the synthesis and characterization of HCMs with the advice of T.S. M.A.T., T.F., and L.U. conducted the UV–Vis, CV and PYS measurements. M.A.T. and T.F. carried out the contact angle and IRRAS measurements with the help of N.S. and T.H. M.A.T., T.F., L.U., W.N., and S.Hi. fabricated, measured the devices, and conducted SEM characterizations. S.Hu conducted the XRD measurements. T.N. carried out $EDAI_2$ thermal deposition. M.A.T. carried out the PL measurements with the help of T.Y. and Y.K. R.M. conducted the impedance, light intensity dependence of open-circuit voltage, and MPPT measurements. N.S., Y.T., and S.I. carried out the theoretical calculations. M.A.T. prepared samples and A.A. carried out the UPS and MAES measurements and analysis under the supervision of H.Y. L.X. conducted the epitaxial ITO fabrication and AFM measurements with the help of D.K. and Y.S. M.A.T. , R.M., and A.W. prepared the manuscript. All authors commented on the manuscript.